

Structural and Physical Properties of Selected  
Complex Chalcogenides

Alexandra Kate Stephenson

Submitted for the degree of  
Master of Philosophy

Heriot-Watt University  
Institute of Chemical Sciences

June 2021

**The copyright in this thesis is owned by the author. Any quotation from the thesis or use of any of the information contained in it must acknowledge this thesis as the source of the quotation or information.**

## Abstract

The structure and physical properties of a selection of mixed-metal chalcogenides have been investigated. Materials covered in this study have shown a range of unusual behaviours.

$\text{GeV}_4\text{S}_8$  has been successfully synthesized in order to investigate the structural properties as a function of temperature. These data reveal that there are three distinct polymorphs over the temperature range  $7 \leq T / \text{K} \leq 32$ , of which one had not been previously determined. Neutron diffraction experiments reveal a series of peak splittings and broadenings upon cooling to indicate a deviation from the face-centred cubic structure at room temperature. A reduction in symmetry to  $R3m$ , at  $T_s = 32\text{K}$  is observed. Antiferromagnetic ordering is then associated with a second successive phase transition at  $T_N = 17\text{K}$  to  $Cm$ , which is a sub-group of  $R3m$ . This monoclinic phase has previously not been reported.

A new series has been prepared through substitution of chromium with indium in  $\text{Cr}_{1-x}\text{In}_x\text{GeTe}_3$  ( $0 \leq x \leq 1$ ) to investigate the effects of diluting the magnetic cation on the structural, physical and magnetic properties.  $\text{CrGeTe}_3$  crystallises in space group  $R\bar{3}$  with a three-layer repeating unit. It consists of hexagonally close packed layers of  $\text{Te}^{2-}$  ions, with  $\text{Cr}^{3+}$  ions and  $(\text{Ge}_2)^{6+}$  dumbbell pairs occupying octahedral holes in only every other layer. The unoccupied layers persist throughout the series; however cationic ordering within the layers of  $\text{Te}^{2-}$  ions results in different stacking sequences.

$\text{Cr}_{1-x}\text{In}_x\text{GeTe}_3$ ,  $x = 0, 0.1, 0.2, 0.5, 0.6$  samples have a range of ferromagnetism that can be described using Curie-Weiss law, but they also have regions of spin glass dominated behaviour below the ‘freeze’ temperature,  $T_f$ .

Semiconducting data showed samples did not exhibit thermally activated conduction but were found to fit a variable-range-hopping model that represents electrical conductivity in three-dimensions. At  $x = 0$ , Seebeck coefficients are large and positive, however for  $x = 1$ , markedly different behaviour is observed.  $\text{InGeTe}_3$  undergoes a change in the dominant charge carriers from electrons to holes at  $245\text{K}$ .

## Acknowledgements

It is with great gratitude to many people that this piece of work has been completed.

Thank you to Professor Anthony V. Powell, who supervised the work with patience and humour. He encourages the highest of standards and was relentless with his optimism of my ability.

Dr. Paz Vaqueiro was always on hand for problem solving and with her keen eye for detail, made some invaluable suggestions.

Thank you to all those involved at the ISIS facility, Didcot; their experience and advice was always required.

The laboratory technical support team at Heriot Watt University were consistently on call. Alan Barton (engineering workshop) and Paul Allan (glassblower) were accommodating and very reliable. Without Alan and Paul, the experimental work could not have been completed.

Thank you to the University for giving me all the opportunities to become a well-rounded enthusiastic employee. A highlight was to Captain the British Universities netball team.

Thank you to all my friends and family, who have listened, empathised and encouraged me through this process.



## Research Thesis Submission

Please note this form should be bound into the submitted thesis.

Name:	Alexandra Kate Stephenson		
School:	EPS		
Version: <small>(i.e. First, Resubmission, Final)</small>	Final	Degree Sought:	MPhil

### Declaration

In accordance with the appropriate regulations I hereby submit my thesis and I declare that:

1. The thesis embodies the results of my own work and has been composed by myself
2. Where appropriate, I have made acknowledgement of the work of others
3. The thesis is the correct version for submission and is the same version as any electronic versions submitted\*.
4. My thesis for the award referred to, deposited in the Heriot-Watt University Library, should be made available for loan or photocopying and be available via the Institutional Repository, subject to such conditions as the Librarian may require
5. I understand that as a student of the University I am required to abide by the Regulations of the University and to conform to its discipline.
6. I confirm that the thesis has been verified against plagiarism via an approved plagiarism detection application e.g. Turnitin.

### ONLY for submissions including published works


Please note you are only required to complete the Inclusion of Published Works Form (page 2) if your thesis contains published works)

7. Where the thesis contains published outputs under Regulation 6 (9.1.2) or Regulation 43 (9) these are accompanied by a critical review which accurately describes my contribution to the research and, for multi-author outputs, a signed declaration indicating the contribution of each author (complete)
8. Inclusion of published outputs under Regulation 6 (9.1.2) or Regulation 43 (9) shall not constitute plagiarism.

\* Please note that it is the responsibility of the candidate to ensure that the correct version of the thesis is submitted.

Signature of Candidate:		Date:	10 June 2021
-------------------------	---	-------	--------------

### Submission

Submitted By <small>(name in capitals)</small> :	Alexandra K Stephenson
Signature of Individual Submitting:	
Date Submitted:	10 June 2021

### For Completion in the Student Service Centre (SSC)

Limited Access	Requested	Yes	No	Approved	Yes	No
<i>E-thesis Submitted (mandatory for final theses)</i>						
Received in the SSC by <small>(name in capitals)</small> :				Date:		

**Internal Examiners Declaration Form**  
 (This form must be typed and all sections completed)

Candidate's Name:	ALEXANDRA STEPHENSON	Heriot-Watt Person ID:	071289184
School:	EPS	Degree Sought:	MPhil
Campus: <i>(If off-campus please state location)</i>	Edinburgh		

**Declaration**

1. I confirm that the corrections to the thesis of the above named have been carried out to the satisfaction of the examiners Yes  No  N/A

2. I confirm that the Joint Examiners Report Form states recommendation (c) - 'Award degree following satisfactory completion of significant corrections to the satisfaction of the Internal Examiner' Yes  No

**If yes,**

- Please provide details below to demonstrate that the particular corrections are satisfactory.
- Confirm that the corrections have been completed within the period of time given, if not please give an explanation.

Corrections have been checked by the Internal Examiner.

3. I confirm that the Joint Examiners Recommendation was originally: Re-submit (decision (d or e) on the previous Joint Examiners Form) Yes  No

4. I confirm that thesis title has changed since the temporary thesis was submitted. **If yes,** please provide details of amended title here: Yes  No

5. I confirm that I have seen the presentation (final bound) thesis and it has been bound in accordance with University regulations. Yes

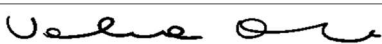
**Electronic Thesis**

As the Internal Examiner, I confirm that the student has prepared an electronic copy of the thesis in accordance with University guidelines **and it is an exact copy of the final bound thesis.**

Yes  No

*In accordance with [Heriot-Watt University Regulations](#), all students submitting research theses to the University for the awards of Doctor of Philosophy, Doctor of Philosophy by Published Research, Doctor of Engineering, Doctor of Business Administration, Master of Philosophy and/or Higher Degrees of Master (Research), must provide an electronic version of their final thesis. Further information on electronic thesis submission is available in the Submission and Format of Thesis Guidelines, available at <https://www.hw.ac.uk/students/studies/examinations/thesis.htm>*

**Internal Examiner**

Print Name:	Valeria Arrighi	Date:	9/06/2021
Signature:		School:	EPS

**Notes**

1. Please note that under current University Regulations one presentation (final bound) and one electronic copy of the thesis are required for final submission.
2. The Internal Examiner's Declaration Form should be submitted along with the presentation (final bound) and electronic copy of the thesis to the Student Service Centre.

# Contents

Abstract .....	ii
Acknowledgements .....	iii
Contents .....	vi
List of Figures .....	viii
Chapter 1: Introduction .....	1
1.1 Background .....	1
1.2 Structural Properties of Materials.....	1
1.2.1 Crystal Structures .....	1
1.2.2 Structure Types .....	2
1.2.3 Phase Transitions .....	3
1.3 Physical Properties of Materials.....	5
1.3.1 Electron-Transport Properties of Metals.....	6
1.3.2 Electron-Transport Properties of Insulators.....	8
1.3.3 Electron-Transport Properties of Semiconductors.....	8
1.3.4 Electron-Transport Properties of Superconductors.....	9
1.3.5 Magnetic Properties .....	9
1.4 Thermoelectric Properties .....	12
1.5 Chalcogenides .....	13
1.5.1 Sulphide Systems .....	14
1.5.2 Telluride Systems.....	20
1.6 Aim of this Work.....	21
1.7 References .....	22
Chapter 2: Preparation and Characterisation .....	25
2.1 Synthesis.....	25
2.2 Structural Characterisation .....	25
2.2.1 Powder X-ray Diffraction .....	25
2.2.2 Powder Neutron Diffraction.....	27
2.2.3 The Rietveld Method.....	35
2.2.4 Thermogravimetric Analysis (TGA).....	38
2.3 Physical Property Studies.....	39
2.3.1 Electron Transport Measurements .....	39
2.3.2 Seebeck Measurements .....	40
2.3.3 Thermal Conductivity Measurements .....	42

2.3.4	Magnetic Susceptibility Measurements .....	44
2.5	References .....	48
Chapter 3:	Structural Transitions in GeV <sub>4</sub> S <sub>8</sub> .....	50
3.1	Introduction .....	50
3.2	Background .....	50
3.3	Synthesis.....	51
3.4	Results .....	51
3.4.1	Characterisation.....	51
3.4.2	High temperature X-ray diffraction .....	53
3.4.3	Neutron studies of GeV <sub>4</sub> S <sub>8</sub> .....	54
3.4.4	Magnetic measurements of GeV <sub>4</sub> S <sub>8</sub> .....	94
3.5	Discussion .....	96
3.6	References .....	99
Chapter 4:	Structural, Physical and Magnetic Properties of Cr <sub>1-x</sub> In <sub>x</sub> GeTe <sub>3</sub>	
	101	
4.1	Introduction .....	101
4.2	Background .....	101
4.3	Synthesis.....	102
4.4	Results .....	105
4.4.1	Structural Studies on Cr <sub>1-x</sub> In <sub>x</sub> GeTe <sub>3</sub> at Room Temperature.	105
4.4.2	Low Temperature Neutron Diffraction .....	123
4.4.3	High Temperature X-ray Diffraction .....	125
4.4.4	Resistivity Measurements .....	128
4.4.5	Seebeck Coefficient .....	131
4.4.6	Thermal Conductivity .....	132
4.4.7	Thermoelectric Figure of Merit.....	133
4.4.8	Magnetic Studies.....	133
4.5	Discussion .....	139
4.6	References .....	140
Chapter 5:	Conclusions and Suggestions for Further Work .....	141
5.1	References .....	143

## List of Figures

Figure 1: Two close packed layers. Dots represent octahedral holes, crosses mark tetrahedral holes. ....	3
Figure 2: Schematic representation of a) NiAs; b) CdI <sub>2</sub> ; c) Cr <sub>2</sub> S <sub>3</sub> . ....	3
Figure 3: Schematic diagram exemplifying the electronic band structure of solids. ....	8
Figure 4: Plot of reciprocal susceptibility against temperature for paramagnetic materials that may show a tendency to order magnetically. (Slope equals C <sup>-1</sup> ) .....	11
Figure 5: Frustrated geometries: a) triangle, b) tetrahedron. ....	12
Figure 6: Schematic of normal spinel, AB <sub>2</sub> X <sub>4</sub> . Pink octahedra represent BX <sub>6</sub> units and white tetrahedra depict AX <sub>4</sub> . The cubic unit cell is represented by a black line. ....	15
Figure 7: AB <sub>4</sub> S <sub>8</sub> structure representations; a) cation-deficient spinel; b) (AS <sub>4</sub> ) <sup>n+</sup> tetrahedra and (B <sub>4</sub> S <sub>4</sub> ) <sup>n-</sup> units in rocksalt arrangement. ....	16
Figure 8: MO schemes of cluster orbitals in GaV <sub>4</sub> S <sub>8</sub> and GaMo <sub>4</sub> S <sub>8</sub> . ....	18
Figure 9: Schematic representation of FePS <sub>3</sub> . Pink polyhedra represent FeS <sub>6</sub> units; grey polyhedral represent P <sub>2</sub> S <sub>6</sub> units. ....	19
Figure 10: The three-layer structure of CrGeTe <sub>3</sub> . Pink polyhedra represent CrTe <sub>6</sub> units; grey polyhedral represent Ge <sub>2</sub> Te <sub>6</sub> units. ....	20
Figure 11: An X-ray spectrum showing the continuous ‘white radiation’ which peaks at about 4/3 λ <sub>swl</sub> and the sharp K <sub>α1</sub> and K <sub>α2</sub> peaks at wavelengths characteristic of the anode element, e.g. copper. ....	26
Figure 12: Schematic of the ISIS spallation neutron experiments, including TS2. ....	29
Figure 13: Schematic diagram of POLARIS instrument. ....	30
Figure 14: Sample alignment on POLARIS candlestick. ....	33
Figure 15: Schematic of HRPD. ....	34
Figure 16: Experimental setup for 4-probe electrical resistivity measurements. ....	40
Figure 17: The Seebeck effect. ....	41
Figure 18: Experimental setup for Seebeck coefficient measurements. ....	42
Figure 19: Final observed (crosses), calculated (upper full line) and difference (lower full line) X-ray diffraction profile at room temperature of GeV <sub>4</sub> S <sub>8</sub> . Reflection positions are marked. ....	52
Figure 20: Thermogravimetric analysis data for GeV <sub>4</sub> S <sub>8</sub> . ....	52
Figure 21: High temperature X-ray diffraction data for GeV <sub>4</sub> S <sub>8</sub> . ....	53
Figure 22: Final observed (crosses), calculated (upper full line) and difference (lower full line) neutron diffraction profile at 300K of GeV <sub>4</sub> S <sub>8</sub> . a) Backscattering bank, 2θ = 168.33° b) 90° bank, 2θ = 89.58°. Reflection positions are marked. ....	55
Figure 23: Temperature dependence of the unit cell in C-GeV <sub>4</sub> S <sub>8</sub> . Error bars are shown. ....	57
Figure 24: Splitting of the C-GeV <sub>4</sub> S <sub>8</sub> (622) reflection centred at d = 1.454 Å and the C-GeV <sub>4</sub> S <sub>8</sub> (533) reflection centred at d = 1.471 Å for 7 ≤ T / K ≤ 32. ....	58
Figure 25: Splitting of the C-GeV <sub>4</sub> S <sub>8</sub> (440) reflection centred at d = 1.705 Å for 7 ≤ T / K ≤ 32. ....	58
Figure 26: Specific heat capacity of GeV <sub>4</sub> S <sub>8</sub> . ....	59



Figure 27: Observed (crosses), calculated (upper full line) and difference (lower full line) neutron diffraction profile at 30K of GeV <sub>4</sub> S <sub>8</sub> . Backscattering bank, $2\theta = 168.33^\circ$ . Reflection positions are marked, black denotes <i>C</i> -GeV <sub>4</sub> S <sub>8</sub> , red <i>R</i> -GeV <sub>4</sub> S <sub>8</sub> .....	60
Figure 28: Observed (crosses), calculated (upper full line) and difference (lower full line) neutron diffraction profile at 25K of <i>O</i> -GeV <sub>4</sub> S <sub>8</sub> . Backscattering bank, $2\theta = 168.33^\circ$ . Reflection positions are marked.....	61
Figure 29: Matrix form of the cubic axis. ....	62
Figure 30: Final observed (crosses), calculated (upper full line) and difference (lower full line) neutron diffraction profile at 32K of GeV <sub>4</sub> S <sub>8</sub> . Backscattering bank, $2\theta = 168.33^\circ$ . Reflection positions are marked; blue denotes <i>C</i> -GeV <sub>4</sub> S <sub>8</sub> , red <i>R</i> -GeV <sub>4</sub> S <sub>8</sub> .....	63
Figure 31: Final observed (crosses), calculated (upper full line) and difference (lower full line) neutron diffraction profile at 31K of GeV <sub>4</sub> S <sub>8</sub> . Backscattering bank, $2\theta = 168.33^\circ$ . Reflection positions are marked; blue denotes <i>C</i> -GeV <sub>4</sub> S <sub>8</sub> , red <i>R</i> -GeV <sub>4</sub> S <sub>8</sub> and black <i>M</i> -GeV <sub>4</sub> S <sub>8</sub> . ....	64
Figure 32: Final observed (crosses), calculated (upper full line) and difference (lower full line) neutron diffraction profile at 30K of GeV <sub>4</sub> S <sub>8</sub> . Backscattering bank, $2\theta = 168.33^\circ$ . Reflection positions are marked; blue denotes <i>C</i> -GeV <sub>4</sub> S <sub>8</sub> , red <i>R</i> -GeV <sub>4</sub> S <sub>8</sub> and black <i>M</i> -GeV <sub>4</sub> S <sub>8</sub> . ....	65
Figure 33: Final observed (crosses), calculated (upper full line) and difference (lower full line) neutron diffraction profile at 29K of GeV <sub>4</sub> S <sub>8</sub> . Backscattering bank, $2\theta = 168.33^\circ$ . Reflection positions are marked; blue denotes <i>C</i> -GeV <sub>4</sub> S <sub>8</sub> , red <i>R</i> -GeV <sub>4</sub> S <sub>8</sub> and black <i>M</i> -GeV <sub>4</sub> S <sub>8</sub> . ....	66
Figure 34: Final observed (crosses), calculated (upper full line) and difference (lower full line) neutron diffraction profile at 25K of GeV <sub>4</sub> S <sub>8</sub> . Backscattering bank, $2\theta = 168.33^\circ$ . Reflection positions are marked; blue denotes <i>C</i> -GeV <sub>4</sub> S <sub>8</sub> , red <i>R</i> -GeV <sub>4</sub> S <sub>8</sub> and black <i>M</i> -GeV <sub>4</sub> S <sub>8</sub> . ....	67
Figure 35: Final observed (crosses), calculated (upper full line) and difference (lower full line) neutron diffraction profile at 20K of GeV <sub>4</sub> S <sub>8</sub> . Backscattering bank, $2\theta = 168.33^\circ$ . Reflection positions are marked; blue denotes <i>C</i> -GeV <sub>4</sub> S <sub>8</sub> , red <i>R</i> -GeV <sub>4</sub> S <sub>8</sub> and black <i>M</i> -GeV <sub>4</sub> S <sub>8</sub> . ....	68
Figure 36: Final observed (crosses), calculated (upper full line) and difference (lower full line) neutron diffraction profile at 19K of GeV <sub>4</sub> S <sub>8</sub> . Backscattering bank, $2\theta = 168.33^\circ$ . Reflection positions are marked; blue denotes <i>C</i> -GeV <sub>4</sub> S <sub>8</sub> , red <i>R</i> -GeV <sub>4</sub> S <sub>8</sub> and black <i>M</i> -GeV <sub>4</sub> S <sub>8</sub> . ....	69
Figure 37: Final observed (crosses), calculated (upper full line) and difference (lower full line) neutron diffraction profile at 18K of GeV <sub>4</sub> S <sub>8</sub> . Backscattering bank, $2\theta = 168.33^\circ$ . Reflection positions are marked; blue denotes <i>C</i> -GeV <sub>4</sub> S <sub>8</sub> , red <i>R</i> -GeV <sub>4</sub> S <sub>8</sub> and black <i>M</i> -GeV <sub>4</sub> S <sub>8</sub> . ....	70
Figure 38: Final observed (crosses), calculated (upper full line) and difference (lower full line) neutron diffraction profile at 15K of <i>M</i> -GeV <sub>4</sub> S <sub>8</sub> . Backscattering bank, $2\theta = 168.33^\circ$ . Reflection positions are marked.....	71
Figure 39: Final observed (crosses), calculated (upper full line) and difference (lower full line) neutron diffraction profile at 7K of <i>M</i> -GeV <sub>4</sub> S <sub>8</sub> . Backscattering bank, $2\theta = 168.33^\circ$ . Reflection positions are marked.....	72
Figure 40: <i>C</i> -GeV <sub>4</sub> S <sub>8</sub> in <i>F</i> 43 <i>m</i> at 29K. Sulphur atoms are shown as yellow spheres, vanadium atoms as grey spheres, with a solid line representing a V-S bond. GeV <sub>4</sub> <sup>4+</sup> units are represented by pink tetrahedra. ....	86
Figure 41: <i>R</i> -GeV <sub>4</sub> S <sub>8</sub> in <i>R</i> 3 <i>m</i> at 29K. Sulphur atoms are shown as yellow spheres, vanadium atoms as grey spheres, with a solid line representing a V-S bond. GeV <sub>4</sub> <sup>4+</sup> units are represented by pink tetrahedra.....	86

Figure 42: $M\text{-GeV}_4\text{S}_8$ in $Cm$ at 29K. Sulphur atoms are shown as yellow spheres, vanadium atoms as grey spheres, with a solid line representing a V-S bond. $\text{GeV}_4^{4+}$ units are represented by pink tetrahedra .....	87
Figure 43: Graph showing temperature dependence of each polymorph of $\text{GeV}_4\text{S}_8$ . Above 32K $\text{GeV}_4\text{S}_8$ is cubic ( $F43m$ ). Below 16K $\text{GeV}_4\text{S}_8$ is monoclinic ( $Cm$ ). Error bars are shown. ....	88
Figure 44: Temperature dependence of unit cell parameters for $R\text{-GeV}_4\text{S}_8$ ; a) $a$ lattice constant; b) $\alpha$ angle. Error bars are shown. ....	89
Figure 45: Temperature dependence of the unit cell parameters for $M\text{-GeV}_4\text{S}_8$ ; a) $a$ , $b$ , $c$ lattice constants; b) $\beta$ angle. Error bars are shown. ...	90
Figure 46: Graph showing discontinuities at 18K in the $b$ and $c$ lattice parameters of $M\text{-GeV}_4\text{S}_8$ . Error bars are shown. ....	91
Figure 47: Comparison of the temperature dependence of the unit cell parameters for $C\text{-GeV}_4\text{S}_8$ (grey squares), $R\text{-GeV}_4\text{S}_8$ (pink triangles) and $M\text{-GeV}_4\text{S}_8$ (black circles). Error bars are shown. ....	91
Figure 48: $R\text{-GeV}_4\text{S}_8$ : $\text{V}_4\text{S}_4^{4+}$ cubane unit.....	92
Figure 49: $M\text{-GeV}_4\text{S}_8$ : $\text{V}_4\text{S}_4^{4+}$ cubane unit.....	93
Figure 50: a) zero-field cooled and field cooled molar magnetic susceptibilities measured in a field of 1000G. b) observed (points) and calculated (red line) reciprocal susceptibility data. The calculated line is derived from the fit to Curie-Weiss law.....	95
Figure 51: X-ray diffraction data ( $1.694 \leq d / \text{\AA} \leq 1.714$ ) collected by Johrendt <i>et al.</i> for $10 \leq T / \text{K} \leq 33$ . Reflection positions are marked for $O\text{-GeV}_4\text{S}_8$ (solid lines) and $R\text{-GeV}_4\text{S}_8$ (dashed lines).....	97
Figure 52: Cluster MO scheme for a) $C\text{-GeV}_4\text{S}_8$ and b) $R\text{-GeV}_4\text{S}_8$ .....	98
Figure 53: The three-layer structure of $\text{CrGeTe}_3$ . Pink polyhedra represent $\text{CrTe}_6$ units; grey polyhedral represent $\text{Ge}_2\text{Te}_6$ units. ....	101
Figure 54: Room temperature X-ray diffraction data for $\text{CrGeTe}_3$ (black line), $\text{Cr}_{0.5}\text{In}_{0.5}\text{GeTe}_3$ (blue line) and $\text{InGeTe}_3$ (pink line).....	106
Figure 55: Lattice parameters as a function of indium substitution in $\text{Cr}_{1-x}\text{In}_x\text{GeTe}_3$ ( $0 \leq x \leq 1$ ) determined by TOPAS analysis in space group $R3$ . Error bars are shown. ....	106
Figure 56: POLARIS neutron diffraction data showing the differences in superlattice peaks and $[00l]$ reflections between $\text{CrGeTe}_3$ (black), $\text{InGeTe}_3$ (pink) and $\text{Cr}_{0.5}\text{In}_{0.5}\text{GeTe}_3$ (blue) in the $4.75 \leq d / \text{\AA} \leq 7.5$ region.....	107
Figure 57: The two-layer structure of $\text{Cr}_{0.5}\text{In}_{0.5}\text{GeTe}_3$ . ....	108
Figure 58: Primitive lattice parameters as a function of indium substitution as determined by Rietveld refinement.....	109
Figure 59: Final observed (crosses), calculated (upper full line) and difference (lower full line) X-ray and neutron diffraction profiles for $\text{CrGeTe}_3$ at room temperature. a) X-ray; b) Neutron, backscattering bank, $2\theta = 145^\circ$ ; c) Neutron, low angle bank, $2\theta = 35^\circ$ . Reflection positions are marked.....	110
Figure 60: Final observed (crosses), calculated (upper full line) and difference (lower full line) X-ray and neutron diffraction profiles for $\text{Cr}_{0.9}\text{In}_{0.1}\text{GeTe}_3$ at room temperature. a) X-ray; b) Neutron, backscattering bank, $2\theta = 145^\circ$ ; c) Neutron, low angle bank, $2\theta = 35^\circ$ . Reflection positions are marked; black, $\text{CrGeTe}_3$ ; blue, $\text{Cr}_{0.9}\text{In}_{0.1}\text{GeTe}_3$ ; red, Te. ....	111
Figure 61: Final observed (crosses), calculated (upper full line) and difference (lower full line) X-ray and neutron diffraction profiles for $\text{Cr}_{0.8}\text{In}_{0.2}\text{GeTe}_3$ at room temperature. a) X-ray; b) Neutron, backscattering	

bank, $2\theta = 145^\circ$ ; c) Neutron, low angle bank, $2\theta = 35^\circ$ . Reflection positions are marked.....	112
Figure 62: Final observed (crosses), calculated (upper full line) and difference (lower full line) X-ray and neutron diffraction profiles for $\text{Cr}_{0.5}\text{In}_{0.5}\text{GeTe}_3$ at room temperature. a) X-ray; b) Neutron, backscattering bank, $2\theta = 145^\circ$ ; c) Neutron, low angle bank, $2\theta = 35^\circ$ . Reflection positions are marked.....	113
Figure 63: Final observed (crosses), calculated (upper full line) and difference (lower full line) neutron diffraction profiles, for $\text{Cr}_{0.4}\text{In}_{0.6}\text{GeTe}_3$ at room temperature. a) Neutron, backscattering bank, $2\theta = 145^\circ$ ; b) Neutron, low angle bank, $2\theta = 35^\circ$ . Reflection positions are marked.....	114
Figure 64: Final observed (crosses), calculated (upper full line) and difference (lower full line) X-ray and neutron diffraction profiles, using le Bail refinement, for $\text{InGeTe}_3$ at room temperature. a) X-ray; b) Neutron, backscattering bank, $2\theta = 145^\circ$ ; c) Neutron, low angle bank, $2\theta = 35^\circ$ . Reflection positions are marked.....	115
Figure 65: Final observed (crosses), calculated (upper full line) and difference (lower full line) neutron diffraction profile for $\text{CrGeTe}_3$ at 4.2K; backscattering bank $2\theta = 145^\circ$ . Reflection positions are marked; lower markers refer to crystallographic unit cell, upper markers to the superimposed magnetic unit cell.....	123
Figure 66: High temperature X-ray diffraction data for $\text{CrGeTe}_3$ . .....	126
Figure 67: High temperature X-ray diffraction data for $\text{Cr}_{0.5}\text{In}_{0.5}\text{GeTe}_3$ . ..	127
Figure 68: Electrical resistivity data for end-members of the $\text{Cr}_{1-x}\text{In}_x\text{GeTe}_3$ series.....	128
Figure 69: Electrical resistivity data for the series $\text{Cr}_{1-x}\text{In}_x\text{GeTe}_3$ .....	129
Figure 70: Temperature dependence of $\text{Cr}_{0.5}\text{In}_{0.5}\text{GeTe}_3$ using a variable-range-hopping relation; $\ln(\rho/T^{1/2})$ versus $T^{-\nu}$ where $\nu = 1/4$ .....	130
Figure 71: Electrical resistivity of $\text{Cr}_{0.4}\text{In}_{0.6}\text{GeTe}_3$ over the range $115 \leq T / \text{K} \leq 350$ .....	131
Figure 72: Selected Seebeck coefficient data for the series $\text{Cr}_{1-x}\text{In}_x\text{GeTe}_3$ collected between $100 \leq T / \text{K} \leq \text{RT}$ . .....	132
Figure 73: Thermal conductivity data for $\text{Cr}_{1-x}\text{In}_x\text{GeTe}_3$ at 300 K. ....	132
Figure 74: Magnetic susceptibility data for $\text{CrGeTe}_3$ measured in a field of 100 G. Red circles represent field cooled and black squares show zero-field cooled data. The inset shows the fit of a Curie-Weiss expression to the reciprocal susceptibility. ....	134
Figure 75: Plot showing the temperature dependence of the effective magnetic moment per ion in $\text{CrGeTe}_3$ . ....	135
Figure 76: Magnetic susceptibility data for $\text{Cr}_{0.9}\text{In}_{0.1}\text{GeTe}_3$ measured in a field of 100 G. Red circles represent field cooled and black squares show zero-field cooled data. The inset shows the fit of a Curie-Weiss expression to the reciprocal susceptibility. ....	135
Figure 77: Magnetic susceptibility data for $\text{Cr}_{0.8}\text{In}_{0.2}\text{GeTe}_3$ measured in a field of 100 G. Red circles represent field cooled and black squares show zero-field cooled data. The inset shows the fit of a Curie-Weiss expression to the reciprocal susceptibility. ....	136
Figure 78: Plot showing the temperature dependence of the effective magnetic moment per ion in $\text{Cr}_{0.8}\text{In}_{0.2}\text{GeTe}_3$ . ....	136
Figure 79: Magnetic susceptibility data for $\text{Cr}_{0.5}\text{In}_{0.5}\text{GeTe}_3$ measured in a field of 100 G. Red circles represent field cooled and black squares show	

zero-field cooled data. The inset shows the fit of a Curie-Weiss expression to the reciprocal susceptibility. ....	137
Figure 80: Plot showing the temperature dependence of the effective magnetic moment per ion in $\text{Cr}_{0.5}\text{In}_{0.5}\text{GeTe}_3$ . ....	137
Figure 81: Plot showing the saturation magnetisation of $2.91(1) \mu_B$ for $\text{Cr}_{0.5}\text{In}_{0.5}\text{GeTe}_3$ .....	138
Figure 82: Magnetic susceptibility data for $\text{Cr}_{0.2}\text{In}_{0.8}\text{GeTe}_3$ measured in a field of 100 G. Red circles represent field cooled and black squares show zero-field cooled data. The inset demonstrates the poor fit of a Curie-Weiss expression to the reciprocal susceptibility. ....	138

# Chapter 1: Introduction

## 1.1 Background

Solid state chemistry explores the structure and physical properties of matter in the solid state. The specialised applications, whether in medicine, informatics or refrigeration, which utilise solid state materials, require thorough understanding down to the molecular and atomic levels [1-3]. In order to facilitate technological progress, advances in the materials and knowledge utilised in such applications must be made.

This chapter provides an overview of the important concepts associated with the structural and physical properties of solid state materials and an introduction to the systems investigated.

## 1.2 Structural Properties of Materials [4]

Determining and understanding the structural properties of materials is of great importance. It provides the essential information required in order to further improve and develop materials utilised in a broad range of applications.

### 1.2.1 Crystal Structures

With the exception of helium, all substances form a solid state, some of which are crystalline. A crystalline phase is a result of a regular repeating array of atoms or molecules packing together in three dimensions. The smallest repeating unit of such an array is known as a unit cell. There are only seven independent unit cell shapes that are possible in three dimensions, known as the crystal systems, Table 1. The atoms comprising the unit cell are depicted as points in a lattice; these points are then linked together. Depending on how these points are linked determines the type of lattice that results. A primitive lattice (*P*) has points at the corners whereas a centred lattice includes additional points. These centred lattices have different terminology depending on the position of the additional points; a face centred lattice (*F*) has additional points in the centre of each face; a side centred lattice has

additional points on one pair of opposite faces, for example a C-centred lattice has points on the  $ab$  face of the unit cell; a body-centred lattice ( $I$ ) has a point at the centre of the cell. The crystal system and the lattice type combine to produce fourteen Bravais lattices that describe a structure.

**Table 1:** The seven crystal systems.

Crystal System	Unit cell shape	Essential symmetry	Allowed lattices
<b>Cubic</b>	$a = b = c, \alpha = \beta = \gamma = 90^\circ$	4 3-fold axes	$P, F, I$
<b>Tetragonal</b>	$a = b \neq c, \alpha = \beta = \gamma = 90^\circ$	1 4-fold axis	$P, I$
<b>Orthorhombic</b>	$a \neq b \neq c, \alpha = \beta = \gamma = 90^\circ$	3 2-fold axes or mirror planes	$P, F, I, A (B \text{ or } C)$
<b>Hexagonal</b>	$a = b \neq c, \alpha = \beta = 90^\circ, \gamma = 120^\circ$	1 6-fold axis	$P$
<b>Trigonal (a)</b>	$a = b \neq c, \alpha = \beta = 90^\circ, \gamma = 120^\circ$	1 3-fold axis	$P$
<b>(b)</b>	$a = b = c, \alpha = \beta = \gamma \neq 90^\circ$	1 3-fold axis	$R$
<b>Monoclinic</b>	$a \neq b \neq c, \alpha = \gamma = 90^\circ, \beta \neq 90^\circ$	1 2-fold axis or mirror plane	$P, C$
<b>Triclinic</b>	$a \neq b \neq c, \alpha \neq \beta \neq \gamma \neq 90^\circ$	none	$P$

### 1.2.2 Structure Types

When atoms are arranged to have the maximum density possible, they are known as close packed. Close packing of equally sized spheres leads to six nearest neighbours in a two dimensional plane. These layers can then be stacked in three dimensions in two ways: hexagonal close packing ( $hcp$ ) and cubic close packing ( $ccp$ ). A  $hcp$  arrangement results from an ...ABABAB... sequence of close packed layers, i.e. the layers sit on top of the same type of site as they are built up into three dimensions. A  $ccp$  arrangement, however, comprises an ...ABCABC... repeat. Here, the layers sit on a geometrically different site compared with the layer below. For example, the B layer may occupy the tetrahedral holes then the C layer, the octahedral.

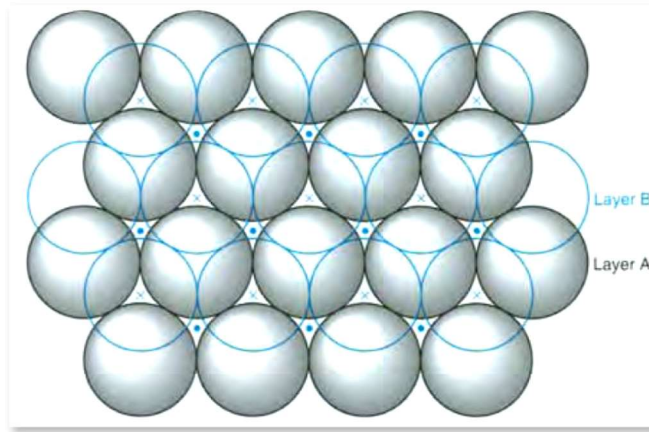


**Figure 1:** Two close packed layers. Dots represent octahedral holes, crosses mark tetrahedral holes.[5]

The NiAs structure is a *hcp* array of arsenic atoms with 100% occupation of the octahedral holes by nickel atoms [6]. Simply, the structure is built up of layers of edge-sharing NiAs<sub>6</sub> octahedra. Using this repeating unit as the sub-cell, partial occupation of the octahedral sites can result in a variety of super-cells. If the octahedral sites are unoccupied every other slab (50% of the octahedral sites occupied), the CdI<sub>2</sub> structure type results [7]. In the Cr<sub>2</sub>S<sub>3</sub> type, a third of the octahedral sites are occupied between layers [8]. These super-cells result from the stacking of the layers directly on top of each other. Alternative sub-cells result from the displacement of one or more of the layers. For example, in CdCl<sub>2</sub> the middle layer in a sequence of three is displaced resulting in a doubling of the unit cell [9].

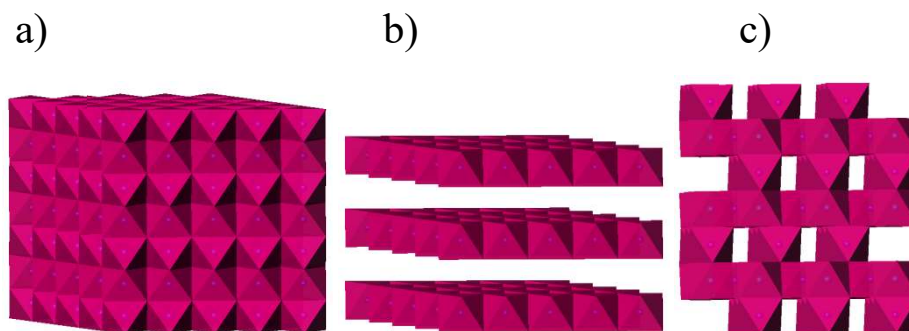


**Figure 2:** Schematic representation of a) NiAs; b) CdI<sub>2</sub>; c) Cr<sub>2</sub>S<sub>3</sub>.

### 1.2.3 Phase Transitions

The transformation between two polymorphic forms of a crystalline material is known as a phase transition. The terminology of transition or

transformation is normally found to be interchangeable, though 'transition' is usually reserved for changes in structure only. A phase transition is the response of a material or system to a change in conditions, for example, temperature or pressure. These transitions are affected by thermodynamic and kinetic factors. Thermodynamics determines the behaviour that should be observed under equilibrium conditions of a particular material or system. This information can be displayed in the form of a phase diagram. The rates of transformation, the kinetics, are governed by the type of mechanism. Nucleation and growth mechanisms result in slow transitions as a result of the slow and difficult rate determining step of nucleation. Martensitic [10-12] and displacive [13] phase transitions occur spontaneously as nucleation is easy.

Phase transitions can be classified according to their structural or thermodynamic properties. When using a description associated with structural properties, transitions can be separated into two groups: reconstructive and displacive.

Reconstructive phase transitions constitute a major reorganisation of crystal structure where bonds are broken and reformed. No structural relationship is required between the two polymorphs, thus no space group or symmetry relation is necessary. These commonly have high activation energies and take place over a long period of time. This type of transition can be prevented.

Displacive transitions result from bond distortions, where no bonds are broken. Changes are often subtle but take place more readily in this type of transformation. They cannot be prevented. Polymorphs must have a symmetry relation. The low temperature polymorph must belong to a subgroup of the high temperature phase.

When based on thermodynamic behaviour phase transitions are known as first or second (or higher) order. At equilibrium temperatures or pressures of a phase transition, Gibbs free energy of the two polymorphs is the same and no discontinuity occurs.

$$\Delta G = \Delta H - T\Delta S = 0$$

**Equation (1)**



A first order transition results when a discontinuity occurs in the first derivatives of free energy with respect to temperature and pressure. The derivatives correspond to entropy and volume respectively. First order transitions are usually easy to detect. A discontinuity in volume will reveal a change in crystal structure and enthalpy. These changes can be observed in X-ray diffraction and DTA experiments respectively. Visual observations may also result from a change in volume, for example in  $ZrO_2$ .

A second order transition will exhibit a discontinuity in the second derivatives of free energy, i.e. heat capacity, thermal expansion and compressibility. Transitions of the second order are not as easy to observe as the changes are much smaller. They can be detected by measuring the heat capacities. Heat capacities usually increase on approach to  $T_c$  and show a discontinuity at  $T_c$ . Between absolute zero and  $T_c$  there are also huge increases in entropy, though there is no discontinuity. This exemplifies a second order phase transition.

With these descriptions it would appear that classifying a phase transition is relatively straight forward, though this is often not the case. Hybrid character is observed when there is a large increase in enthalpy on approach to  $T_c$ , though there is strictly no discontinuity in enthalpy at  $T_c$ . In this instance, continuous and discontinuous transition is found to be more appropriate terminology. A continuous transition is one in which there is no discontinuity in enthalpy at  $T_c$ , where the crystal structure changes are gradual. The converse is seen in a discontinuous transition.

Phase transitions mostly show premonitory behaviour, that is an increase in entropy and heat capacity as  $T_c$  is approached. It is this behaviour that links the first and the second order transition. If premonitory changes terminate with a discontinuity, an infinite change in the heat capacity, the transition is first order or discontinuous. If no discontinuity is observed and the heat capacity demonstrates a finite change at  $T_c$  the transition is second order or continuous.

### **1.3 Physical Properties of Materials [4, 5]**

It is often more practicable to classify materials with respect to their electrical and magnetic properties. These characteristics depend directly on the

behaviour of electrons. There are four principle groups in terms of the electrical properties of materials;

- metals;
- insulators;
- semiconductors;
- superconductors.

Primarily, the main difference between these groups is the electronic conductivity ( $\sigma$ ) defined in Equation (2).

$$\sigma = ne\mu$$

**Equation (2)**

where  $n$  is the number,  $e$  is the charge and  $\mu$  is the mobility of the charge carriers. The conductivity temperature dependence of the above groups can be rationalised by considering the temperature dependence of these quantities.

All materials exhibit some sort of magnetism. There are five categories in which a material can be classified;

- diamagnetism;
- paramagnetism;
- ferromagnetism (*FM*);
- antiferromagnetism (*AFM*);
- ferrimagnetism.

### **1.3.1 Electron-Transport Properties of Metals**

The conductivity of metals is the highest, typically  $10^4$ - $10^6 \Omega^{-1} \text{ cm}^{-1}$ , and decreases as the temperature of the system is reduced. The number of charge carriers is large and remains unchanged with temperature. The mobility of the charge carriers is the only variable. This decreases with temperature as the phonons gain energy and have larger amplitudes.

The high conductivity of metals can be explained in terms of band theory. An extension of molecular orbital (MO) theory from a simple diatomic to a larger molecule (a metal can be considered as an infinitely large molecule) is necessary. In larger molecules there are a greater number of MO's as a result

of the increased numbers of atomic orbitals. As the numbers of MO's increase, the energy gap between them decreases, eventually resulting in a continuum of energy levels that are delocalised over all the atoms in the system. These energy levels form the basis of energy bands. By calculating the band structure it can be seen that the width of a band is related to the interatomic separation,  $r$ , and therefore to the amount of orbital overlap between the atoms. The degree of overlap determines how metallic a compound is. The application of pressure to a system causes some discrete levels to overlap as  $r$  is reduced.

The free electron theory of Sommerfeld can also be used to describe band theory in terms of the energy and wavelength of electrons in a solid. [14] With analogy to a particle in a box, a metal is regarded as a potential well in which loosely bound electrons are able to move around. Within the well, energy levels are quantised and filled from the bottom obeying the Pauli exclusion principle. The Fermi level is the highest level filled at absolute zero with energy,  $E_F$ . The energy required to remove the electrons from the Fermi level is known as the work function energy,  $\phi$ . When the number of energy levels,  $N(E)$ , are plotted as a function of energy,  $E$ , a density of states diagram results. As per Sommerfeld it shows that as the energy increases the number of available energy levels also increases. At temperatures above absolute zero there are a few electrons that have sufficient thermal energy to be promoted to energy levels above  $E_F$ , thus leaving some levels unoccupied below  $E_F$ . The drift in electrons between partially occupied levels surrounding  $E_F$  results in larger numbers of mobile electrons and is therefore the reason for high conductivity within metals.

This oversimplified picture is developed by regarding the potential in the well as periodic and not constant. By having a regular arrangement of positively charged nuclei the potential energy of the electron can be calculated by solving the Schrödinger equation for a periodic potential function. Due to coulombic attraction, the electron passes through a minimum at the site of the nuclei and a maximum, equidistance between two adjacent nuclei. The solution shows that there are only certain allowed levels in which the electrons can be permitted. These forbidden energies are found to satisfy Bragg's law, Equation (8), and result in discontinuities in the density of states.

The band structure of metals is characterised by a part-full valence band where electrons in singly occupied levels can move freely. The overlapping of energy bands can result in partially filled bands. The band structure of beryllium consists of overlapping  $2s$  and  $2p$  bands that are only partly occupied. If these bands did not overlap, the two would be completely occupied and beryllium would not be metallic.

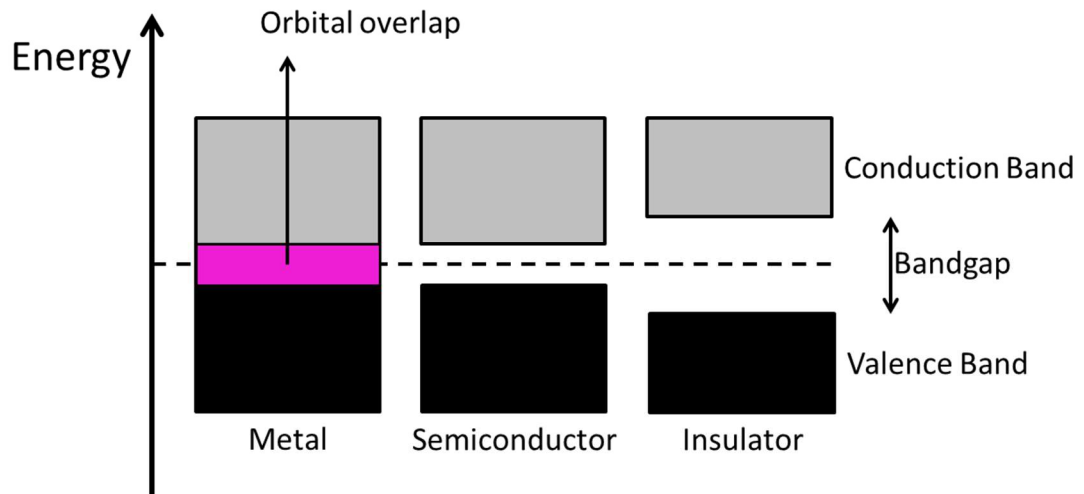


**Figure 3:** Schematic diagram exemplifying the electronic band structure of solids.

### 1.3.2 Electron-Transport Properties of Insulators

An insulator is characterised by a band structure comprising a full valence band. The valence band is separated from the highest unoccupied level (conduction band) by a forbidden gap, a band gap. A large band gap ensures very few electrons have sufficient energy to make the transition from the valence band to the conduction band. Diamond has a large band gap at  $\sim 6$  eV.

### 1.3.3 Electron-Transport Properties of Semiconductors

The band structure of semiconductors is similar to that of an insulator, however, the band gap is smaller, typically 0.5 to 3.0 eV. In these circumstances, a few electrons have sufficient thermal energy to be promoted to the empty band. There are two types of conduction mechanism. The first considers a promoted electron as a negative charge carrier. Under an applied potential it would move towards a positive electrode. This sort is known as an  $n$ -type semiconductor. The second utilises positive hole conduction. This

arises when vacant energy levels (holes) are left behind in the valence band. The holes are repetitively filled leaving another hole in a different location. Holes, therefore, move in the opposite direction to electrons. Materials exhibiting this type of behaviour are known as *p*-type semiconductors.

Semiconductors can be classified further into two groups: *intrinsic* and *extrinsic*. Intrinsic semiconductors are those whose properties are inherent to the electron configuration. Extrinsic semiconductors arise from the deliberate introduction of very low concentrations of specific impurities into very pure materials. As boron has one fewer valence electron compared with silicon, the substitution of silicon with boron in a silicon crystal will create holes in the valence band of the density of states (*p*-type semiconductor).

#### **1.3.4 Electron-Transport Properties of Superconductors [15]**

Superconductivity was discovered in 1911 by Heike Onnes and arises when a material exhibits infinite conductivity below a certain temperature,  $T_c$ . Above  $T_c$ , materials show a finite conductivity, consistent with other metallic samples. The resistance offered above  $T_c$  results from interactions between the lattice vibrations and the dynamic conduction electrons. Below  $T_c$ , however, electrons proceed through the lattice in a concerted fashion with the lattice vibrations, resulting in zero resistance, infinite conductivity.

#### **1.3.5 Magnetic Properties**

Diamagnetism reduces the magnetic flux density of a field and is present in all substances. These interactions are produced by circulation of closed shell electrons in an atom or molecule and are very weak. Unpaired electrons, however, give rise to paramagnetism. Paramagnetism is found in materials where the unpaired electrons are isolated on different atoms. The thermal energy of the system ensures these spinning electrons orientate in a random way. When placed in a magnetic field, the moments on each centre tend to align with respect to each other and the field. The correlation between the applied field and the thermal randomization can be described using the Curie law,

$$\chi = \frac{C}{T}$$

**Equation (3)**

where  $\chi$  is the magnetic susceptibility,  $C$  is the Curie constant and  $T$  is the temperature. Curie law states the magnetic susceptibility is inversely proportional to temperature. It is only applicable when there is no interaction between adjacent moments. Though the moments do tend to align when exposed to a magnetic field, it becomes increasingly difficult as the temperature is increased.

Cooperative magnetism is where there are spontaneous interactions between adjacent spins. At low temperatures this may develop into ferro-, antiferro- or ferrimagnetism. Curie-Weiss law, Equation (4), is found to be a better description of the high-temperature paramagnetic region.

$$\chi = \frac{C}{T - \theta}$$

**Equation (4)**

where  $\theta$  is the Weiss constant.

A plot of the reciprocal susceptibility against temperature indicates the type of behaviour observed in a material. Substances that show no tendency to align, simple paramagnets, extrapolate through the origin. Ferromagnets show some local alignment of spins in the paramagnetic region, above the ordering temperature. This results in higher susceptibility values and positive Weiss constants, when compared to the purely paramagnetic material. The temperature below which the sample is ferromagnetic is called the ferromagnetic Curie temperature,  $T_c$ .  $T_c$  usually coincides with the reciprocal susceptibility approaching zero.

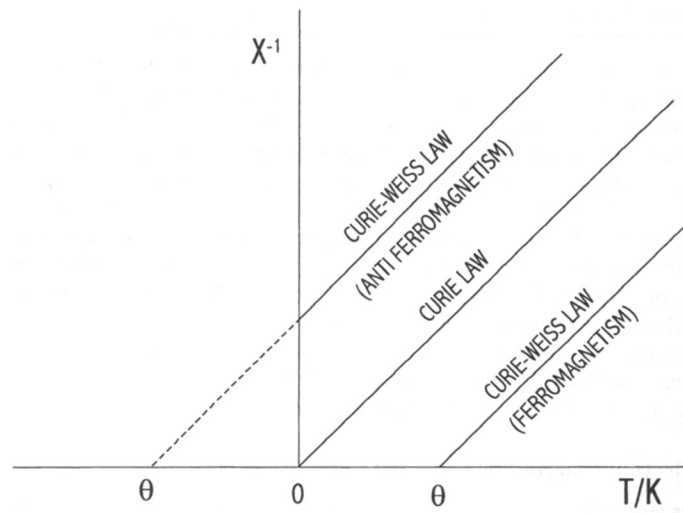


**Figure 4:** Plot of reciprocal susceptibility against temperature for paramagnetic materials that may show a tendency to order magnetically.

(Slope equals  $C^{-1}$ ) [5].

Antiferromagnetic ordering results in reduced susceptibility values compared with purely paramagnetic materials and extrapolated Weiss constants that are negative. As these temperatures cannot be achieved a departure from Curie-Weiss law is observed on cooling below the Néel temperature,  $T_N$ . The susceptibility is very small at low temperatures for an antiferromagnetic substance, as the temperature is increased the thermally-induced disorder causes an increase in the susceptibility. This increase hits its maximum at  $T_N$  and then declines as the temperature is further increased, now paramagnetic following Curie-Weiss law.

Some antiferromagnetic materials show spin glass-like behaviour that results from a frustrated arrangement of spins. Magnetic frustration is when a large fraction of magnetic sites in a lattice are subject to competing or contradictory constraints [16]. Here, the interactions between adjacent unpaired electrons results in antiferromagnetism but this cannot develop into long range order due to the presence of unavoidable ferromagnetic pairings. When frustration arises from the topology of the lattice it is termed geometric frustration, for example, an equilateral triangle or tetrahedron. If the energy is to be minimised the spin alignments must be collinear, clearly in a triangle only two of the three spin constraints can be satisfied at the same time. Hence, the

system is geometrically frustrated. In the case of the tetrahedron only two of the four constraints can be simultaneously satisfied.

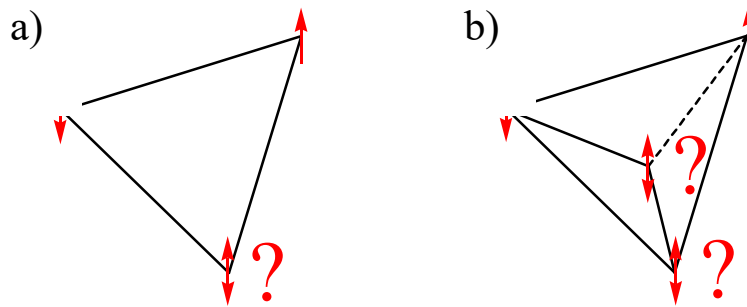


**Figure 5:** Frustrated geometries: a) triangle, b) tetrahedron.

There are three commonly encountered types of lattice that can exhibit frustrated magnetism; the corner shared triangular lattice or Kagome lattice; the edge shared tetrahedral lattice or face centred cubic (FCC) lattice and the corner shared tetrahedral lattice. The FCC lattice comprises the  $16c$  or  $16d$  sites in the  $Fd\bar{3}m$  space group that describes the spinel [17] and pyrochlore [18] structure type. A frustrated system can still make the transition to a long range ordered state by adopting a non-collinear or compromise spin configuration to introduce degeneracy into the ground state. However, many materials do not exhibit any long range order. This arises when each unit minimises the energy of the ground state but there is no correlation between adjacent frustrated units.

## 1.4 Thermoelectric Properties [4, 19]

Currently there is great interest in developing novel thermoelectric materials for thermoelectric energy conversion [20, 21]. The coupling between heat and electrical currents has captivated scientists since the early experiments of Lenz in 1838 [22]. It is also recognised that this technology has a wide range of applications for power generation in terms of waste heat recovery and cooling of a large variety of modern electronic devices. [3]

In a typical thermoelectric device, a junction is formed with a  $p$ -type and an  $n$ -type semiconductor. If an electric current is then passed through the junction, the charge carriers move away from the junction, creating a cooling effect. Conversely, a heat source at the junction causes carriers to flow away



from the junction generating an electric current. The relative performance of a thermoelectric material is given by the dimensionless figure of merit  $ZT$ ,

$$ZT = \frac{(S^2\sigma)T}{\kappa_e + \kappa_{ph}}$$

**Equation (5)**

where  $S$  is the Seebeck coefficient;  $\sigma$  is the electrical conductivity;  $\kappa_e$  is the electrical carrier contribution to the thermal conductivity;  $\kappa_{ph}$  is the lattice vibration contribution to the thermal conductivity and  $T$  the absolute temperature. These devices are advantageous due to the lack of moving parts, but more efficient constituent materials are required for widespread refrigeration and electrical power generation. Commercially available materials with  $ZT \sim 1$  cannot compete with traditional vapour compression systems [23].

The best thermoelectric materials were succinctly defined as “phonon-glass electron-crystal”, which means that the materials should have a low lattice thermal conductivity as in a glass, and a high electrical conductivity as in a crystal [24]. There is an interdependence between  $S$ ,  $\sigma$  and  $\kappa_e$ , however  $\kappa_{ph}$  can be independently tuned. In order to maximise the figure of merit, the power factor,  $S^2\sigma$ , can be increased by optimising the carrier concentration or the lattice thermal conductivity can be reduced [25]. Investigations by the Research Triangle Institute showed that to be economically competitive for refrigerators  $ZT \approx 3$ . For example;  $p$ -type superlattices of  $\text{Bi}_2\text{Te}_3/\text{Sb}_2\text{Te}_3$  have  $ZT = 2.4$  at room temperature whereas  $n$ -type  $ZT = 1.2$  [19].

## 1.5 Chalcogenides

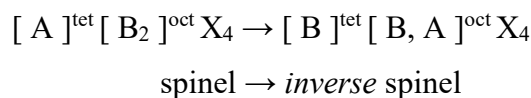
Chalcogenides are composite materials that contain a group 16 element (chalcogen). Chalcogenides are found to exhibit a variety of different structure types including; corundum [26]; perovskite [27]; and spinel [17]. Chalcogenides with the formula  $A_y\text{MX}_2$  ( $0 \leq y \leq 1$ ) adopt a structure consisting of layers of  $\text{MX}_2$  edge-sharing octahedra separated by a network of octahedral sites. In a fashion analogous to section 1.2.2, the value of  $y$  determines the occupancy of these holes and therefore the supercell of the

material. Interesting magnetic and electrical properties can also be observed in this broad category of materials. A wide range of applications result from the assortment of properties and traces can be made back to ancient Egypt where the cubic semiconductor PbS was used as kohl eye liner. In the early 20<sup>th</sup> century PbS was then utilised in crystal radio sets; the perovskite, CaTiO<sub>3</sub>, aids the integration of bone implants; Bi<sub>2</sub>Te<sub>3</sub> is an established low temperature thermoelectric material; and ZnSe is used to form light emitting diodes [28].

### 1.5.1 Sulphide Systems

Sulphides are an important class of materials that exhibit a wide range of properties. For example, in Cr<sub>2</sub>S<sub>3</sub> ( $y = 1/3$ ), the vacancy ordering between the layers results in supercell parameters  $\sqrt{3}a_p \times \sqrt{3}a_p \times \sqrt{3}c_p$  with respect to the primitive hexagonal subcell. Cr<sub>2</sub>S<sub>3</sub> is a ferrimagnetic material,  $T_C \approx 125$  K, which displays an anomaly at  $T_C$  in the transport properties. This anomaly is thought to originate from the spin-disorder scattering of the charge carriers from the exchange splitting of the conduction band. Sulphides find uses in tincture; solar cells; and catalysis. They are found readily as metal ores including: argentite; cinnabar; and chalcopyrite.

The spinel structure (Figure 6) is often adopted by materials with the general formula AB<sub>2</sub>O<sub>4</sub> [17]. In nature the mineral spinel is MgAl<sub>2</sub>O<sub>4</sub> but analogous structures exist for many oxides, sulphides and halides (AB<sub>2</sub>X<sub>4</sub>). The cationic components can comprise different charge combinations to result in an overall neutral material, for example Cu<sub>2</sub>SnS<sub>4</sub> and Li<sub>2</sub>NiF<sub>4</sub>. MgAl<sub>2</sub>O<sub>4</sub> crystallizes in spacegroup  $Fd\bar{3}m$  and comprises a *ccp* array of O<sup>2-</sup> ions. Al<sup>3+</sup> ions occupy one half of the octahedral sites whilst maintaining a three-dimensional network of corner-sharing tetrahedra; Mg<sup>2+</sup> ions are distributed evenly over one eighth of the T<sub>+</sub> and T<sub>-</sub> tetrahedral sites. An *inverse* spinel is the result of half of the cations that normally reside on an octahedral site, occupying the tetrahedral holes as demonstrated below [29, 30]:



These compounds are generally only single-phase at stoichiometric compositions. Cation deficiency is much less common in spinel-type phases than in nickel arsenide-type, where a range of cation-ordered phases can be observed. However, a group of materials exist that are non-stoichiometric [31, 32].

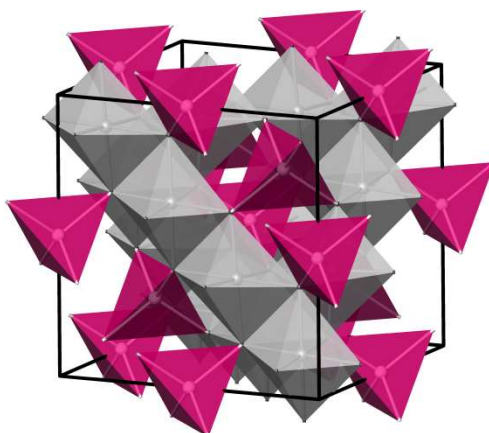


**Figure 6:** Schematic of normal spinel,  $AB_2X_4$ . Pink octahedra represent  $BX_6$  units and white tetrahedra depict  $AX_4$ . The cubic unit cell is represented by a black line.

A small family of non-stoichiometric, spinel-related materials exist that are 50% deficient at the A-cation site when compared with the spinel structure. These sulphur containing phases result in an  $AB_4S_8$  general formula ( $A_{0.5}B_2X_4 \equiv AB_2X_4$ ), where  $A = Ga, Al, Ge, Fe-Ni, Zn$  and  $B = Mo, V, Nb, Ta, (Mo/Re)$  [31]. Cation substitution at the A-site has been explored through the series;  $Ga_{1-x}Ge_xV_4S_8$ ;  $Ga_{1-x}Cu_xV_4S_8$ ;  $Ga_{1-x}Zn_xV_4S_8$ ; a limited deficiency or excess can also be tolerated at the A-site. B-site substitution has also been investigated though;  $GaV_{4-x}Mo_xS_8$ ;  $Ga_xV_{4-y}Cr_yS_8$ .

The  $AB_4S_8$  structure can be described on the basis of a cation-deficient spinel [33, 34] but is more appropriately depicted when considering the metal-metal bonding arising from the B-site cations (Figure 7). Accounting for these interactions, the  $AB_4S_8$  phase comprises  $(AS_4)^{n+}$  tetrahedra and cubanelike

$(B_4S_4)^{n-}$  units ordered in a rocksalt arrangement [35]. The reduced symmetry ( $Fd\bar{3}m \rightarrow F\bar{4}3m$ ) of the defect spinel is a result of the ordering of the vacancies associated with the tetrahedral A-sites and the displacement of the octahedral B-site from 0.625 in the spinel to  $\approx 0.6$  [36]. The octahedral coordination of the B-site is strongly distorted by the splitting of the six equidistant nearest neighbours.

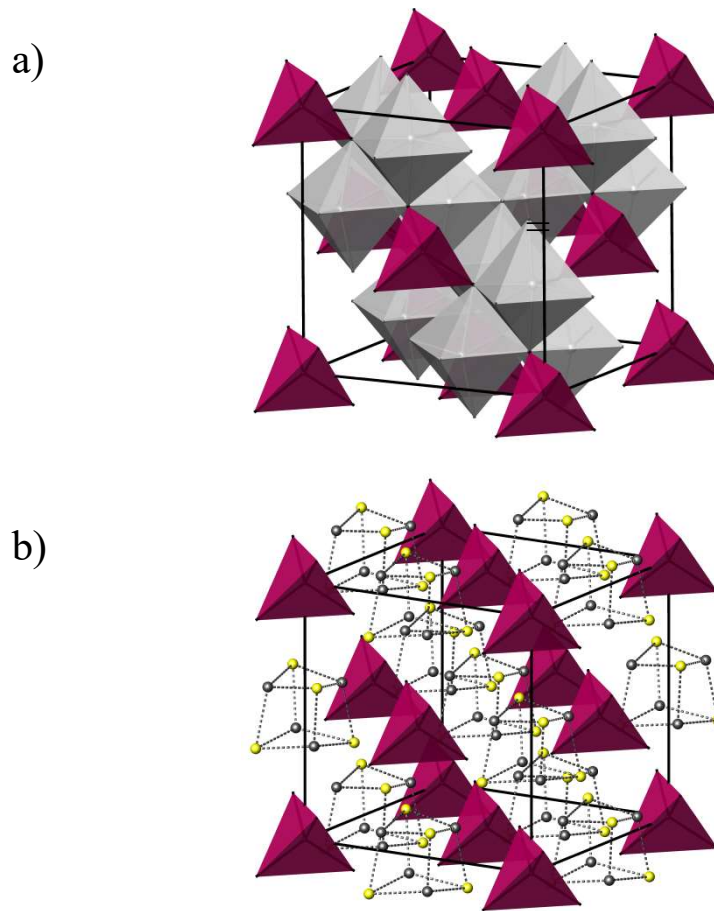


**Figure 7:**  $AB_4S_8$  structure representations; a) cation-deficient spinel;  
b)  $(AS_4)^{n+}$  tetrahedra and  $(B_4S_4)^{n-}$  units in rocksalt arrangement.

**Table 2:** Low temperature structural deformations in selected defect thiospinels.

Compound	Space group	Lattice parameters, $a / \text{\AA}, c / \text{\AA}, \alpha / ^\circ$	Transition temperature, $T_s / \text{K}$	Magnetic ordering
<b>GaMo<sub>4</sub>S<sub>8</sub></b>	<i>R3m</i>	$a = 6.8506(2)$ $\alpha = 60.533(1)$	45	<i>FM</i> , $T_C = 19\text{K}$
<b>GaV<sub>4</sub>S<sub>8</sub></b>	<i>R3m</i>	$a = 6.83974(4)$ $\alpha = 59.616(1)$	40	<i>FM</i> , $T_C \approx 9\text{K}$
<b>AlMo<sub>4</sub>S<sub>8</sub></b>	<i>R3m</i>	$a = 6.8500(3)$ $\alpha = 60.374(5)$	24	<i>FM</i> , $T_C \approx 24\text{K}$
<b>GaNb<sub>4</sub>S<sub>8</sub></b>	<i>P<math>\bar{4}</math><sub>2</sub><i>m</i></i>	$a = 9.992(1)$ $c = 9.978(2)$	31	<i>AFM</i> , $T_N = 31\text{K}$

Defect thiospinels are known to exhibit structural distortions at low temperatures. The most common modification is to a rhombohedral unit cell (Table 2). Powder X-ray diffraction studies reveal that the cubic unit cell of GaMo<sub>4</sub>S<sub>8</sub> undergoes a compression along the body diagonal to result in a rhombohedral lattice where  $\alpha > 60^\circ$ . Conversely, the distortion in GaV<sub>4</sub>S<sub>8</sub> is a result of an expansion along the analogous diagonal to form a lattice where  $\alpha < 60^\circ$ . The opposing nature of the transformation was rationalised by considering the metal-based atomic orbitals in the (B<sub>4</sub>S<sub>4</sub>)<sup>n-</sup> units. Band structure calculations on cubic GeV<sub>4</sub>S<sub>8</sub> reveal very narrow bands near the Fermi level indicating electron-electron interactions are important. The DOS in the same energy range is dominated by metal-metal bonding states of the V<sub>4</sub> cluster generated by the V 3d orbitals. The cluster orbitals have symmetries  $a_1$ ,  $e$  and  $t_2$  at  $\Gamma$ , with the  $t_2$  being the highest occupied, three-fold degenerated level. The number of valence electrons within the  $t_2$  level determines the direction of the distortion within these phases. GaV<sub>4</sub>S<sub>8</sub> has one electron that occupies the  $t_2$  level whereas GaMo<sub>4</sub>S<sub>8</sub> has five. The degeneracy is removed upon the reduction of symmetry to result in a pair of degenerated levels with  $e$  symmetry and a single level with  $a_1$  symmetry. When the angle deviates from  $\alpha = 60^\circ$  (ideal cubic), there is an opposite effect depending on whether  $\alpha$  increases or decreases about  $60^\circ$ . For  $\alpha < 60^\circ$ , the  $a_1$  level is stabilised with respect to the  $t_2$  levels and the  $e$  levels increase in energy. The converse occurs when  $\alpha > 60^\circ$ . If the  $a_1$  level is reduced by an energy  $-2\varepsilon$ , then the  $e$  levels must be increased in energy by  $+1\varepsilon$ . When the MO's are filled with the available valence electrons of the thiospinel

moiety,  $\Delta E$  can be used to predict the direction of the distortion (Figure 8). It is, therefore, energetically favourable for smaller angles in  $\text{GaV}_4\text{S}_8$  and larger angles in  $\text{GaMo}_4\text{S}_8$ .

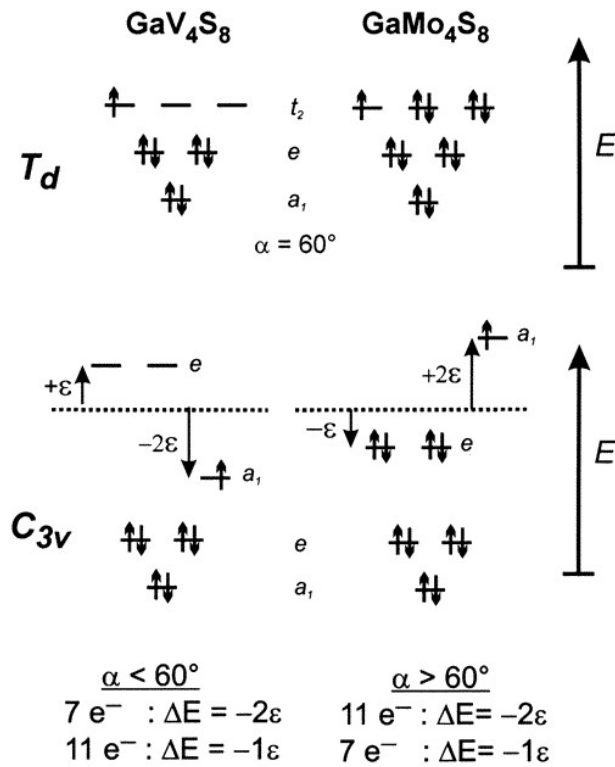


**Figure 8:** MO schemes of cluster orbitals in  $\text{GaV}_4\text{S}_8$  and  $\text{GaMo}_4\text{S}_8$ . [36]

$\text{MPS}_3$  ( $M = \text{V} \rightarrow \text{Zn}$ ) phases constitute an interesting group of layered compounds found to be semiconducting. They were first obtained by Friedel who reported the structure of  $\text{FePS}_3$  (Figure 9), but more extensively investigated by Klingen in the late seventies. In an analogous way to the defect thiospinel family of compounds there are two ways in which to describe the structure; the first is to use the formula  $\text{M}_{2/3}(\text{P}_2)_{1/3}\text{S}_2$  and consider the structure as layers of edge-sharing,  $\text{MS}_6$  octahedra with  $1/3$  of the cationic sites occupied in an ordered manner by a phosphorous atom pair ( $\text{P}_2$  dumbbell), separated by a van der Waals' gap; in the second scenario the phase can be depicted as a salt-like arrangement of  $\text{M}^{2+}$  cations and  $(\text{P}_2\text{S}_6)^{4-}$  anions. The layers are stacked in an ...ABCABC... arrangement analogous to the  $\text{CdCl}_2$ -type structure. However, contrary to the  $\text{CdCl}_2$  structure the trigonal symmetry is not retained and the unit cell is largely found to be monoclinic, space group  $C2/m$ .  $\text{FePS}_3$  and  $\text{CoPS}_3$  both exhibit ideal  $\beta$  values,  $\beta = 107.16^\circ$ , and can therefore be indexed on the basis of a hexagonal unit

cell, though retaining the atomic arrangement of the monoclinic cell. In the vanadium analogue some of the interslab cationic sites are occupied and therefore remove the van der Waals' gap.

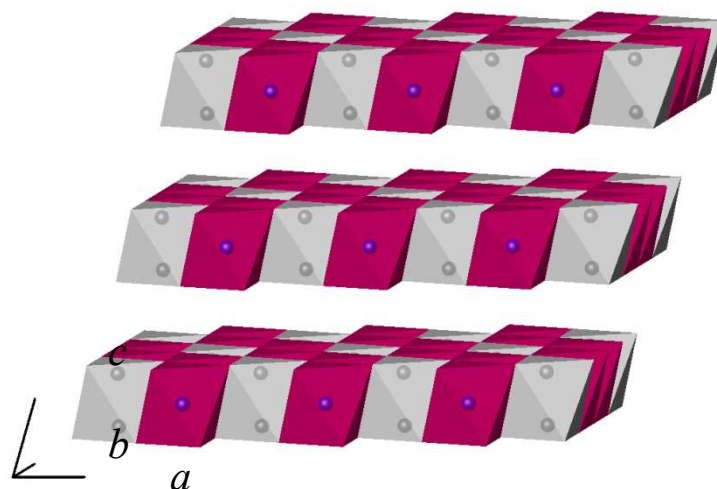


**Figure 9:** Schematic representation of FePS<sub>3</sub>. Pink polyhedra represent FeS<sub>6</sub> units; grey polyhedral represent P<sub>2</sub>S<sub>6</sub> units.

The MPS<sub>3</sub>-type structure, where M = Mn, Fe, Co and Ni, exemplifies low-dimensional magnetic systems, Curie-Weiss law is obtained only at high temperatures. At low temperatures antiferromagnetic ordering is observed. In FePS<sub>3</sub>, Fe<sup>2+</sup> ions compete in competitive ferromagnetic, antiferromagnetic couplings, i.e. each Fe<sup>2+</sup> ion is ferromagnetically coupled, within a layer, with two nearest neighbours and antiferromagnetically coupled to the third.[37] A Mössbauer study of FePS<sub>3</sub> revealed the existence of paramagnetic and antiferromagnetic domains near the ordering temperature. This is thought to occur as a result of the magnetic hyperfine field making a sudden drop to zero at different temperatures for the respective phases. Some MPS<sub>3</sub> phases are found to readily intercalate electron donors. The nature of the accepting levels is often sought after. The DOS for FeSP<sub>3</sub> shows that there are two, sharp, partially filled conduction bands situated 12eV below the empty 4s and 4p molecular orbitals. The valence band, largely sulphur 3p in character, is able to donate electrons into these partially occupied bands. However in ZnPS<sub>3</sub> and CdPS<sub>3</sub> the band structure is slightly different due to the presence of a d<sup>10</sup> ion resulting in the acceptor levels being too high in energy. This is seen practically as these two compounds are unable to intercalate electron donors.

### 1.5.2 Telluride Systems

Materials containing tellurium, although highly toxic, have been widely investigated due to their diverse structural and physical properties. Tellurides are of huge commercial importance in terms of thermoelectric materials. As the demand for renewable energy devices has increased so too has the research into mixed metal tellurides. Tellurides are found to crystallise in a wide range of structure types, often similar to those observed in sulphide systems.

$\text{CrGeTe}_3$  [38, 39] is a ternary low-dimensional transition metal chalcogenide first published in 1995 by Carteaux *et al.*.  $\text{CrGeTe}_3$ , and its tellurosilicate analogue, can be described in a hexagonal unit cell, space group  $R\bar{3}$ , with lattice parameters;  $a = 6.7578 \text{ \AA}$ ;  $c = 20.665 \text{ \AA}$ . The structure shows obvious similarities to the  $\text{MPS}_3$ -type structure and consists of a hexagonal close packed arrangement of tellurium atoms where the octahedral sites are fully occupied in an ordered manner every other layer analogous to  $\text{CdCl}_2$ . Throughout the occupied layer,  $2/3$  of the octahedra are centred with chromium ions, the remaining  $1/3$  with a  $\text{Ge}_2$  pair.

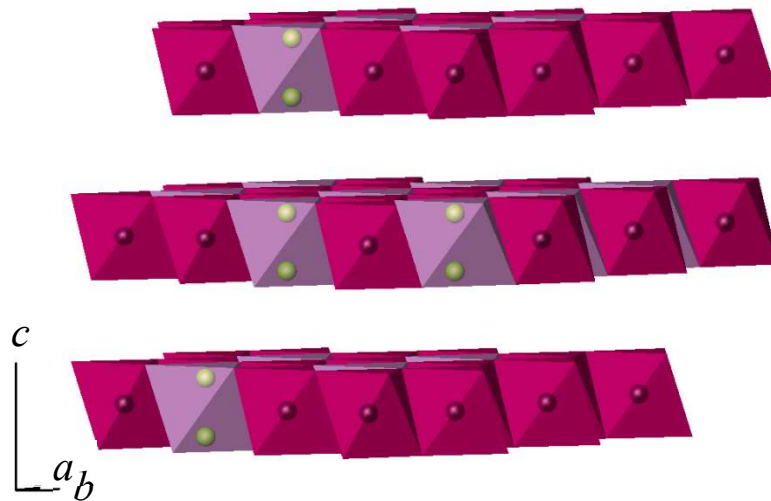


**Figure 10:** The three-layer structure of  $\text{CrGeTe}_3$ . Pink polyhedra represent  $\text{CrTe}_6$  units; grey polyhedral represent  $\text{Ge}_2\text{Te}_6$  units.

$\text{CrGeTe}_3$  is ferromagnetic below 61 K, with the spins are aligned along the  $c$ -axis. The calculated effective magnetic moment,  $\mu_{\text{eff}} = 3.77 \mu_{\text{B}}$ , is in agreement with the theoretical value but the thermal evolution of the



magnetisation curve shows unusual behaviour; significant magnetisation is observed above the three-dimensional ordering temperature that can be attributed to two-dimensional, short range ordering. A neutron diffraction study revealed that the magnetic peaks disappear completely above  $T_C$  with no residual magnetisation. The magnetic contributions are superimposed on the Bragg peaks due to the nuclear cell and correspond to the collinear configuration of the spins lying along the  $c$ -axis.

Room temperature resistivity measurements have been carried out on single crystal platelets revealing  $\rho = 0.02 \text{ } \Omega \text{ cm}$ . When applying the Montgomery method to determine the thermal evolution of the resistivity,  $\text{CrGeTe}_3$  is found to be semiconducting and can be fitted as  $\rho = e^{A/kT}$ , where  $k$  is the Boltzmann constant and  $A = 0.2 \text{ eV}$  at temperatures greater than  $T_C$ . The Fermi level,  $E_F = 11.85 \text{ eV}$ , corresponds to a very sharp increase in the DOS largely due to the chromium 3d orbitals ( $t_{2g}$ ). The intensity and shape indicate a localised electronic system consistent with a Mott insulator.

## 1.6 Aim of this Work

This body of work has been carried out in order to expand the knowledge of chalcogenide systems with a view to providing a better foundation for the development of technologically useful materials and focussed primarily on:

- Determining the absolute low temperature structure of  $\text{GeV}_4\text{S}_8$  and rationalising the physical behaviour associated with it.
- Investigating the effect on the physical properties of  $\text{CrGeTe}_3$  by substituting the magnetic cation for a non-magnetic cation.

## 1.7 References

- [1] S. Raoux, M. Wuttig, *Phase change materials: science and applications*. Springer Science & Business Media, 2010.
- [2] S.W. McKeever, M. Moscovitch, P.D. Townsend, (1995).
- [3] T.M. Tritt, M. Subramanian, *MRS bulletin* 31 (2006) 188-198.
- [4] A.R. West, *Solid State Chemistry and its Applications*. John Wiley & Sons, LTD, 1984.
- [5] A.R. West, *Basic Solid State Chemistry*. John Wiley & Sons, LTD, 1999.
- [6] J. Thompson, A. Rae, R. Withers, T. Welberry, A. Willis, *Journal of Physics C: Solid State Physics* 21 (1988) 4007.
- [7] R.M. Bozorth, *Journal of the American Chemical Society* 44 (1922) 2232-2236.
- [8] F. Jellinek, *Acta Crystallographica* 10 (1957) 620-628.
- [9] L. Pauling, J.L. Hoard, *Zeitschrift fuer Kristallographie* 74 (1930) 546-551.
- [10] K.C. Le, C. Günther, *Journal of the Mechanics and Physics of Solids* 79 (2015) 67-79.
- [11] S. Miyazaki, A. Ishida, *Materials Science and Engineering a-Structural Materials Properties Microstructure and Processing* 273 (1999) 106-133.
- [12] C. Salazar Mejia, A.M. Gomes, *Journal of Alloys and Compounds* 586 (2014) 718-721.
- [13] G.A. Samara, T. Sakudo, K. Yoshimitsu, *Physical Review Letters* 35 (1975) 1767-1769.
- [14] A. Sommerfeld, *Zeits. and Physik*, 1928, pp. 1-32 43-60.
- [15] J. Bardeen, L.N. Cooper, J.R. Schrieffer, *Physical Review* 108 (1957) 1175.
- [16] J. Greedan, *Journal of Materials Chemistry* 11 (2001) 37-53.
- [17] H. Sawada, *Materials Research Bulletin* 30 (1995) 341-345.
- [18] J.M. Longo, P.M. Raccah, J.A. Kafalas, J.W. Pierce, *Materials Research Bulletin* 7 (1972) 137-146.
- [19] F.J. Disalvo, *Science* 285 (1999) 703-706.

- [20] M.A. McGuire, T.K. Reynolds, F.J. DiSalvo, *Chemistry of Materials* 17 (2005) 2875-2884.
- [21] M.A. McGuire, T.K. Reynolds, F.J. DiSalvo, *Journal of Alloys and Compounds* 425 (2006) 81-87.
- [22] B.C. Sales, D. Mandrus, R.K. Williams, *Science* 272 (1996) 1325-1328.
- [23] H. Alam, S. Ramakrishna, *Nano Energy* 2 (2013) 190-212.
- [24] G.A. Slack, in: H. Ehrenreich, F. Seitz, D. Turnbull, (Eds.), *Solid State Physics*, 1979, pp. 1-71.
- [25] D.K. Misra, S. Sumithra, N.S. Chauhan, W.M. Nolting, P.F.P. Poudeu, K.L. Stokes, *Materials Science in Semiconductor Processing* 40 (2015) 453-462.
- [26] L. Pauling, S.B. Hendricks, *Journal of The American Chemical Society* 47 (1925) 781-790.
- [27] F.S. Galasso, *Structure, Properties and Preparation of Perovskite-Type Compounds: International Series of Monographs in Solid State Physics*. Elsevier, 2013.
- [28] H. Zou, D. Rowe, G. Min, *Journal of Crystal Growth* 222 (2001) 82-87.
- [29] J. Popović, B. Gržeta, B. Rakvin, E. Tkalčec, M. Vrankić, S. Kurajica, *Journal of Alloys and Compounds* 509 (2011) 8487-8492.
- [30] G. Brun, B. Gardes, J.C. Tedenac, A. Raymond, M. Maurin, *Materials Research Bulletin* 14 (1979) 743-749.
- [31] A. Powell, A. McDowall, I. Szkoda, K. Knight, B. Kennedy, T. Vogt, *Chemistry of Materials* 19 (2007) 5035-5044.
- [32] I. Szkoda, P. Vaqueiro, A. McDowall, A. Powell, C. Ritter, *Journal of Solid State Chemistry* 182 (2009) 2806-2814.
- [33] H. BARZ, *Materials Research Bulletin* 8 (1973) 983-988.
- [34] D. Brasen, J. Vandenberg, M. Robbins, R. Willens, W. Reed, R. Sherwood, X. Pinder, *Journal of Solid State Chemistry* 13 (1975) 298-303.
- [35] H. Muller, W. Kockelmann, D. Johrendt, *Chemistry of Materials* 18 (2006) 2174-2180.
- [36] R. Pocha, D. Johrendt, R. Pottgen, *Chemistry of Materials* 12 (2000) 2882-2887.

- [37] K. Kurosawa, S. Saito, Y. Yamaguchi, *Journal of the Physical Society of Japan* 52 (1983) 3919-3926.
- [38] V. Carreaux, D. Brunet, G. Ouvrard, G. Andre, *Journal of Physics-Condensed Matter* 7 (1995) 69-87.
- [39] B. Siberchicot, S. Jobic, V. Carreaux, P. Gressier, *Journal of Physical Chemistry* 100 (1996) 5863-5867.

## Chapter 2: Preparation and Characterisation

This chapter describes the experimental procedures utilised and background to the instrumentation techniques.

### 2.1 Synthesis

All materials have been prepared by reacting stoichiometric amounts of appropriate high purity elements in evacuated silica-glass tubes ( $\approx 10^{-4}$  torr). Syntheses typically required 3-4 firings at varying temperatures dependent on the system. After each firing the materials were homogenised and analysed by powder X-ray diffraction. Reactions were deemed completed when no further changes were observed in diffraction data. Thallium, vanadium, germanium and sulphur all needed to be treated prior to use in order to ensure single-phase products. The thallium was prepared by washing the oxidised granules in water before drying on a vacuum line and storing in the glovebox. Vanadium powder required the removal of surface  $V_2O_3$ . This was carried out by washing the green powder in a dilute hydrochloric acid solution until grey. The clean vanadium is then rinsed with distilled water and acetone before being dried on the vacuum line. Germanium required numerous (dependent on supplied batch) reductions under 5%  $H_2$  / 95%  $N_2$  gas at 823 K to remove  $GeO_2$ . Sulphur was dried on a vacuum line for 8 hours to remove traces of water. All elements were stored in a dry-box, unless otherwise stated. Initial stages of all thallium containing materials were carried out in an argon atmosphere glovebox.

### 2.2 Structural Characterisation

#### 2.2.1 Powder X-ray Diffraction [1]

Electromagnetic radiation waves of the magnitude  $\sim 1 \text{ \AA}$  are more commonly known as X-rays. X-rays result when electrons are accelerated through 30000 V and collide with matter. When these collisions occur the electrons are slowed down or stopped on impact resulting in a transfer of energy into electromagnetic radiation. The resulting 'white radiation' has wavelengths upwards of a minimum value given by,

$$\lambda_{\text{swl}} = \frac{12400}{V}$$

**Equation (6)**

where  $\lambda_{\text{swl}}$  is the short-wavelength limit (Å) and  $V$  is the accelerating voltage.

Most X-ray diffraction experiments utilise monochromatic radiation. Here a beam of electrons strike a metal target, for example copper, and ionise some of the  $1s$  ( $K$  shell) electrons. Energy is then released as outer electrons from the  $2p$  or  $3p$  transition to fill the vacant  $1s$  level. These transitions have fixed energy values and therefore a spectrum characteristic of the metal target is observed, Figure 11.

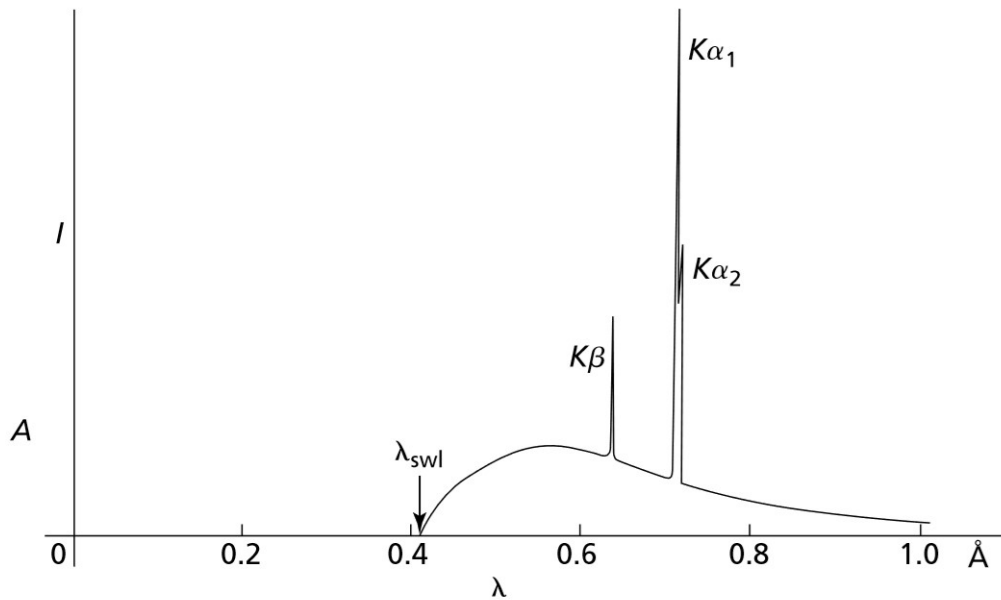


**Figure 11:** An X-ray spectrum showing the continuous ‘white radiation’ which peaks at about  $4/3 \lambda_{\text{swl}}$  and the sharp  $K_{\alpha 1}$  and  $K_{\alpha 2}$  peaks at wavelengths characteristic of the anode element, e.g. copper. [2]

For a copper target the  $2p \rightarrow 1s$  transition, known as  $K\alpha$ , has a wavelength of  $\lambda = 1.5418 \text{ \AA}$ ;  $3p \rightarrow 1s$  transition,  $K\beta$ ,  $\lambda = 1.3922 \text{ \AA}$ . The  $K\alpha$  transition occurs more frequently resulting in a more intense radiation; for this reason it is typically used in diffraction experiments. There are two possible spin states for the  $2p$  electron in the  $K\alpha$  transition which results in a doublet;  $K\alpha_1$  where  $\lambda = 1.54051 \text{ \AA}$  and  $K\alpha_2$  where  $\lambda = 1.54433 \text{ \AA}$ .

All of the samples were analysed by powder X-ray diffraction using a D8 Advance Bruker diffractometer fitted with a Bruker LynxEye linear detector. The D8 Advance uses germanium monochromated Cu-K $_{\alpha 1}$  radiation,  $\lambda = 1.54056 \text{ \AA}$ . Routine analysis, used to monitor the progress of reaction, was carried out in the range  $5 \leq 2\theta/^{\circ} \leq 85$ . For Rietveld analysis the angular range was increased to  $5 \leq 2\theta/^{\circ} \leq 120$ . The patterns were analysed in EVA [3] using PDFMaint [4] as the Reference Databases Manager together with the Inorganic Crystal Structure Database (ICSD) [5]. TOPAS [6] was utilised for the identification of single phase materials and the initial determination of unit cell lattice parameters. Data were then processed using The General Structural Analysis System (GSAS) [7].

### 2.2.2 Powder Neutron Diffraction [8]

Neutron investigations were carried out on Cr $_{1-x}$ In $_x$ GeTe $_3$  and GeV $_4$ S $_8$  samples at the ISIS facility, Rutherford Appleton laboratory, Chilton, United Kingdom.

When utilised in diffraction experiments, the neutron allows the complete description of the static arrangement and the displacement of atoms simultaneously. The convenient wavelengths (1 – 10  $\text{\AA}$ ) and available energy range (1 – 1000 meV, where  $1 \text{ meV} \approx 8 \text{ cm}^{-1}$ ) of neutrons facilitate the study of interatomic distances. Condensed matter exhibits vibrational energies equivalent to that of neutrons. The energy transfer from a molecule to a neutron is in the same range as that of the incident neutron and is therefore easily detected.

The scattering powers of neutrons and X-rays are markedly different. Neutrons are scattered by atomic nuclei and, due to their own magnetic moment, the magnetic moment of atoms. In contrast, X-rays are scattered by atomic electrons. The scattering power of X-rays therefore varies as a function of atomic number. For example, a very light atom, hydrogen, is a very weak scatterer of X-rays but a strong scatterer of neutrons. Neutrons therefore provide a means to differentiate between atoms and isotopes with similar X-ray scattering powers, e.g. Sn, In and  $^1\text{H}$ ,  $^2\text{H}$ .

For neutrons produced by spallation the entire neutron spectrum (variable wavelength) is used with a fixed diffraction angle,  $\theta$ . The wavelength,  $\lambda$ , depends on the velocity of the neutron given by the de Broglie relation:

$$\lambda = \frac{h}{mv}$$

**Equation (7)**

where  $h$  is Plank's constant,  $v$  is the velocity and  $m$  is the mass of a neutron.

Scattering from a crystal or polycrystalline material can be described in terms of reflection from a set of lattice planes. The condition for diffraction to take place is known as Bragg's law:

$$n\lambda = 2d \sin\theta$$

**Equation (8)**

In the time of flight (TOF) method  $\lambda$  and  $d$  are variables at fixed  $\theta$ .

When a neutron interacts with condensed matter it results in a combination of elastic and inelastic scattering. The overall scattering process is a superposition of each interaction. Different instruments have been designed in order to isolate a particular scattering process.

Magnetic behaviour depends on the presence of unpaired electrons. Neutrons possess a magnetic dipole moment ( $\mu_n = -1.913 \mu_n$ ) and therefore interact with the moment of unpaired electrons surrounding the nucleus. The interaction of a neutron with an unpaired electron results in magnetic scattering that can be used to determine unique spatial and dynamical information regarding the valence atomic orbitals. Magnetic scattering can result from both spin and orbital contributions. Magnetic Bragg peaks are observed in diffraction data when long-range magnetic order is present in a material. It is possible to determine the orientation of the atomic moments as the electron spin is a vector quantity. In this study, the Rietveld [9] refinement technique was used to simultaneously refine the magnetic and nuclear structure models using the GSAS software package.



The process starts with an ion source to produce  $H^-$ . These hydride ions are extracted and injected into a chain of linear accelerators. They are then stripped of their two electrons by a thin piece of aluminium oxide foil.  $H^+$  ions then enter the synchrotron and are accelerated to 800 MeV. The proton beam is trapped into two bunches and circulates approximately 10,000 times before being kicked out of the accelerator towards the heavy metal targets. Neutrons are generated when the 160 kW proton beam bombards a target comprising of a series of thin tungsten plates, clad in tantalum to prevent corrosion. Each collision causes a decay process resulting in 15 neutrons. The neutrons are then slowed down by various types of moderator. These moderators double the useful flux and dictate the energy of neutrons. Each moderator is surrounded by a beryllium reflector scattering neutrons back into the moderator. The moderators that are used at ISIS are water at room temperature, liquid methane at 100 K and liquid hydrogen at 20 K.

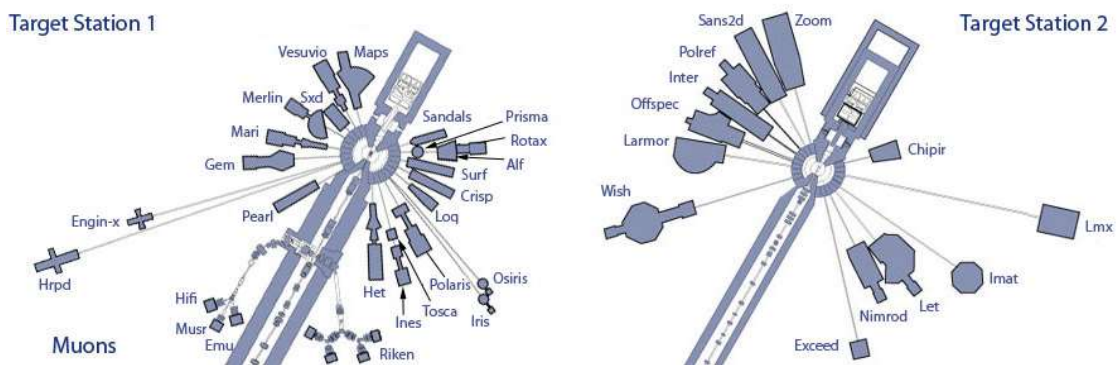


**Figure 12:** Schematic of the ISIS spallation neutron experiments, including TS2.[10]

Powder neutron diffraction data on  $Cr_{1-x}In_xGeTe_3$  were collected on the POLARIS Diffractometer [11, 12] at the ISIS facility. The POLARIS instrument is a high intensity, medium resolution powder diffractometer, Figure 13. It is located on ISIS beamline N7 and receives a polychromatic beam of neutrons from the ambient temperature water moderator.

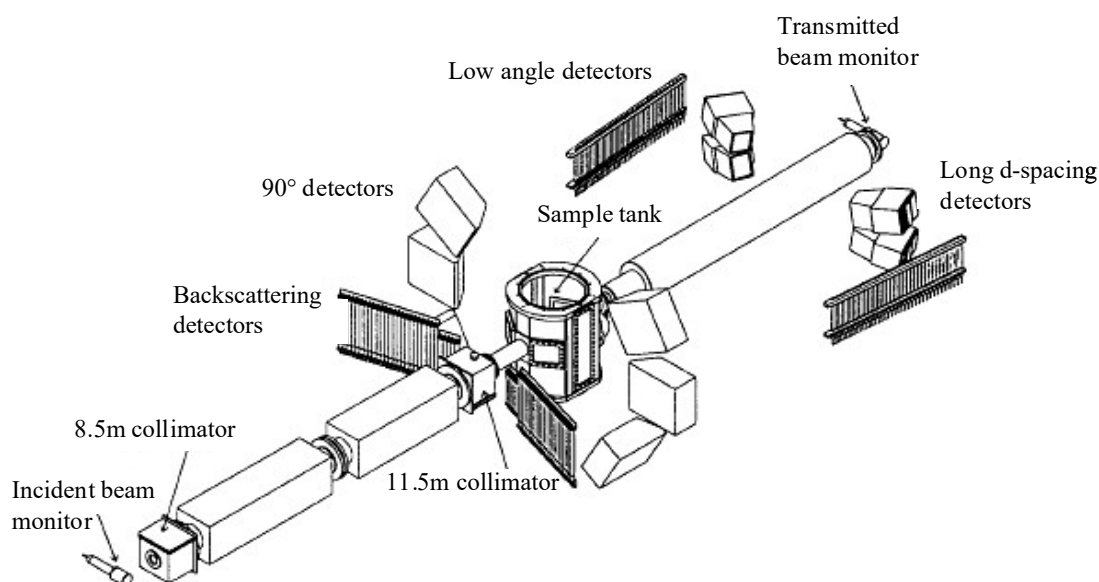


**Figure 13:** Schematic diagram of POLARIS instrument.

POLARIS provides a high count rate that allows experiments to be performed with short counting times or very little sample. The high count rate is a result of the intense neutron flux and the large detector solid angle. These crucial properties are exploited in kinetic experiments whereby diffraction patterns are collected while a furnace or cryostat is heating or cooling the sample. The 90° detector bank provides suitable collimation of the incident and scattered beams to ensure that signals from the surrounding sample environment apparatus can be eliminated. There are a total of 434 detectors arranged into four banks; two  $^3\text{He}$  gas tube detectors (bank A and C) and two ZnS scintillator detectors (bank B and E). A summary of the POLARIS detector banks is provided in Table 3.

**Table 3:** POLARIS detector configuration.

Bank	Low angle (A)	Low angle (B)	Backscattering (C)	90 degrees (E)
Detector type	$^3\text{He}$	ZnS	$^3\text{He}$	ZnS
No. of elements	$2 \times 40 = 80$	$2 \times 40 = 80$	$2 \times 29 = 58$	$6 \times 36 = 216$
$2\theta$ range	$28^\circ < 2\theta < 42^\circ$	$13^\circ < 2\theta < 15^\circ$	$130^\circ < 2\theta < 160^\circ$	$83^\circ < 2\theta < 97^\circ$
Resolution ( $\Delta d/d$ )	$\sim 1 \times 10^{-2}$	$\sim 3 \times 10^{-2}$	$\sim 5 \times 10^{-3}$	$\sim 7 \times 10^{-3}$
$d$ -range (Å)	0.5 – 8.3	0.5 – 21.6	0.2 – 3.2	0.2 – 4.0

For a set of detectors that are time focused the following apply:

For a given Bragg reflection:

$$n\lambda = n \frac{h}{mv} = n \frac{h}{n} \frac{t}{L} = 2d \sin \theta$$

**Equation (9)**

Where  $\lambda$  is the neutron wavelength,  $h$  is Planck's constant,  $m$  is the neutron mass,  $t$  is the total time of flight,  $L$  is the total flight path from the moderator to the detector,  $d$  is the interplanar spacing and  $2\theta$  is the Bragg scattering angle.

Substitution for  $h$  and  $m$  yields:

$$t (\mu\text{s}) = 505.56 L (\text{m}) \sin \theta d (\text{Å})$$

**Equation (10)**

or

$$d (\text{Å}) = \frac{1.977 \times 10^{-3}}{L(\text{m}) \sin \theta} t (\mu\text{s})$$

**Equation (11)**

From Equation (10) if the product,  $L\sin\theta$ , is identical for all detector elements in a bank, then neutrons scattered from a given  $hkl$  will reach the detectors in that bank at the same TOF.

The detectors on POLARIS are arranged into four discrete resolution focused banks. Here all the elements within each bank have an approximate constant resolution.

By partial differentiation of Equation (11) an expression can be derived to describe the resolution,  $\Delta d/d$ , of any detector.

$$R(d) = \frac{\Delta d}{d} = \left[ \Delta\theta^2 \cot^2 \theta + \left( \frac{\Delta t}{t} \right)^2 + \left( \frac{\Delta L}{L} \right)^2 \right]^{1/2}$$

**Equation (12)**

Equation (12) shows that for a given  $\Delta\theta$ , the contribution to  $\Delta d/d$  from the angular uncertainties increases as the scattering angle decreases. This contribution is infinite at  $2\theta = 0^\circ$  and zero at  $2\theta = 180^\circ$ . The  $\theta$  term dominates in the B bank (very low angle) whereby constant resolution is achieved by ensuring the  $\Delta\theta\cot\theta$  term is constant. Detectors of an identical size are placed along a straight line parallel to the incident neutron beam. Practically the detector modules in B bank of POLARIS are positioned  $\sim 10^\circ$  away from this ideal arrangement to increase the solid angle. In the C bank (large angle) the contribution of the  $\Delta\theta\cot\theta$  term is small and the resolution is dominated by time uncertainties,  $\Delta t/t$ . Detectors in the C bank are arranged in a straight line but are now inclined to the scattered neutron beam. All the detectors intersect approximately the same fraction of the Debye-Scherrer cones to give a constant resolution and line shape across the bank.

The decreased resolution of POLARIS in comparison to HRPD is a result of larger  $\Delta t/t$  values from Equation (12):  $\Delta t$  is approximately equal on the two instruments, but on HRPD  $t$  is a factor of 10 larger due to the increased neutron flight path. This results in a resolution 10 times greater on HRPD.

During the experimental work at ISIS, data were collected on *ca.* 2g of sample loaded into a vanadium sample can. Room temperature collections were

carried out by mounting the sample can on a candlestick. The sample can is mounted 314 mm from the lower face of the aluminium plate on the candlestick, Figure 14. This ensures the centre of the sample is in the centre of the neutron beam.

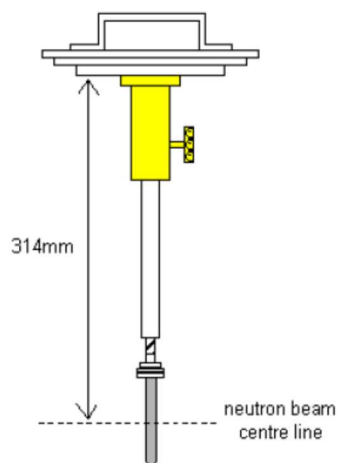


**Figure 14:** Sample alignment on POLARIS candlestick.

Variable temperature measurements were carried out using a standard RAL orange cryostat. The initial data processing was performed using Ariel spectrum manipulation software.

Powder neutron diffraction data on  $\text{GeV}_4\text{S}_8$  were collected on the high resolution powder diffractometer, HRPD [13] at the ISIS facility, Figure 15. HRPD has approximately a 100 m flight path. This long flight path is necessary in order to negate the small flight path uncertainty ( $\sim 5$  cm) introduced largely because of the finite moderator depth. Flux intensity usually follows an inverse-square fall-off with distance. HRPD incorporates a neutron guide in order to ensure that the extended flight path does not result in unworkable flux intensities. With a neutron guide the flux intensities at  $1\text{\AA}$  and  $2\text{\AA}$  on HRPD are roughly equivalent to 40 m and 18 m flight paths respectively without a guide. The neutron guide is a Ni plated glass along which neutrons travel by total external reflection. A curved section of the guide eliminates the potentially damaging high energy neutrons. The shallow radius of the curvature allows transmission of sub- $\text{\AA}$  neutrons.

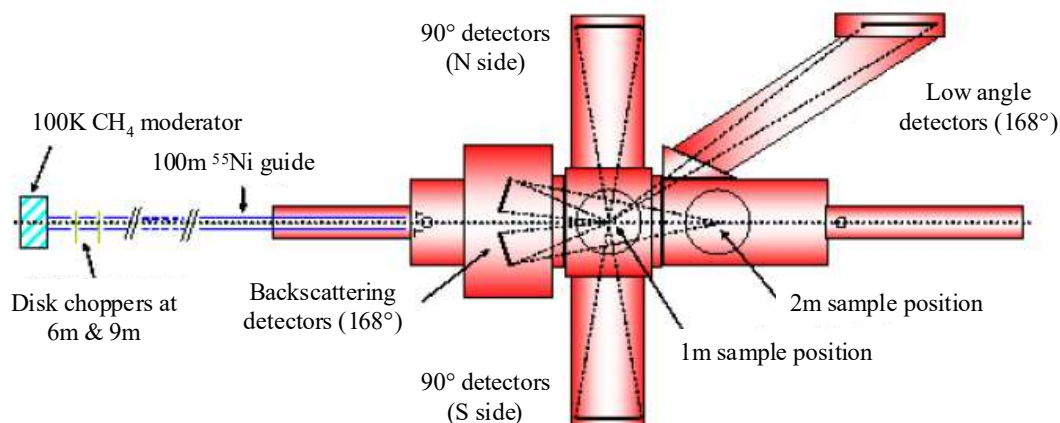


**Figure 15:** Schematic of HRPD.

The long flight path of HRPD introduces a ‘frame overlap’ problem of successive neutron pulses. This issue is eliminated by the use of two disk choppers. HRPD is sited on a 50 Hz source and without the choppers a wavelength band of  $0.2 \text{ \AA}$  could be successfully utilised. The choppers are situated 6 m and 9 m away from the moderators. The 6 m chopper rotates at ISIS frequency and acts as a wavelength selector. The offset time of the 6 m chopper relative to  $t = 0$  can be varied to optimise when the disk aperture is open to the beam. The 9 m chopper prevents frame overlap by rotating at a frequency of  $(50/n) \text{ Hz}$ , where  $n = 1, 2, 3, 5$  and  $10$ , and closing at appropriate times. The wavelength window may therefore be increased but with a loss of relative intensity. Typically wavelength windows of  $2 \text{ \AA}$  and  $1 \text{ \AA}$  are achieved with frequencies of 5 Hz and 10 Hz respectively.

HRPD operates with three fixed angle banks; a backscattering, a  $90^\circ$  and a low angle bank, their configuration is shown in Figure 15. Traditionally there were two positions into which the samples could be loaded; one 1m and the other 2m away from the backscattering bank. Diffraction data can now be recorded simultaneously in all three banks from the 1m position due to the addition of a ZnS detector in the backscattering bank. A summary of each detector bank is provided in Table 4.

**Table 4:** HRPD detector characteristics.

Bank	Low angle	Backscattering	90 degrees
Detector type	$^3\text{He}$	ZnS	ZnS
No. of elements	72	720	396
$2\theta$ range	$28^\circ < 2\theta < 32^\circ$	$130^\circ < 2\theta < 160^\circ$	$83^\circ < 2\theta < 97^\circ$
Resolution ( $\Delta d/d$ )	$\sim 2 \times 10^{-2}$	$\sim 4-5 \times 10^{-4}$	$\sim 2 \times 10^{-3}$
$d$ -range (Å)	$\sim 2.2 - 16.5$	$\sim 0.6 - 4.6$	$\sim 0.9 - 6.6$

The backscattering bank contains a total of 720 discrete detector elements. These ZnS elements are separated into eight octants. Typically these octants are software linked to form 60 rings in order to minimise geometric aberration. The 90° bank comprises six modules, each with 66 elements. Each module is positioned equidistance from the 1m sample position. Again these octants are more commonly software configured into 66 radial segments. The low angle bank is made up of 72  $\text{He}^3$  ½” tubes. They lie on a constant radius to the through beam and can be linked as previously described. The low angle bank is isolated from the other two banks. In order to minimise angular divergence of the long secondary flight path, the detector elements are housed in an Ar filled tank.

During the experimental work on HRPD, data were collected on *ca.* 3g of sample loaded into a vanadium slab. Variable temperature measurements were carried out using a standard RAL orange cryostat. The initial data processing was performed using Ariel spectrum manipulation software.

### 2.2.3 The Rietveld Method

The structures of all the materials investigated have been refined from powder X-ray and, in some cases, neutron diffraction data using the Rietveld method. [9] The GSAS software package was used to implement this method [7].

For a Rietveld refinement it is crucial that the diffraction data is collected appropriately. The geometry of the diffractometer, the type of radiation and the preparation of the sample are all important factors when designing diffraction experiments. The experimental data is of a digital format describing a collection of individual reflection profiles, where each profile

has a peak height, position, breadth and decays gradually from the peak position. The Rietveld method involves analysing overall line profiles rather than measuring the position and intensity of individual peaks. As the method is not a structure determination method it is crucial that the initial model describes the diffraction data sufficiently well. Rietveld analysis requires that an initial structural model is refined, by way of a least squares method, to best fit the experimental diffraction data. The whole calculated profile is directly compared to the experimental data and a weighted difference,  $S_y$ , between the two determined. Ideally  $S_y = 0$ .

$$S_y = \sum_i w_i (y_i - y_{ci})^2$$

**Equation (13)**

where  $w_i = 1/y_i$ ,

$y_i$  = observed (gross) intensity at the  $i$ th step,

$y_{ci}$  = calculated intensity at the  $i$ th step,

and the sum is over all data points.

The integrated area of a reflection profile is proportional to the Bragg intensity,  $I_K$ , where  $K$  represents the Miller indices,  $h, k, l$ .  $I_K$  is proportional to the absolute square of the structure factor.

$$I_K \propto |F_K|^2$$

**Equation (14)**

Typically many Bragg reflections contribute to the intensity,  $y_i$ , observed at step  $i$  as the profiles are not usually completely resolved. The calculated intensities,  $y_{ci}$ , are determined from  $|F_K|^2$  values in the structural model; this emphasises the need for a good structural model in the first instance.  $y_{ci}$  are found by summing of the calculated contributions from neighbouring Bragg reflections plus the background.

$$y_{ci} = S \sum_K L_K |F_K|^2 \phi(2\theta_i - 2\theta_K) P_K A + y_{bi}$$

**Equation (15)**



where  $S$  is the scale factor,

$K$  represents the Miller indices,  $h k l$ , for a Bragg reflection,

$L_K$  contains the Lorentz, polarization and multiplicity factors,

$\emptyset$  is the reflection profile function,

$P_K$  is the preferred orientation function,

$A$  is the absorption factor

$F_K$  is the structure factor for the  $K$ th Bragg reflection, and

$y_{bi}$  is the background intensity at the  $i$ th step.

$$y_{bi} = \sum_{m=0}^5 B_m \left[ \frac{2\theta_i}{\text{BKPOS}} - 1 \right]^m$$

**Equation (16)**

where BKPOS is the user-specified origin in the input control file.

The structure factor,  $F_K$ , is given by,

$$F_K = \sum_j N_j f_j e^{2\pi i(hx_j + ky_j + lz_j)} e^{-M_j}$$

**Equation (17)**

where  $N_j$  is the site occupancy multiplier for the  $j$ th atom site,

$f_j$  is the scattering factor of the  $j$ th atom,

$h, k$  and  $l$  are Miller indices,

$x_j, y_j$  and  $z_j$  are the positional coordinates of the  $j$ th atom in the unit cell,

$M_j = 8\pi^2 \overline{u_s^2} \sin^2 \theta / \lambda^2$  and

$\overline{u_s^2}$  is the root-mean-square of the thermal motion of the  $j$ th atom parallel to the diffraction vector.

The Rietveld refinement process will continue until the residual, Equation (13), is minimised. The success of this procedure depends on the strength of the model and whether or not a global minimum is reached. The refinement must be monitored to ensure it is proceeding satisfactorily and to determine

when the process is complete. R-values have been developed in the Rietveld method to numerically represent the criteria of fit. ‘R-weighted pattern’,  $R_{wp}$ , best reflects the progress of the refinement as the numerator is the residual that is being minimised.

$$R_{wp} = \sqrt{\frac{\sum w_i (y_i(\text{obs}) - y_i(\text{calc}))^2}{\sum w_i (y_i(\text{obs}))^2}}$$

**Equation (18)**

Another widely utilised criterion is  $\chi^2$ , also known as the ‘goodness-of-fit’.

$$\chi^2 = \left[ \frac{S_y}{(N - P)} \right]^{1/2} = \frac{R_{wp}}{R_e}$$

**Equation (19)**

where  $N$  is the number of profile points,  $P$  is the number of refined parameters and  $R_e$ , ‘R-expected’, takes the form:

$$R_e = \left[ \frac{N - P}{\sum w_i y_{oi}^2} \right]^{1/2}$$

**Equation (20)**

A  $\chi^2$  value of less than 5 is generally thought to be satisfactory. The value of  $\chi^2$  can be distorted by statistical errors and a well fitted background may artificially lower the value.

#### **2.2.4 Thermogravimetric Analysis (TGA)**

Sample mass as a function of temperature has been determined using a DuPont Instruments 951 Thermogravimetric Analyser. The sulphur content of defect thiospinel,  $\text{GeV}_4\text{S}_8$ , was determined thermogravimetrically by oxidation. A Sample of 10-20 mg was loaded into a quartz crucible mounted in a platinum wire cage suspended from the balance arm. Measurements were

performed under a flow of oxygen ( $60 \text{ cm}^3 \text{ min}^{-1}$ ) and heated to 1273 K at  $2 \text{ K min}^{-1}$ . In order to ensure complete conversion to oxides the maximum temperature was maintained for 30 minutes.

## 2.3 Physical Property Studies

### 2.3.1 Electron Transport Measurements

The four probe method is the most commonly used technique for the measurement of resistivity. It is typically a non-destructive method. A known current,  $I$ , is passed between the two outer probes and the potential developed across the inner probes is measured. The resistance,  $R$ , of the material is first calculated before taking into account the dimensions of the pellet using Equation (21).

$$\rho = R \times \frac{A}{l}$$

**Equation (21)**

where  $\rho$  is the resistivity,  $A$  is the cross-sectional area and  $l$  is the distance between in the inner probes.  $A$  and  $l$  varied with every pellet prepared and were measured using a micrometer. The resistivity of a semiconductor is defined by:

$$\rho = \frac{1}{q(n\mu_n + p\mu_p)}$$

**Equation (22)**

where  $n$  and  $p$  are the free electron and hole concentrations;  $\mu_n$  and  $\mu_p$  are the electron and hole mobilities respectively;  $q$  is the magnitude of electronic charge ( $1.6021 \times 10^{-19} \text{ C}$ ) [14].

The electrical conductivity is the inverse of the resistivity.

Electrical Resistivity measurements were carried out in the temperature range  $100 \leq T/\text{K} \leq 400$  using a standard four-point probe technique. The samples were cold pressed under 10 tons of pressure and sintered in evacuated

( $\approx 10^{-4}$  torr) silica glass tubes. A bar-shaped ingot, of approximate  $8 \times 3 \times 1$  mm dimensions, was then cut from the sintered pellet. Using colloidal silver conducting paint four  $50 \mu\text{m}$  silver wires were attached at equal spacings along the pellet. The sample was then connected to an 8 pin DIL socket by silver wires, fixed in position by silver paint. The socket was mounted on a sample stick with external connections to an HP 34401A multimeter, and placed in an Oxford Instruments CF1200 cryostat connected to an ITC502 temperature controller. A schematic of the experimental setup is shown in Figure 16. The measurements were carried out using liquid nitrogen as a coolant. Data was collected under computer control using LabView written by Dr. P. Vaqueiro.

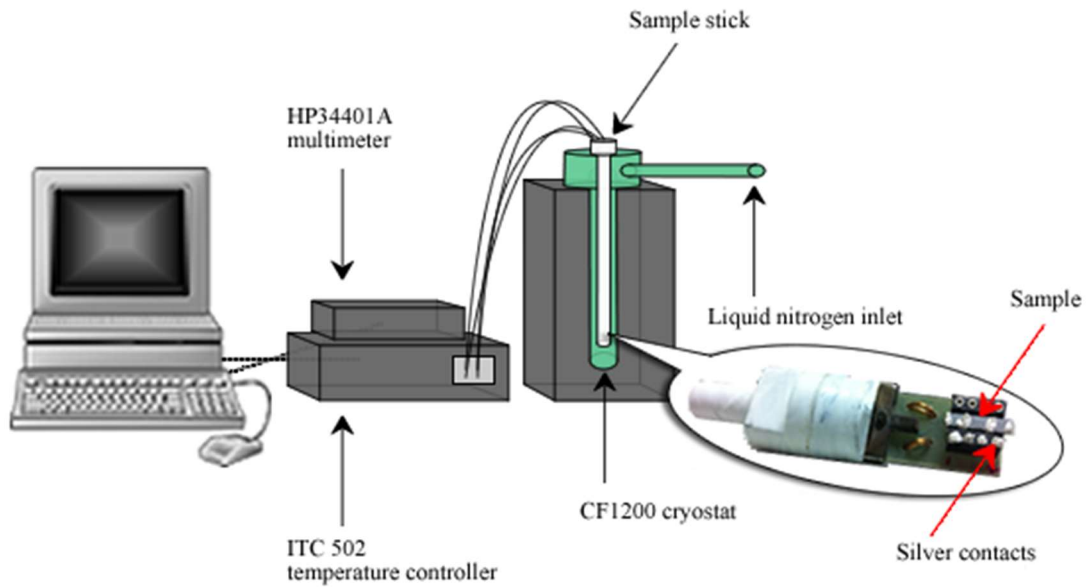


**Figure 16:** Experimental setup for 4-probe electrical resistivity measurements.

### 2.3.2 Seebeck Measurements

A thermal electromotive force is generated when a temperature gradient is applied across a material. This is known as the Seebeck effect. It is reversible and results from the changes in Fermi level with temperature [15]. By experimental determination of the Seebeck coefficient, the carrier type and concentration can be extracted. The Seebeck coefficient is typically higher in semiconductors than in metals.

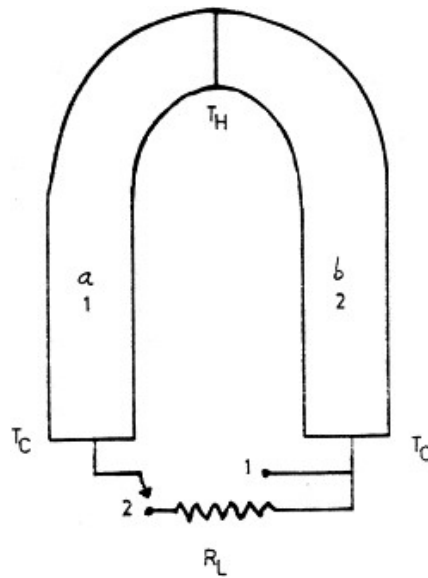


**Figure 17:** The Seebeck effect [16].

The Seebeck voltage is the open circuit voltage for zero current. If the junction between two unlike conductors  $a$  and  $b$  (Figure 17) is kept at two different temperatures  $T_H$  and  $T_C$ , where  $T_H > T_C$ , an open circuit potential is developed.

$$V = a_{ab}(T_H - T_C)$$

**Equation (23)**

The Seebeck coefficient or thermoelectric power,  $S$ , is the limit of the measured thermo-e.m.f.,  $\Delta V$ , across a thermoelectric material when applying a temperature gradient,  $\Delta T$ , and is defined by Equation (24) [17].

$$S = \lim_{\Delta T \rightarrow 0} \left( \frac{\Delta V}{\Delta T} \right)$$

**Equation (24)**

The relative Seebeck e.m.f. is often incorrectly described as being a consequence of the external contact potential between dissimilar materials. The external contact effect, however, is not a thermoelectric effect. When two materials are brought close enough together that electron transfer can result in a common Fermi energy level in each they are said to have induced an

external contact potential. This induction is not temperature dependent and vanishes when the materials touch [18].

The Seebeck coefficient was measured over the temperature range  $100 \leq T/K \leq 300$  on an ingot cut from a sintered pellet. The pellet was mounted onto two copper blocks using silver conductive adhesive. Two 50  $\mu\text{m}$  copper wires were attached to each end of the sample and connected to a Keithley 2182A nanovoltmeter. Two Au: 0.07 % Fe vs. chromel thermocouples were placed close to the samples at the cold and hot ends and connected to a Lakeshore LS-331 temperature controller. The hot end copper block incorporates a 120  $\Omega$  strain gauge that acts as a heat source. The heater forms the hot stage of a closed cycle system (Advanced Research Systems, CSW-202AI closed cycle system), controlled by another Lakeshore LS-331 temperature controller. Data was collected under computer control using LabView written by Dr. P. Vaqueiro of this Department.

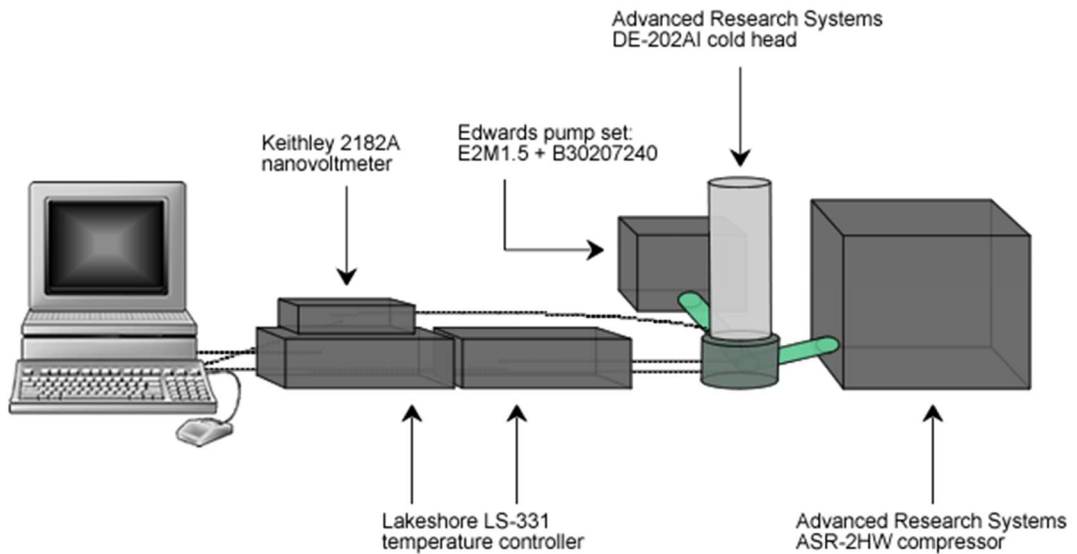


**Figure 18:** Experimental setup for Seebeck coefficient measurements.

### 2.3.3 Thermal Conductivity Measurements

The thermal conductivity has two contributions. The first is from the electrical carriers,  $\kappa_e$ , and the other is from lattice vibrations,  $\kappa_{\text{ph}}$  (phonons). Generally  $\kappa_{\text{ph}}$  is much greater than  $\kappa_e$ . The concept is to minimise  $\kappa_{\text{ph}}$  by using elements with high atomic masses. High atomic masses reduce the vibrational frequency. Low vibrational frequencies result in a reduced mobility of

electrons (charge carriers), thus the current is reduced, the resistance is increased and therefore higher electrical resistivity is observed. The presence of a large number of atoms ( $N$ ) per unit cell also lowers the fraction of vibrational modes (phonons) that carry heat efficiently to  $1/N$ . Thus reducing the thermal conductivity, but possibly raising the electrical conductivity.

The Anter Flashline 3000 System was used to determine the thermal conductivity. Measurements were made on 13 mm diameter pellets coated in graphite, typically *ca.* 1 mm thick. The Flashline uses a transient method, the Flash Method[19]. A heating pulse is provided at one side of a 13 mm diameter pellet. On the opposite side infrared radiation is recorded as a function of time using a cooled InSb detector. This is used to compute the time-dependent temperature rise.

It is necessary to know the amount of energy absorbed in the front surface in order to calculate the thermal diffusivity and heat capacity. The product of the density and the heat capacity of the material is given by:

$$DC = Q/LT_M$$

**Equation (25)**

Where  $D$  is the density in  $\text{g/cm}^3$ ,  $C$  is the heat capacity in  $\text{cal/g}^\circ\text{C}$ ,  $Q$  is the radiant energy of the pulse in  $\text{cal/cm}^2$ ,  $L$  is the thickness of the sample in cm and  $T_M$  is the maximum temperature at the rear surface in K. The thermal conductivity is then found using the relationship:

$$\kappa = \alpha DC$$

**Equation (26)**

Where  $\alpha$  is the thermal diffusivity in  $\text{m}^2/\text{s}$  and can be calculated in two ways[20]. The Flashline 3000 uses the general relation:

$$\alpha = \frac{K_x}{t_x} l^2$$

**Equation (27)**

Where  $l$  is the thickness of the sample in m,  $K_x$  is a dimensionless constant depending on  $t_x$ , the x percent raise of temperature in seconds. The software then uses different x values (25, 50, 75) to compare the calculated diffusivity values to assess the quality of the response curve.

### 2.3.4 Magnetic Susceptibility Measurements [21]

A magnetic field produces lines of force that penetrate the medium to which the field is applied. The density of these lines of force is known as the magnetic flux density. The magnetic field,  $H$  and the magnetic flux density,  $B$  are related by the permeability of free space,  $\mu_0$ , in a vacuum,

$$B = \mu_0 H$$

**Equation (28)**

If a magnetic material is placed in an applied magnetic field, the induced field of the material is called the magnetisation,  $M$ . Therefore the magnetic flux density is now given by,

$$B = \mu_0 (H + M)$$

**Equation (29)**

The magnetic susceptibility is the magnetisation induced by unit applied magnetic field.  $\chi_m$  is dimensionless as a result of the units of  $\mu_0$ .

$$\chi_m = \frac{M}{H}$$

**Equation (30)**

The molar susceptibility in  $\text{m}^3 \text{mol}^{-1}$ , is of more general use, i.e. the susceptibility per mole of substance, given by:

$$\chi_{mol} = \frac{\chi_m M_r}{10^3 \rho}$$

**Equation (31)**



where  $M_r$  (in  $\text{g mol}^{-1}$ ) is the relative molecular mass and  $\rho$  ( $\text{kg m}^{-3}$ ) is the density. If  $\chi_{mol}$  is quoted in cgs/-emu terms it can be converted into S.I. units through multiplication by  $4\pi \times 10^{-6}$ .

Magnetic data for  $\text{Cr}_{1-x}\text{In}_x\text{GeTe}_3$  ( $0 \leq x \leq 1$ ) materials were measured using a Quantum Design Magnetic Property Measurement System (MPMS<sup>®</sup>) Superconducting Quantum Interference Device (SQUID). SQUIDs detect changes in minute magnetic fields, can measure voltages as low as  $10^{-18}$  V, currents of  $10^{-18}$  A, magnetic fields of  $10^{-14}$  T and magnetic moments with resolution of  $5 \times 10^{-12}$  A m<sup>2</sup>. The SQUID measures the changes in magnetic flux as the sample moves through a system of superconducting detection coils, approximately 11cm below the magnet. The coils are connected to the SQUID by superconducting wires. This allows the current from the detection coils to inductively couple the SQUID sensor. The SQUID produces an output voltage that is proportional to the current flowing in the SQUID input coil. Hence the SQUID is functioning as a sensitive current-to-voltage converter. As the sample moves through the superconducting detection coils, the magnetic moment of the material induces an electric current in the coils. The change in persistent current of the detection circuit is proportional to the change in magnetic flux. Variations of the current within the detector coils result in a variation of the output voltage of the SQUID which is proportional to the magnetic moment of the sample.

SQUID measurements were carried out in the Materials Characterisation Laboratory (R53) at ISIS, Didcot, UK. Samples of *ca.* 40 mg were weighed and loaded into gelatine capsules of a known weight. The capsule was then placed in the middle of a plastic drinking straw. The bottom end of the straw was taped over to prevent accidental loss of sample. Small holes were punctured in the straw above and below the sample capsule to allow air flow. The straw was attached to the sample stick, placed in the sample transport and the airlock was evacuated. The sample then lowered into the cryostat and centred in the second-order gradiometer pickup coil to ensure uniform magnetisation of the sample. Data were typically collected over  $5 \leq T/\text{K} \leq 300$  in a zero-field-cooled/field-cooled (*zfc / fc*) measurement. This type of sequence provides a means of observing hysteresis. *zfc* measurements were carried out by cooling the sample to the lowest temperature when

$H = 0$ . After a 5 minute equilibrium period a magnetic field ( $H = 100$  G) was applied and the magnetisation as a function of temperature measured. *fc* measurements were carried out as above but by cooling the sample in  $H = 100$  G field, rather than zero-field. At low temperatures (5 – 150 K) data was generally collected in 5 K steps. The step size was increased to 10 K at higher temperatures (150 – 300 K). Magnetisation as a function of field ( $0 \leq H/G \leq 50000$ ) was carried out for  $\text{Cr}_{0.9}\text{In}_{0.1}\text{GeTe}_3$ ,  $\text{Cr}_{0.5}\text{In}_{0.5}\text{GeTe}_3$  and  $\text{Cr}_{0.2}\text{In}_{0.8}\text{GeTe}_3$  samples at 5 K, 100 K and 200 K.

The SQUID output is raw magnetisation,  $M_{\text{raw}}$ , as a function of temperature or field. The raw magnetisation data must be corrected for diamagnetism exhibited by the gelatine capsule. The capsule magnetisation is given by:

$$M_{\text{capsule}} = -3.188 \times 10^{-10} \times \text{mass of capsule (mg)} \times H \text{ (G)}$$

**Equation (32)**

Hence,

$$M_{\text{corr}} = M_{\text{raw}} - M_{\text{capsule}}$$

**Equation (33)**

The corrected magnetisation allows the calculation of  $\chi_{\text{mol}}$ :

$$\chi_{\text{mol}} = \frac{M_{\text{corr}}}{nH}$$

**Equation (34)**

where  $n$  is the number of moles of a sample. The molar susceptibilities are then corrected for core diamagnetism using Pascal's constants.

$$\chi_{\text{mol}}^{\text{corr}} = \chi_{\text{mol}} - \chi_{\text{dia}}$$

**Equation (35)**

where  $\chi_{\text{dia}}$  is the sum of the diamagnetic contributions from the component ions.

Using Curie Law, Equation (3), a plot of  $1/\chi_{\text{mol}}$  against  $T$  results in a straight line that extrapolates to 0 K when a substance shows no tendency to order magnetically.

Curie-Weiss behaviour, Equation (36), is often observed when a material shows a tendency to magnetically order. A plot of  $1/\chi_{\text{mol}}$  against  $T$  should result in a straight line above the ordering temperature, with gradient  $1/C$  and intercept  $-\theta/C$ .

$$\frac{1}{\chi_{\text{mol}}} = \frac{T}{C} - \frac{\theta}{C}$$

**Equation (36)**

The Curie constant can then be used to calculate the effective magnetic moment as follows:

$$\mu_{\text{eff}} = \sqrt{\frac{8C}{m}}$$

**Equation (37)**

where  $m$  is the number of magnetic ions per formula unit.

It is regarded that magnetic properties arise from spin or electrical orbital motion. In transition metals, agreement between experimentally observed and theoretical magnetic moments can be found from the spin-only formula, Equation (38), where the orbital contribution is zero in most cases.

$$\mu_s = g\sqrt{S(S+1)}$$

**Equation (38)**

where  $S$  is the sum of the spin quantum numbers for each unpaired electron.

## 2.5 References

- [1] A.R. West, *Solid State Chemistry and its Applications*. John Wiley & Sons, LTD, 1984.
- [2] C. Hammond, *The Basics of Crystallography and Diffraction*. OUP Oxford, 2009.
- [3] *Bruker DIFFRAC<sup>plus</sup> Evaluation Package – EVA V13*. 2007.
- [4] *PDF-2*. 2006.
- [5] D.A. Fletcher, R.F. McMeeking, D. Parkin, *Journal of Chemical Information and Computer Sciences* 36 (1996) 746-749.
- [6] B.A. Bruker AXS: TOPAS V3: General profile and structural analysis software for powder diffraction data. – User’s Manual, Karlsruhe, Germany, 2005.
- [7] A.C. Larson, R.B. Dreele, *General Structural Analysis System (GSAS)*. Los Alamos National Laboratory Report, LAUR 86-748 (2004).
- [8] <http://www.isis.stfc.ac.uk/about/how-isis-works---in-depth4371.html>.
- [9] H. Rietveld, *Journal of Applied Crystallography* 22 (1967) 151-152.
- [10] [www.isis.stfc.ac.uk](http://www.isis.stfc.ac.uk).
- [11] R.I. Smith, S. Hull, *User Guide for the Polaris Powder Diffractometer at ISIS*. **RAL-TR-97-038**, ISSN 1358-6254.
- [12] S. Hull, R.I. Smith, W.I.F. David, A.C. Hannon, J. Mayers, R. Cywinski, *Physica B: Condensed Matter* 180–181, Part 2 (1992) 1000-1002.
- [13] <http://www.isis.stfc.ac.uk/instruments>.
- [14] D.K. Schroder, *Semiconductor Material and Device Characterisation*. John Wiley & Sons Inc., 1990.
- [15] R.R. Heikes, R.W. Ure, *Thermoelectricity: Science and Engineering*. Interscience Publishers, 1961.
- [16] Z. Dughaish, *Physica B-Condensed Matter* 322 (2002) 205-223.
- [17] J. Tauc, *Photo and Thermoelectric Effects in Semiconductors*. Pergamon Press, 1962.
- [18] D.M. Rowe, *CRC Handbook of Thermoelectrics*. CRC Press LLC, 1995.

- [19] R.T. Littleton IV, J. Jeffries, M.A. Kaeser, M. Long, T. Tritt, Fall Materials Research Society, Symposium Z: Thermoelectric Materials, Boston, 1998.
- [20] W.J. Parker, R.J. Jenkins, C.P. Butler, G.L. Abbott, *Journal of Applied Physics* 32 (1961) 1679-1684.
- [21] L.E. Smart, E.A. Moore, *Solid State Chemistry: An Introduction, Fourth Edition*. Taylor & Francis, 2012.

## Chapter 3: Structural Transitions in GeV<sub>4</sub>S<sub>8</sub>

### 3.1 Introduction

This chapter presents the results of an investigation into the defect thiospinel, GeV<sub>4</sub>S<sub>8</sub>. GeV<sub>4</sub>S<sub>8</sub> has been successfully synthesized in order to investigate the structural properties as a function of temperature. High Resolution Powder Diffraction (HRPD) experiments have been completed at ISIS.

### 3.2 Background

The spinel structure is often adopted by materials with the general formula AB<sub>2</sub>S<sub>4</sub>. Here one-third of the cations occupy tetrahedral sites and the remaining two-thirds are octahedrally coordinated. These compounds are generally only single-phase at stoichiometric compositions and present interesting structural [1] and physical properties. There are spinels that exhibit magnetoresistance [2-4]; those whose magnetic behaviour is dominated by antiferromagnetic interactions and those where ferromagnetic interactions dominate [5-9]. Sn-In sulphides with spinel structure have been utilised as lithium insertion host-matrix for solid state lithium batteries. [10]

There is a small family of non-stoichiometric, spinel-related materials that exist. These compounds are 50% deficient at the A-cation site and result in ternary phases with the general formula AB<sub>4</sub>S<sub>8</sub>, where A = Ga, Al, Ge, Fe-Ni, Zn and B = Mo, V, Nb, Ta, (Mo/Re). [11] GeV<sub>4</sub>S<sub>8</sub> comprises of (GeS<sub>4</sub>)<sup>4+</sup> tetrahedra and cubane-like (V<sub>4</sub>S<sub>4</sub>)<sup>4-</sup> units ordered in a rocksalt arrangement [12]. The (V<sub>4</sub>S<sub>4</sub>)<sup>4-</sup> unit incorporates a tetrahedral V<sub>4</sub>-cluster that is instrumental in directing structural and physical changes of the compound. GeV<sub>4</sub>S<sub>8</sub> is an antiferromagnetic ( $S = 1$ ) cluster compound with Néel-temperature,  $T_N = 15$  K. Chudo *et al.* previously suggested two structural phase transitions existed; the first from a cubic to a rhombohedral phase at  $T_S = 33$  K, followed by the onset of an orthorhombic phase at  $T_N$  [13]. Bichler *et al.*, however, report no transformation to a rhombohedral phase and observe only the onset of a orthorhombic (*Imm2*) phase at 30 K [14]. This investigation sought to conclusively determine the low temperature structure

and rationalise the physical behaviour associated with it in order to facilitate the structure determination of other related phases.

### 3.3 Synthesis

The compound  $\text{GeV}_4\text{S}_8$  has been synthesized by high-temperature solid-state reaction. Stoichiometric amounts of high-purity germanium, vanadium and sulphur were ground in an agate mortar and loaded into a silica tube. In order to suppress the formation of  $\text{V}_3\text{S}_4$  *ca.* 20 mg of iodine was added to the *ca.* 10 g reaction mixture. The silica tubes were evacuated to  $\leq 10^{-4}$  Torr and sealed. Liquid nitrogen was used to cool the sample prior to sealing to prevent iodine sublimation. Samples were fired at 1003 K for 24 hours then transferred to a tube furnace for four hours. The three zone tube furnace was set to 937 K at the sample end of the sealed tube and 1003 K at the empty end. The cold end was set to cool prior to the hot end. This ensured the reaction mixture could be removed from the tube in its entirety before being ground and re-fired for a further 48 hours. Reaction mixtures were initially inserted into a pre-heated furnace and upon completion of the heating period were allowed to cool at the natural rate of the furnace. In subsequent firings the tubes were placed into room temperature furnaces and heated up to the required temperature.  $\text{GeV}_4\text{S}_8$  is a fine, loose, dark grey powder.

### 3.4 Results

#### 3.4.1 Characterisation

$\text{GeV}_4\text{S}_8$  was initially characterised by laboratory powder X-ray diffraction. These data can be indexed on the basis of a face-centred cubic unit cell. Structural refinements were initiated in the cubic space group  $F\bar{4}3m$  using atomic coordinates and lattice parameters previously determined. Lattice parameters were obtained by Rietveld analysis using GSAS [15] and are in excellent agreement to those previously reported [12].

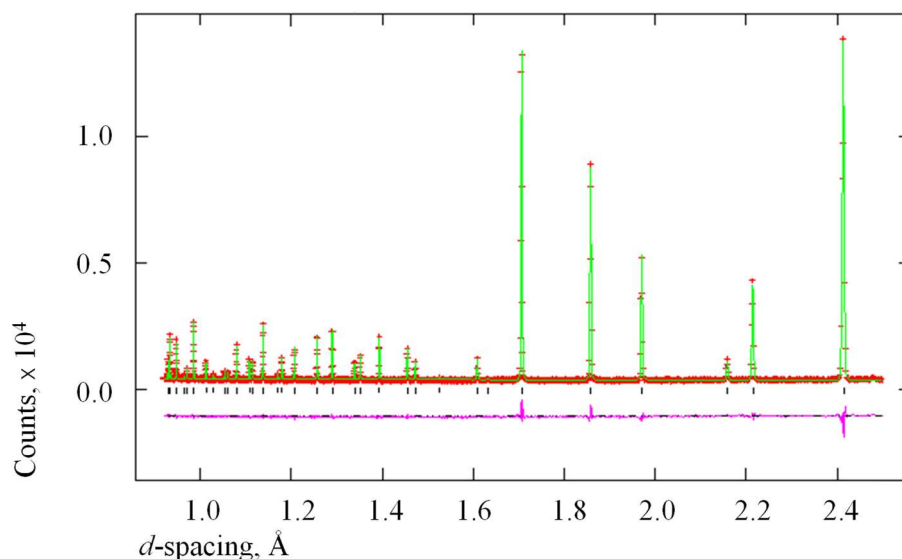


**Figure 19:** Final observed (crosses), calculated (upper full line) and difference (lower full line) X-ray diffraction profile at room temperature of GeV<sub>4</sub>S<sub>8</sub>. Reflection positions are marked.

The sulphur content of GeV<sub>4</sub>S<sub>8</sub> was determined by thermogravimetric analysis, Figure 20. Several runs were completed and an average taken, the calculated composition was GeV<sub>4</sub>S<sub>8.00</sub>. The sulphur content affects the oxidation state of vanadium and hence the number of *d*-electrons available to the V<sub>4</sub>-cluster. This type of defect thiospinel is often found to be non-stoichiometric and is extremely tolerant to an excess or deficiency on either the 4(*a*) or 16(*e*) site [16, 17].

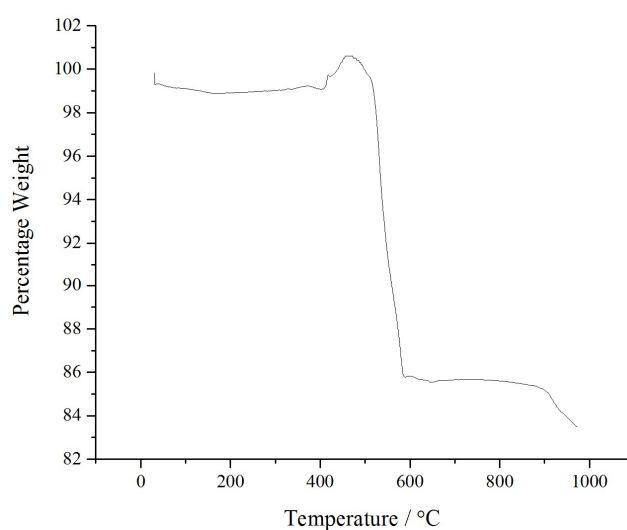


**Figure 20:** Thermogravimetric analysis data for GeV<sub>4</sub>S<sub>8</sub>.



### 3.4.2 High temperature X-ray diffraction

High temperature X-ray diffraction experiments have been carried out on a D8 Advance Bruker diffractometer fitted with a Bruker LynxEye linear detector and an Anton Paar furnace. The system was calibrated using an  $\alpha$  quartz standard and adjusting the sample height to provide lattice parameters according to the National Bureau of Standards [18]. Measurements were carried out in 50° steps up to 800°C with a continuous flow of oxygen free nitrogen. The gas supply line was fitted with a flow meter and two cleaning columns. After the final run the furnace was allowed to cool at its own rate, with a continued flow of nitrogen.

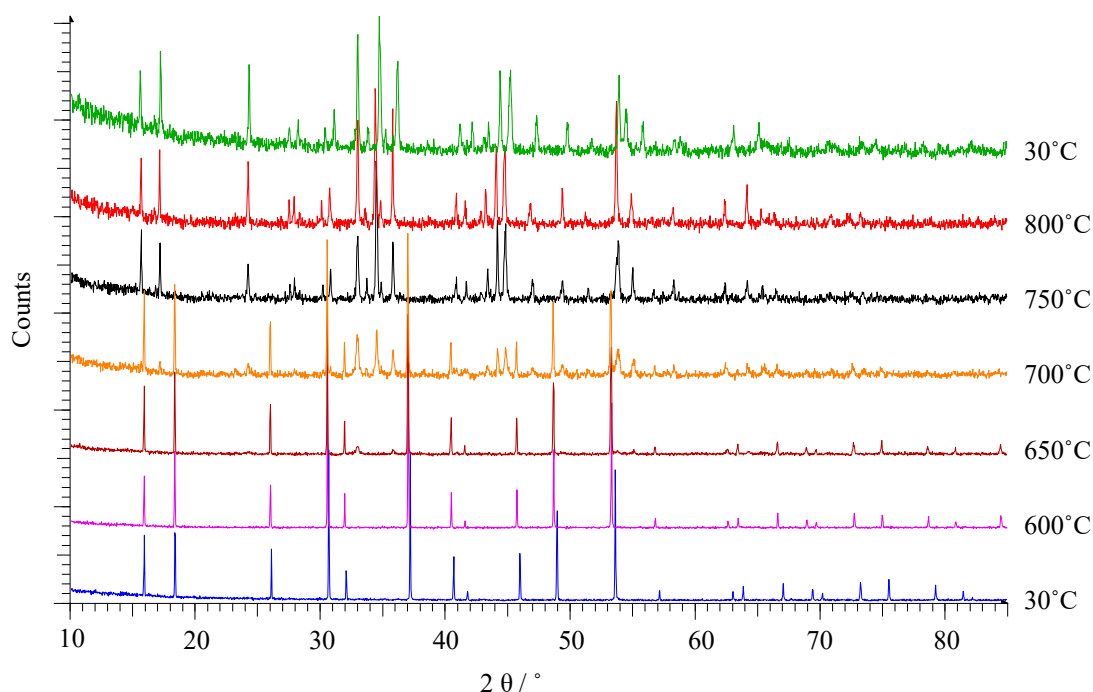


**Figure 21:** High temperature X-ray diffraction data for GeV<sub>4</sub>S<sub>8</sub>.

Contrary to data collected at low temperatures, no phase transition can be observed at elevated temperatures under the conditions utilised in these experiments. An expansion in the cubic unit cell, space group  $F\bar{4}3m$ , is seen from  $a = 9.65350(24)$  Å, at 30°C, to  $a = 9.723265(99)$  Å at 600°C. The diffraction data show that at temperatures above 700°C,  $C$ -GeV<sub>4</sub>S<sub>8</sub> is no longer present. The heat treatment of GeV<sub>4</sub>S<sub>8</sub>, up to 800°C under flowing N<sub>2</sub>, results in three binary phases; V<sub>2</sub>O<sub>3</sub>; V<sub>3</sub>S<sub>4</sub>; GeS<sub>2</sub>. V<sub>2</sub>O<sub>3</sub> is the first to be observed at 650°C. The thermodynamic stability of V<sub>2</sub>O<sub>3</sub> is likely to be the driving force

behind the decomposition observed when GeV<sub>4</sub>S<sub>8</sub> is heated in the presence of trace amounts of oxygen. The sample showed no impurity phase prior to heat treatment. This experiment demonstrated how crucial the exclusion of oxygen is to the synthesis of large, single phase GeV<sub>4</sub>S<sub>8</sub> samples.

### 3.4.3 Neutron studies of GeV<sub>4</sub>S<sub>8</sub>

Powder neutron diffraction data were collected on HRPD between  $7 \leq T / \text{K} \leq 300$ . Temperature sweeps were carried out from 7 K up to 34 K in 1K steps, from 34 K to 70 K in 2 K steps and from 70 K to 300 K in 10 K steps. Longer data collections were made at 7 K, 10 K, 13 K, 14 K, 15 K, 29 K and 32 K.

Structural refinements were initiated in the cubic space group  $F\bar{4}3m$  using atomic coordinates and lattice parameters previously determined[12]. The backgrounds were modelled using an expansion of the exponential function,

$$I_b = \sum_{j=1}^N B_j \frac{Q^{2(j-1)}}{(j-1)!}$$

**Equation (39)**

, designed to account for thermal diffuse scattering and the coefficients included as refinable parameters. The peak shape was described using a convolution of two back-to-back exponentials together with a pseudo-Voigt function to account for the Lorentzian broadening. Regions centred at  $d = 2.1\text{-}2.2$ ,  $1.5\text{-}1.6$  and  $1.2\text{-}1.3$  Å were excluded in the Rietveld analysis due to the presence of reflections originating from the vanadium sample can. Following initial refinement of scale factors, background terms, diffractometer constants, lattice and peak shape parameters, positional coordinates and thermal parameters were introduced. The thermal parameters were constrained below 33 K and for combined X-ray, neutron refinements at 300 K. Vanadium atomic positions were damped below 33 K. This resulted in residuals in the range of 2-7% depending on the counting time. Longer counting times, typically 100 μA, resulted in lower residuals.

Figure 22 shows the neutron diffraction profile of cubic  $\text{GeV}_4\text{S}_8$  ( $C\text{-GeV}_4\text{S}_8$ ) at 300 K. This structure persists under cooling from 300 K to 33 K. The final refined parameters are presented in Table 5.

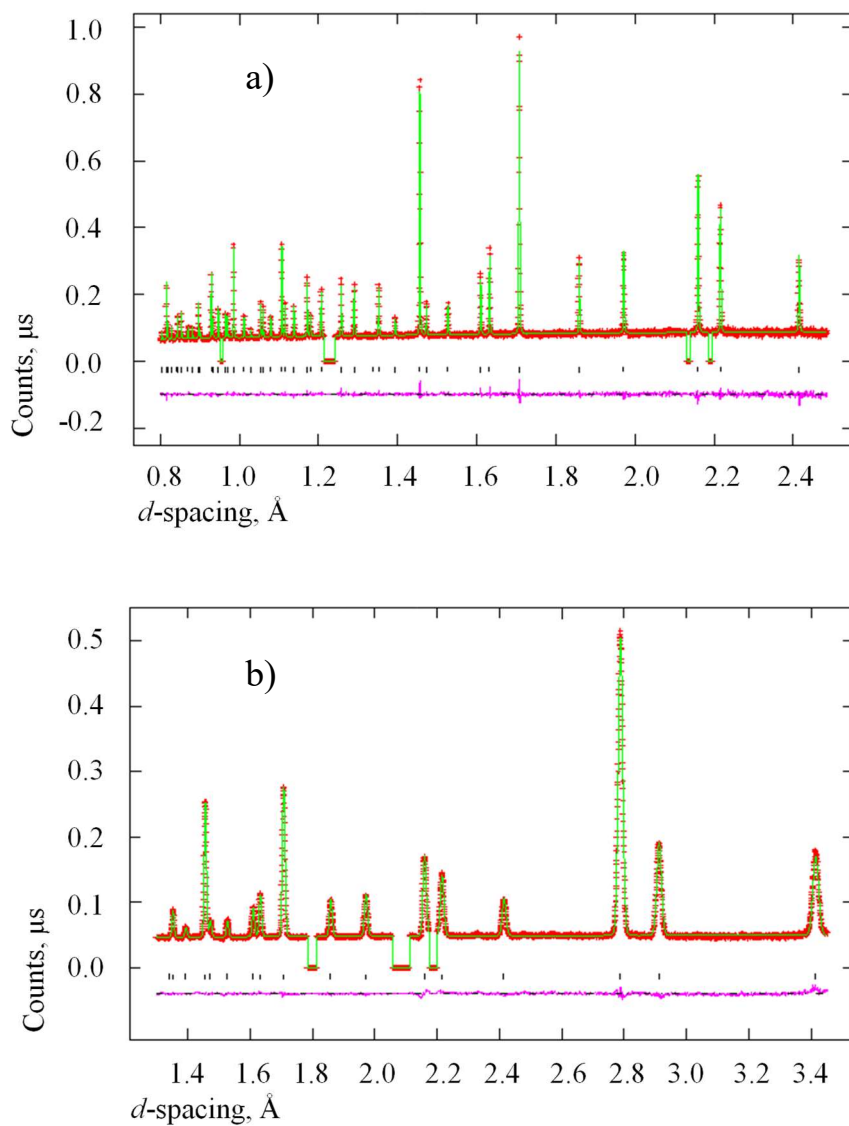


**Figure 22:** Final observed (crosses), calculated (upper full line) and difference (lower full line) neutron diffraction profile at 300 K of  $\text{GeV}_4\text{S}_8$ .

a) Backscattering bank,  $2\theta = 168.33^\circ$

b)  $90^\circ$  bank,  $2\theta = 89.58^\circ$ . Reflection positions are marked.

**Table 5:** Final refined parameters for GeV<sub>4</sub>S<sub>8</sub> in space group  $F\bar{4}3m$  at 300 K.

T / K		300
$a / \text{\AA}$		9.657105(10)
$V / \text{\AA}^3$		900.619(3)
Ge <sup>a</sup>	<i>site</i>	4( <i>a</i> )
	<i>x</i>	0
	$B / \text{\AA}^2$	0.1274(2)
V	<i>site</i> <sup>b</sup>	16( <i>e</i> )
	<i>x</i>	0.60652(13)
	$B / \text{\AA}^2$	0.1274(2)
S1	<i>site</i>	16( <i>e</i> )
	<i>x</i>	0.369661(29)
	$B / \text{\AA}^2$	0.1274(2)
S2	<i>site</i>	16( <i>e</i> )
	<i>x</i>	0.865195(28)
	$B / \text{\AA}^2$	0.1274(2)
$R_{wp} / \%$ (X-ray)		10.38
$R_{wp} / \%$ (neutron bs)		2.96
$R_{wp} / \%$ (neutron 90°)		2.22
$\chi^2$		6.053

A non-linear unit cell contraction is observed from  $a = 9.65710(1) \text{\AA}$  at 300 K to  $a = 9.64073(2) \text{\AA}$  at 33 K and is displayed in Figure 23. The thermal expansion coefficient,  $\alpha$ , is  $\alpha = 6.35033(2) \times 10^{-6} \text{ K}^{-1}$  at 33 K, comparable to that of glass.

---

<sup>a</sup> Ge fixed at origin  $x x x$

<sup>b</sup> 16(*e*) site is a special position at  $x x x$

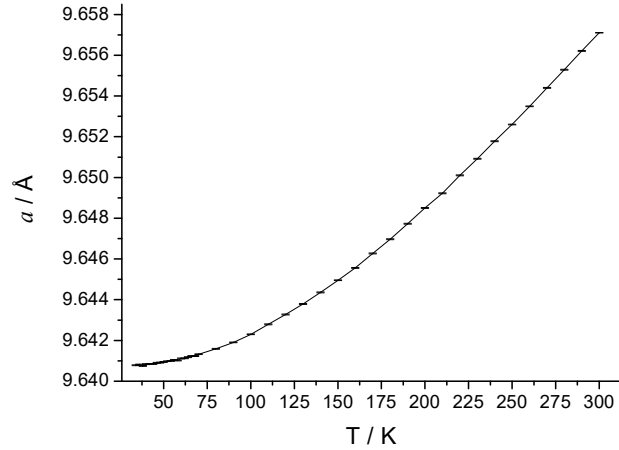


**Figure 23:** Temperature dependence of the unit cell in  $C\text{-GeV}_4\text{S}_8$ . Error bars are shown.

Data revealed that upon cooling to 7 K,  $\text{GeV}_4\text{S}_8$  exhibits a series of peak broadenings and a large range of splittings that become apparent below 33 K, i.e.  $T_S = 32$  K. It is the  $C\text{-GeV}_4\text{S}_8$   $[h00]$  reflections that undergo broadening and the remainder show clear splitting in the backscattering bank,  $2\theta = 168.33^\circ$ .

In order to determine what structural changes were taking place, two important regions within the data set were identified. Figure 24 displays the splitting of the  $C\text{-GeV}_4\text{S}_8$   $[622]$  and  $[533]$  reflections in the region  $1.445 \leq d / \text{\AA} \leq 1.48$  and Figure 25 shows the splitting of the  $C\text{-GeV}_4\text{S}_8$   $[440]$  reflection in the region  $1.69 \leq d / \text{\AA} \leq 1.72$ . These two regions were crucial in solving the data sets. Figure 24 and Figure 25 also show three distinct trends. There are clear differences in the number and intensity of the observed peaks over the d-spacing range shown. Throughout the temperature range,  $18 \leq T / \text{K} \leq 29$ , the intensities and splittings are very similar. For  $1.445 \leq d / \text{\AA} \leq 1.48$  the splittings are profoundly different at each temperature extreme.

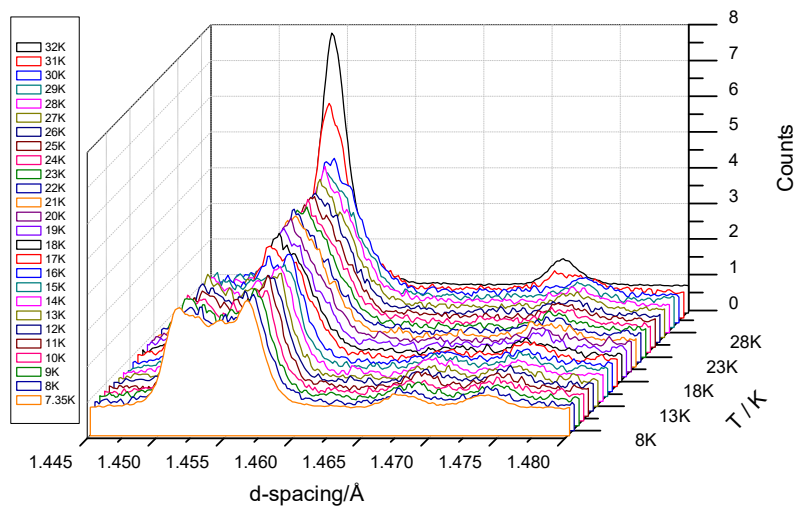


**Figure 24:** Splitting of the  $C\text{-GeV}_4\text{S}_8$  (622) reflection centred at  $d = 1.454 \text{ \AA}$  and the  $C\text{-GeV}_4\text{S}_8$  (533) reflection centred at  $d = 1.471 \text{ \AA}$  for  $7 \leq T / \text{K} \leq 32$ .

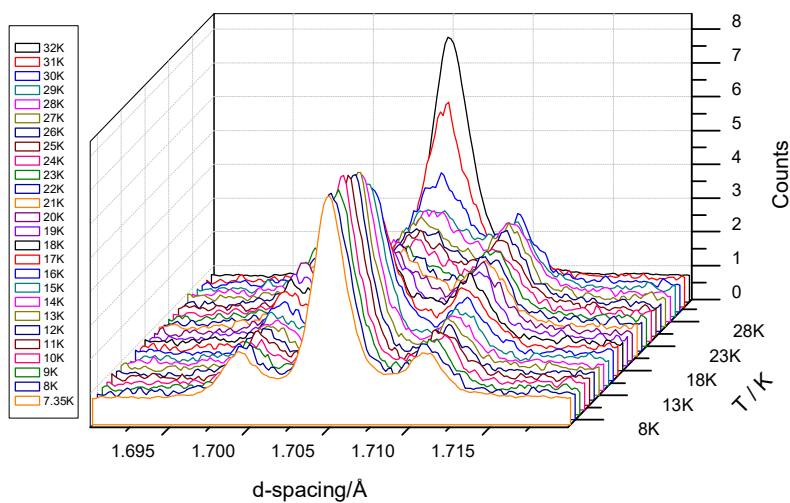


**Figure 25:** Splitting of the  $C\text{-GeV}_4\text{S}_8$  (440) reflection centred at  $d = 1.705 \text{ \AA}$  for  $7 \leq T / \text{K} \leq 32$ .

The subtle changes observed in these neutron diffraction data are gradual. This implies that the transition is likely to be of the second order (continuous). This has important implications, in terms of an appropriate space group, as polymorphs must have a symmetry relation. The low temperature polymorph

must belong to a sub-group of the high temperature phase. The specific heat capacity has previously been measured and two finite discontinuities are observed (Figure 26) to further support the notion of a second order phase transition.

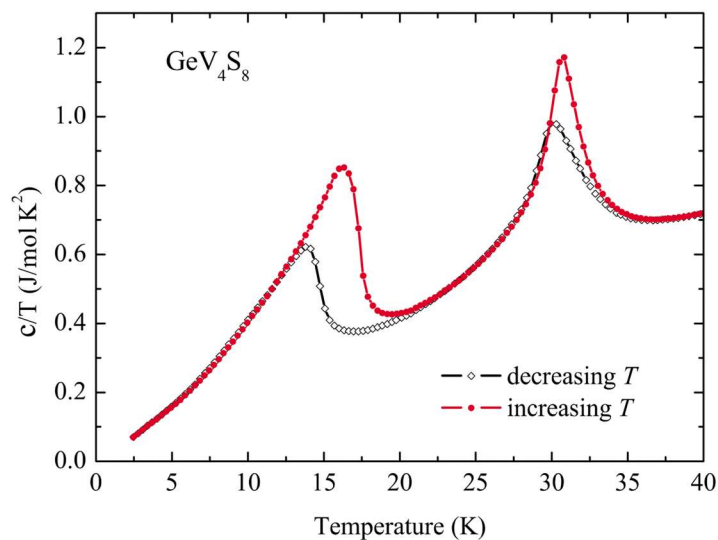


**Figure 26:** Specific heat capacity of  $\text{GeV}_4\text{S}_8$  [14].

At 32 K shoulders start to appear at the  $C\text{-GeV}_4\text{S}_8$  [440] reflection position. These can be fitted with a rhombohedral phase ( $R\text{-GeV}_4\text{S}_8$ ), space group  $R3m$ , that has been previously observed in  $\text{GeV}_4\text{S}_8$  by Chudo *et al.*[13], though no atomic coordinates were reported, and by a previous member of our group, A. D. McDowell[19]. A two phase Rietveld refinement, initially using the values reported in the thesis of A. D. McDowell for  $R\text{-GeV}_4\text{S}_8$ , resulted in residuals of 2.9 % and a reduced  $\chi^2$  of 2.667. It was found that a 3.27(1) % fraction of the overall composition was  $R\text{-GeV}_4\text{S}_8$  (Figure 30). This same two phase refinement was repeated at 31 K and 30 K, however it did not sufficiently describe the data. Figure 27 demonstrates the inability of the two phase model to account for the asymmetry and intensity distribution in the  $1.445 \leq d / \text{\AA} \leq 1.48$  and  $1.69 \leq d / \text{\AA} \leq 1.72$  regions respectively at 30 K.

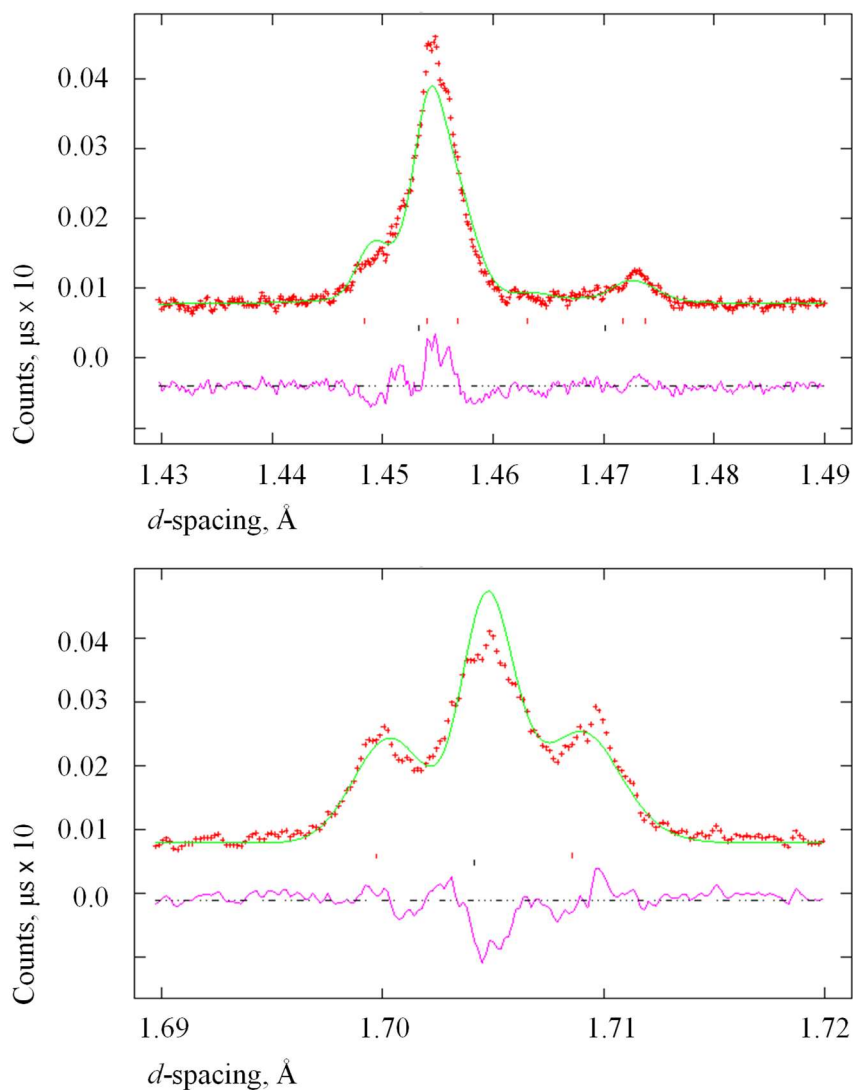


**Figure 27:** Observed (crosses), calculated (upper full line) and difference (lower full line) neutron diffraction profile at 30 K of  $\text{GeV}_4\text{S}_8$ . Backscattering bank,  $2\theta = 168.33^\circ$ . Reflection positions are marked, black denotes  $C\text{-GeV}_4\text{S}_8$ , red  $R\text{-GeV}_4\text{S}_8$ .

In previous investigations, two models have been proposed to describe  $\text{GeV}_4\text{S}_8$  at 25 K. Chudo *et al.* reported the presence of only the rhombohedral phase. Bichler *et al.*[14] proposed an orthorhombic structure and showed their data over the  $1.69 \leq d / \text{\AA} \leq 1.72$  region. These data had the same intensity distribution as is reported here. As a result of this observation, these models were investigated in order to help solve the data at 31 K and 30 K. According to the results presented here a phase transition to  $R\text{-GeV}_4\text{S}_8$  is never complete as this would result in only two peaks in the  $1.69 \leq d / \text{\AA} \leq 1.72$  region, not three as is observed. Bichler *et al.* correctly discounted the possibility of a purely rhombohedral phase but failed to provide a precise description of



GeV<sub>4</sub>S<sub>8</sub> at 25 K. They proposed that the cubic structure transforms directly to an orthorhombic structure (*O*-GeV<sub>4</sub>S<sub>8</sub>), space group *Imm*2, at T<sub>S</sub> = 30 K. No evidence was found of this. Figure 28 demonstrates the inability of the orthorhombic model to effectively describe the observed profile at 25 K.

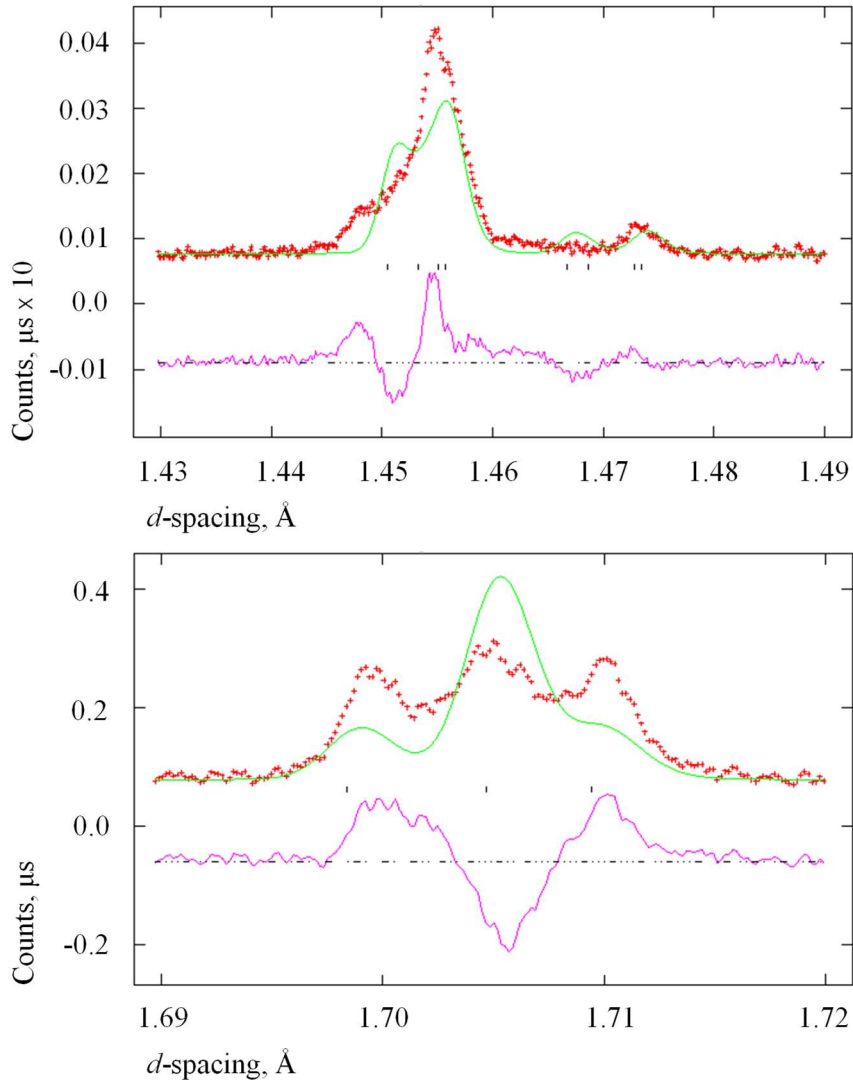


**Figure 28:** Observed (crosses), calculated (upper full line) and difference (lower full line) neutron diffraction profile at 25 K of *O*-GeV<sub>4</sub>S<sub>8</sub>. Backscattering bank,  $2\theta = 168.33^\circ$ . Reflection positions are marked

After the unsuccessful attempts to characterise data using previously known models, careful analysis of the splitting pattern arising from the *C*-GeV<sub>4</sub>S<sub>8</sub> [440] reflection was carried out at 7 K. An intensity distribution of 1:4:1 centred at  $d = 1.705 \text{ \AA}$  was observed in the profile to establish that the structure was *C*-centred monoclinic. The monoclinic axis was then expressed in terms of the cubic axis and the scalar products taken to determine the monoclinic lattice parameters including  $\beta$ . A matrix form (Figure 29) of the

cubic axis was then used to calculate the monoclinic coordinates by transposition.

$$\begin{bmatrix} 1/2 & 1/2 & 1 \\ 1/2 & -1/2 & 0 \\ 1/2 & 1/2 & 0 \end{bmatrix}$$

**Figure 29:** Matrix form of the cubic axis.

A trial model was established in *Cm* (*M*-GeV<sub>4</sub>S<sub>8</sub>) which is a sub-group of *R3m*. A Rietveld refinement using this model resulted in residuals of 2.8 % and a reduced  $\chi^2$  of 2.701. The monoclinic model can be used to fit the data from 7 K (Figure 39) to 15 K (Figure 38). At 16 K intensity mismatches start to appear in the  $1.445 \leq d / \text{\AA} \leq 1.48$  region.

To find an adequate description for the region,  $16 \leq T / \text{K} \leq 31$ , it was necessary to use the 29 K data set (the only longer data collection, 100  $\mu\text{A}$ , within the unsolved range). Analysis was initiated in GSAS using the two phase experiment file utilised at 32 K with the inclusion of the monoclinic phase observed at 7 K. These three-phase refinements with the cubic, rhombohedral and monoclinic phases were found to satisfactorily model the observed data in the  $16 \leq T / \text{K} \leq 31$  range. The Rietveld refinements carried out with all three phases were complex. It was necessary to constrain the thermal parameters of all three phases to be equal below 31 K. The monoclinic and the rhombohedral phases were also constrained to be equal to each other. The phase fractions were adjusted manually before being introduced as a refinable parameter.

The final observed, calculated and difference profiles for selected temperatures below 33 K are shown in Figure 30 through to Figure 39; the final refined parameters are displayed in Table 6 through to Table 14; and selected bond lengths plus bond angles in Table 15, 16 and 17.

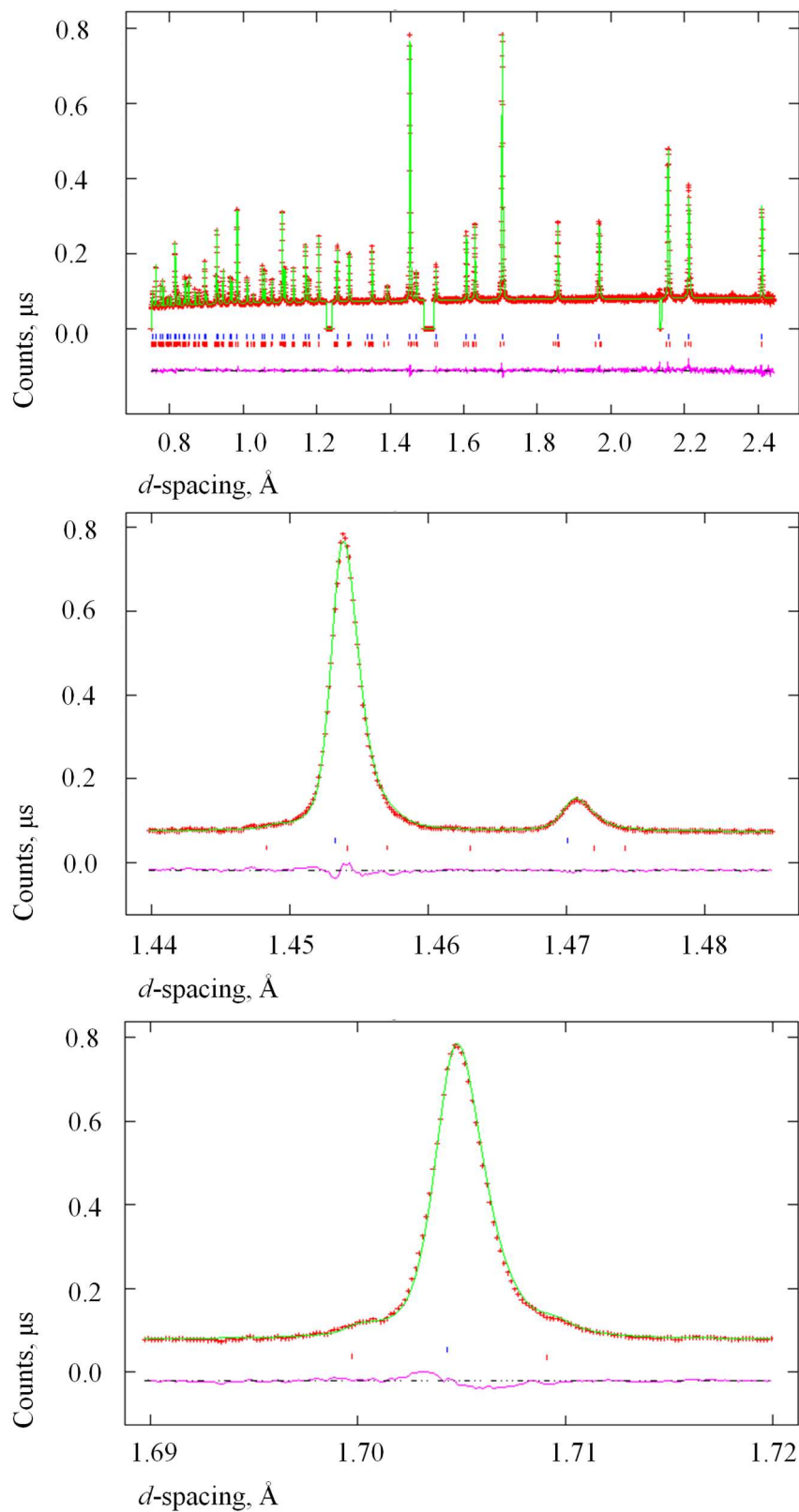


**Figure 30:** Final observed (crosses), calculated (upper full line) and difference (lower full line) neutron diffraction profile at 32 K of  $\text{GeV}_4\text{S}_8$ . Backscattering bank,  $2\theta = 168.33^\circ$ . Reflection positions are marked; blue denotes  $C\text{-GeV}_4\text{S}_8$ , red  $R\text{-GeV}_4\text{S}_8$ .

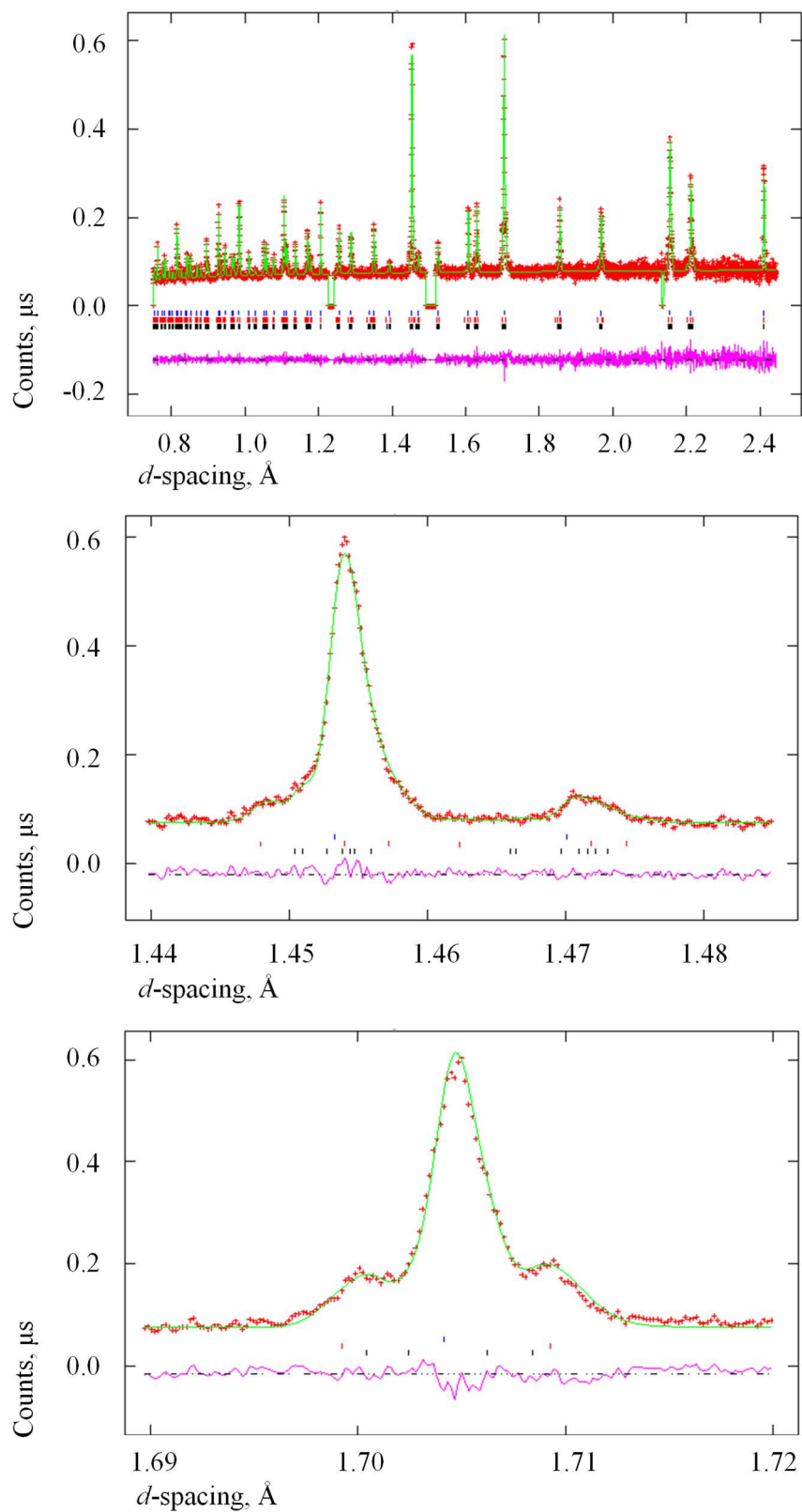


**Figure 31:** Final observed (crosses), calculated (upper full line) and difference (lower full line) neutron diffraction profile at 31 K of  $\text{GeV}_4\text{S}_8$ . Backscattering bank,  $2\theta = 168.33^\circ$ . Reflection positions are marked; blue denotes  $C$ - $\text{GeV}_4\text{S}_8$ , red  $R$ - $\text{GeV}_4\text{S}_8$  and black  $M$ - $\text{GeV}_4\text{S}_8$ .

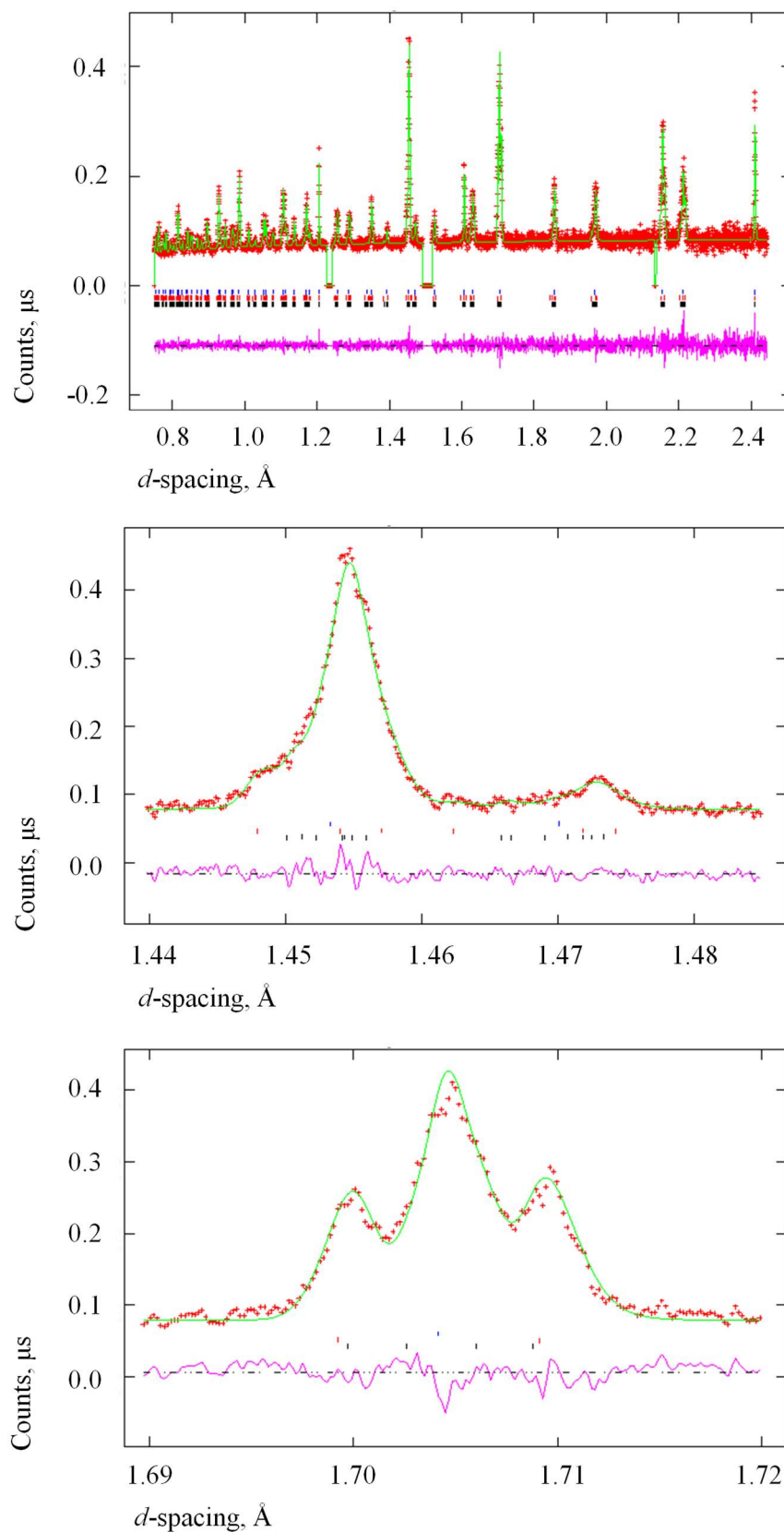


**Figure 32:** Final observed (crosses), calculated (upper full line) and difference (lower full line) neutron diffraction profile at 30 K of GeV<sub>4</sub>S<sub>8</sub>. Backscattering bank,  $2\theta = 168.33^\circ$ . Reflection positions are marked; blue denotes C-GeV<sub>4</sub>S<sub>8</sub>, red R-GeV<sub>4</sub>S<sub>8</sub> and black M-GeV<sub>4</sub>S<sub>8</sub>.

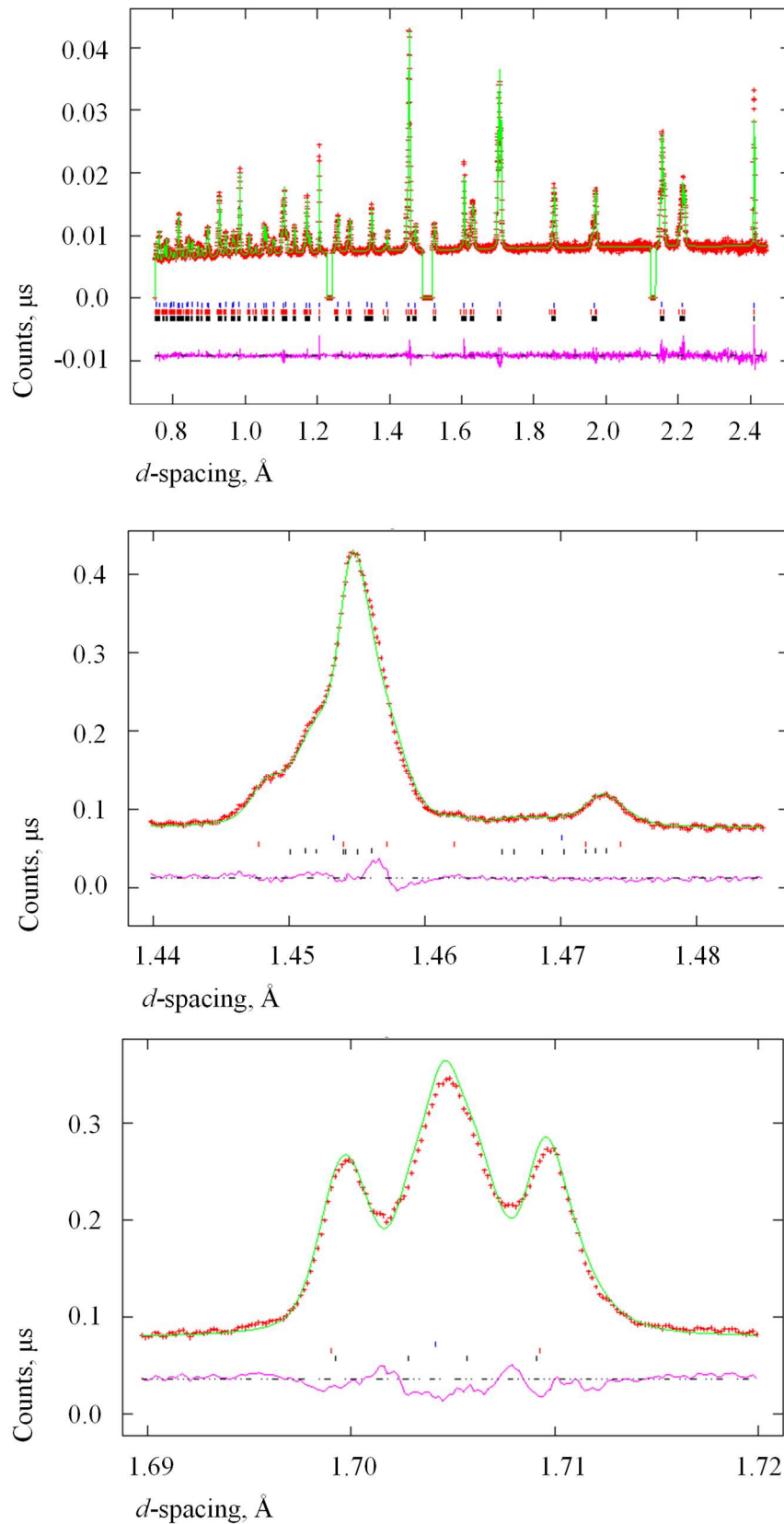


**Figure 33:** Final observed (crosses), calculated (upper full line) and difference (lower full line) neutron diffraction profile at 29 K of  $\text{GeV}_4\text{S}_8$ . Backscattering bank,  $2\theta = 168.33^\circ$ . Reflection positions are marked; blue denotes  $C$ - $\text{GeV}_4\text{S}_8$ , red  $R$ - $\text{GeV}_4\text{S}_8$  and black  $M$ - $\text{GeV}_4\text{S}_8$ .

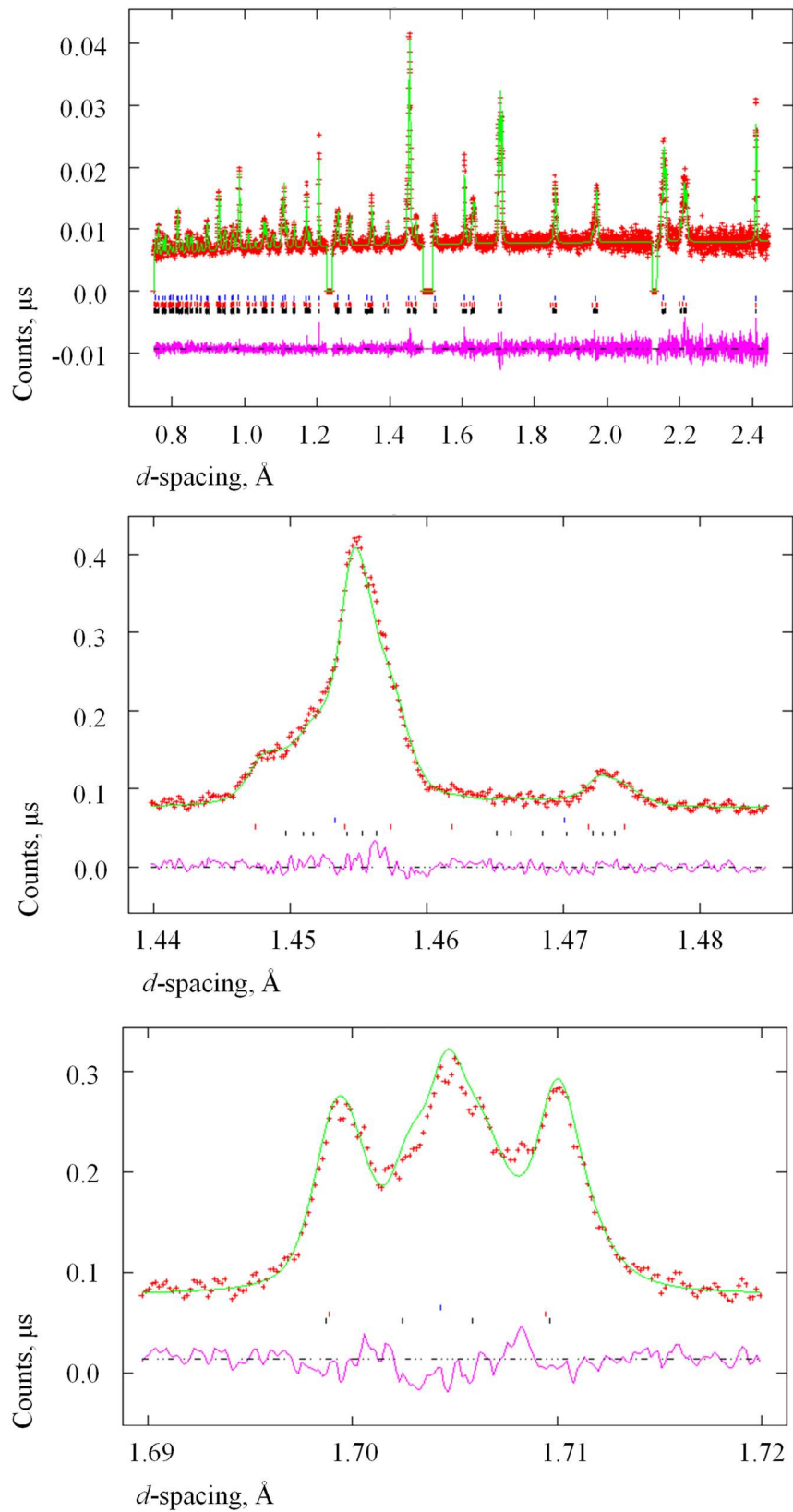


**Figure 34:** Final observed (crosses), calculated (upper full line) and difference (lower full line) neutron diffraction profile at 25 K of  $\text{GeV}_4\text{S}_8$ . Backscattering bank,  $2\theta = 168.33^\circ$ . Reflection positions are marked; blue denotes  $C$ - $\text{GeV}_4\text{S}_8$ , red  $R$ - $\text{GeV}_4\text{S}_8$  and black  $M$ - $\text{GeV}_4\text{S}_8$ .

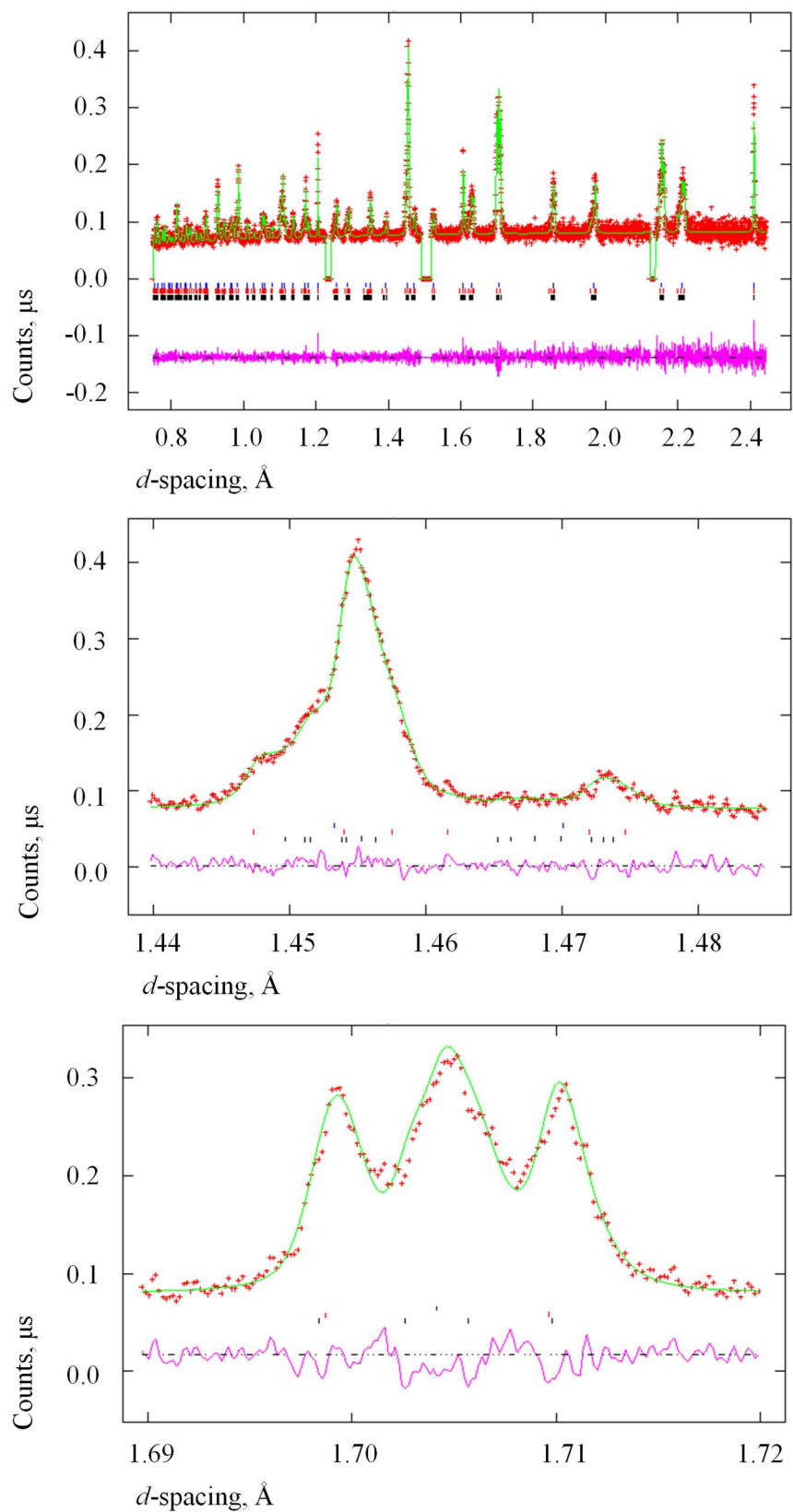


**Figure 35:** Final observed (crosses), calculated (upper full line) and difference (lower full line) neutron diffraction profile at 20 K of  $\text{GeV}_4\text{S}_8$ . Backscattering bank,  $2\theta = 168.33^\circ$ . Reflection positions are marked; blue denotes  $C\text{-GeV}_4\text{S}_8$ , red  $R\text{-GeV}_4\text{S}_8$  and black  $M\text{-GeV}_4\text{S}_8$ .



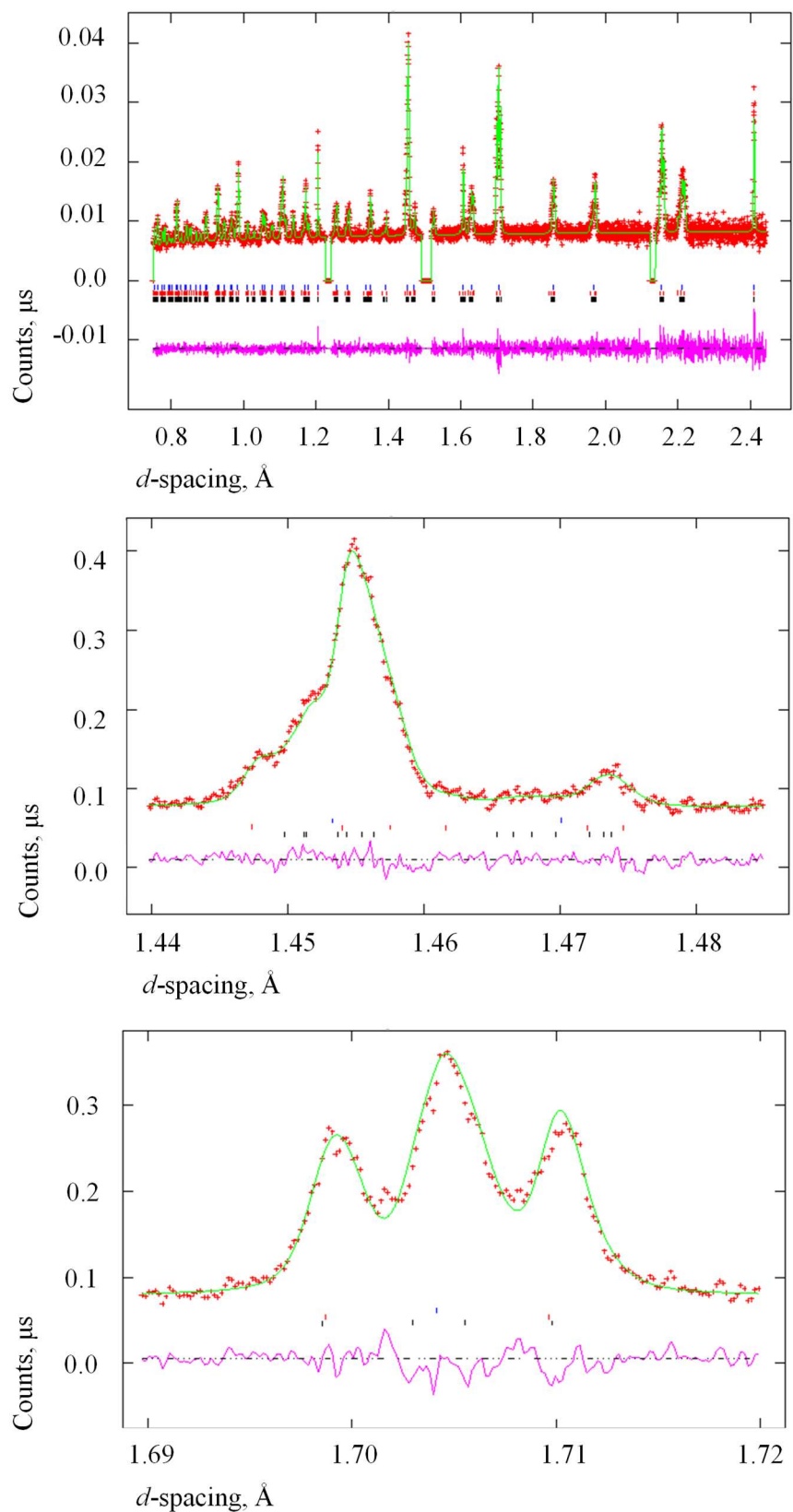


**Figure 36:** Final observed (crosses), calculated (upper full line) and difference (lower full line) neutron diffraction profile at 19 K of  $\text{GeV}_4\text{S}_8$ . Backscattering bank,  $2\theta = 168.33^\circ$ . Reflection positions are marked; blue denotes  $C$ - $\text{GeV}_4\text{S}_8$ , red  $R$ - $\text{GeV}_4\text{S}_8$  and black  $M$ - $\text{GeV}_4\text{S}_8$ .

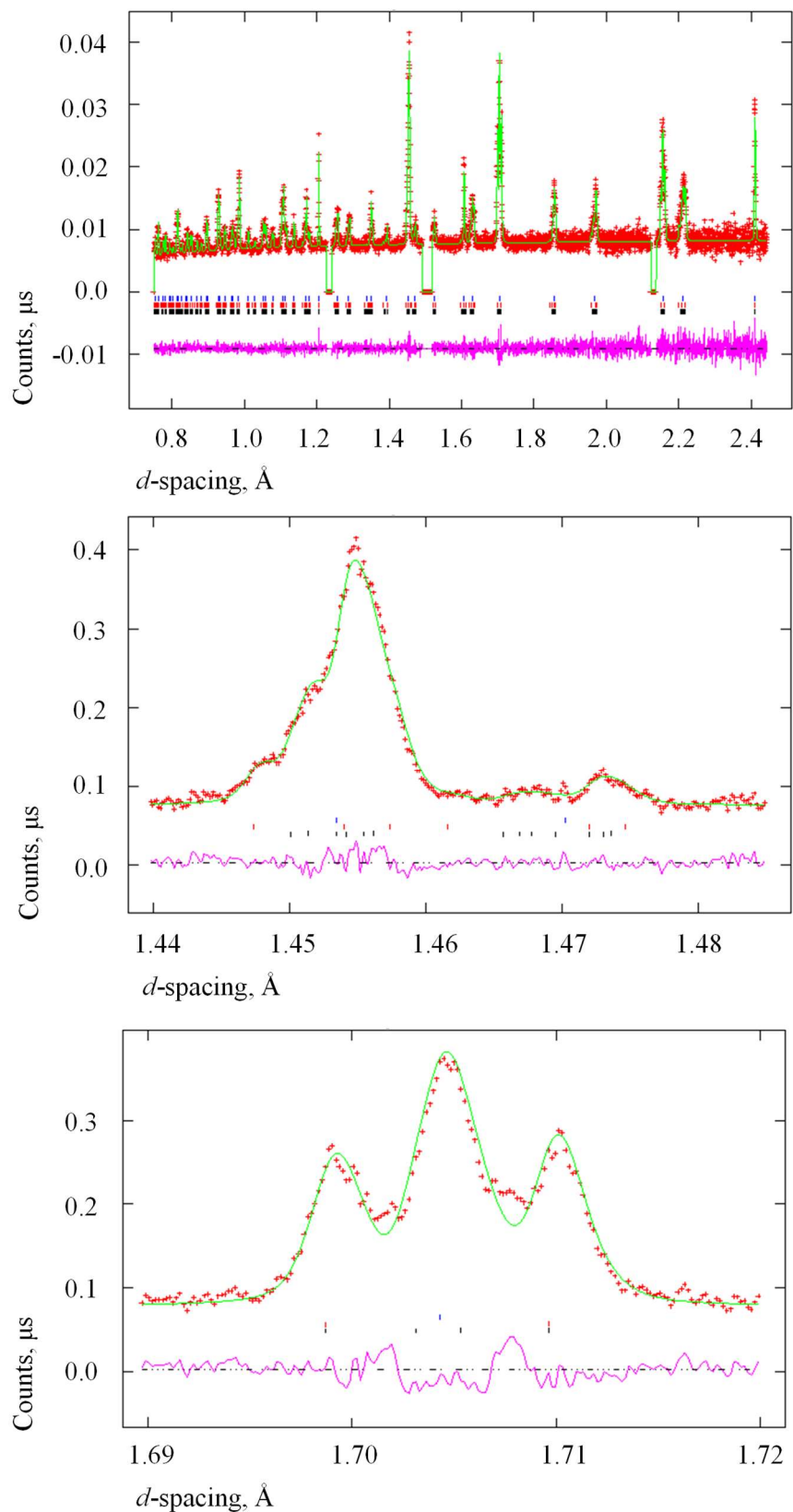


**Figure 37:** Final observed (crosses), calculated (upper full line) and difference (lower full line) neutron diffraction profile at 18 K of  $\text{GeV}_4\text{S}_8$ . Backscattering bank,  $2\theta = 168.33^\circ$ . Reflection positions are marked; blue denotes  $C$ - $\text{GeV}_4\text{S}_8$ , red  $R$ - $\text{GeV}_4\text{S}_8$  and black  $M$ - $\text{GeV}_4\text{S}_8$ .

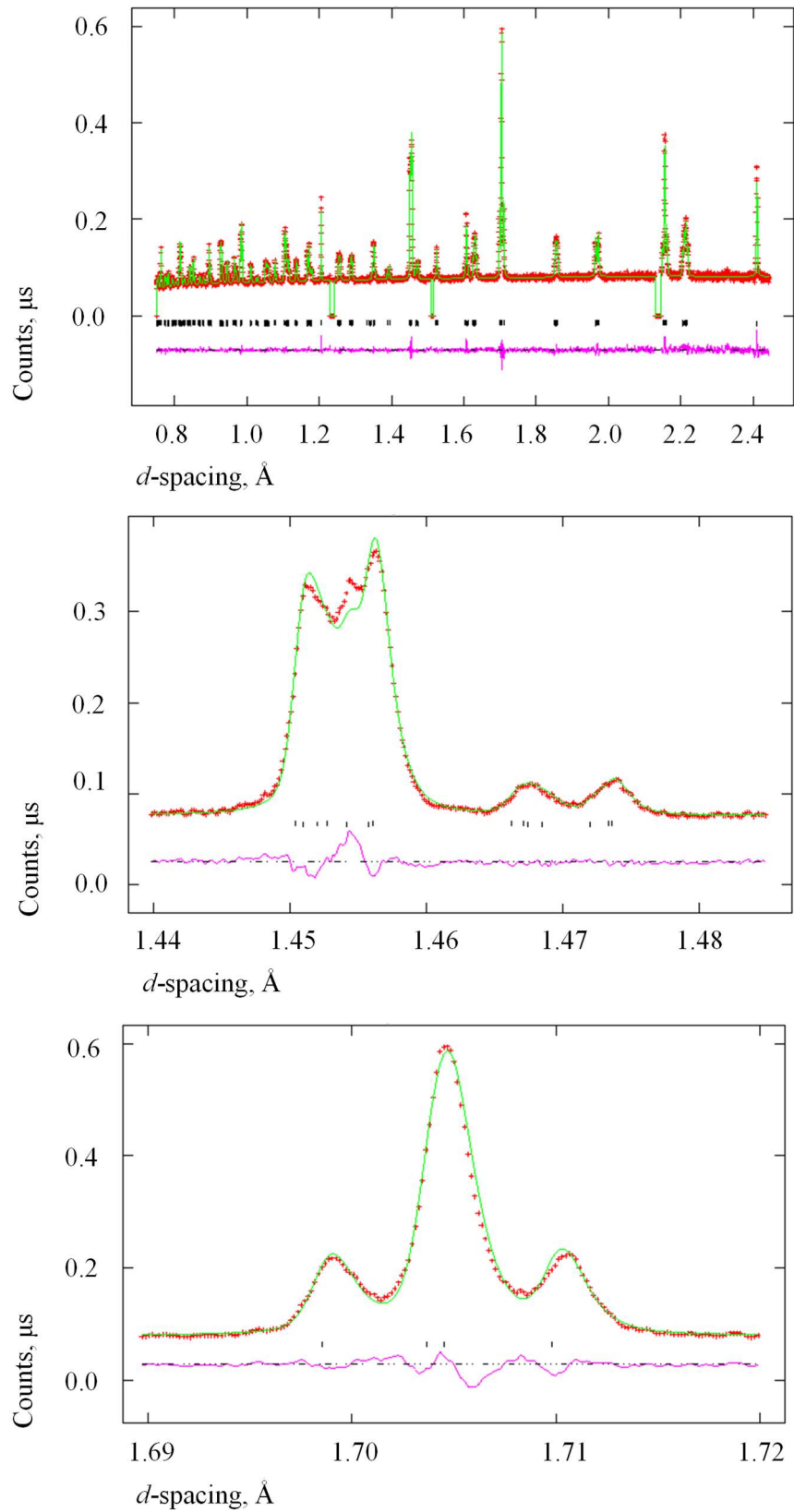


**Figure 38:** Final observed (crosses), calculated (upper full line) and difference (lower full line) neutron diffraction profile at 15 K of  $M\text{-GeV}_4\text{S}_8$ . Backscattering bank,  $2\theta = 168.33^\circ$ . Reflection positions are marked.

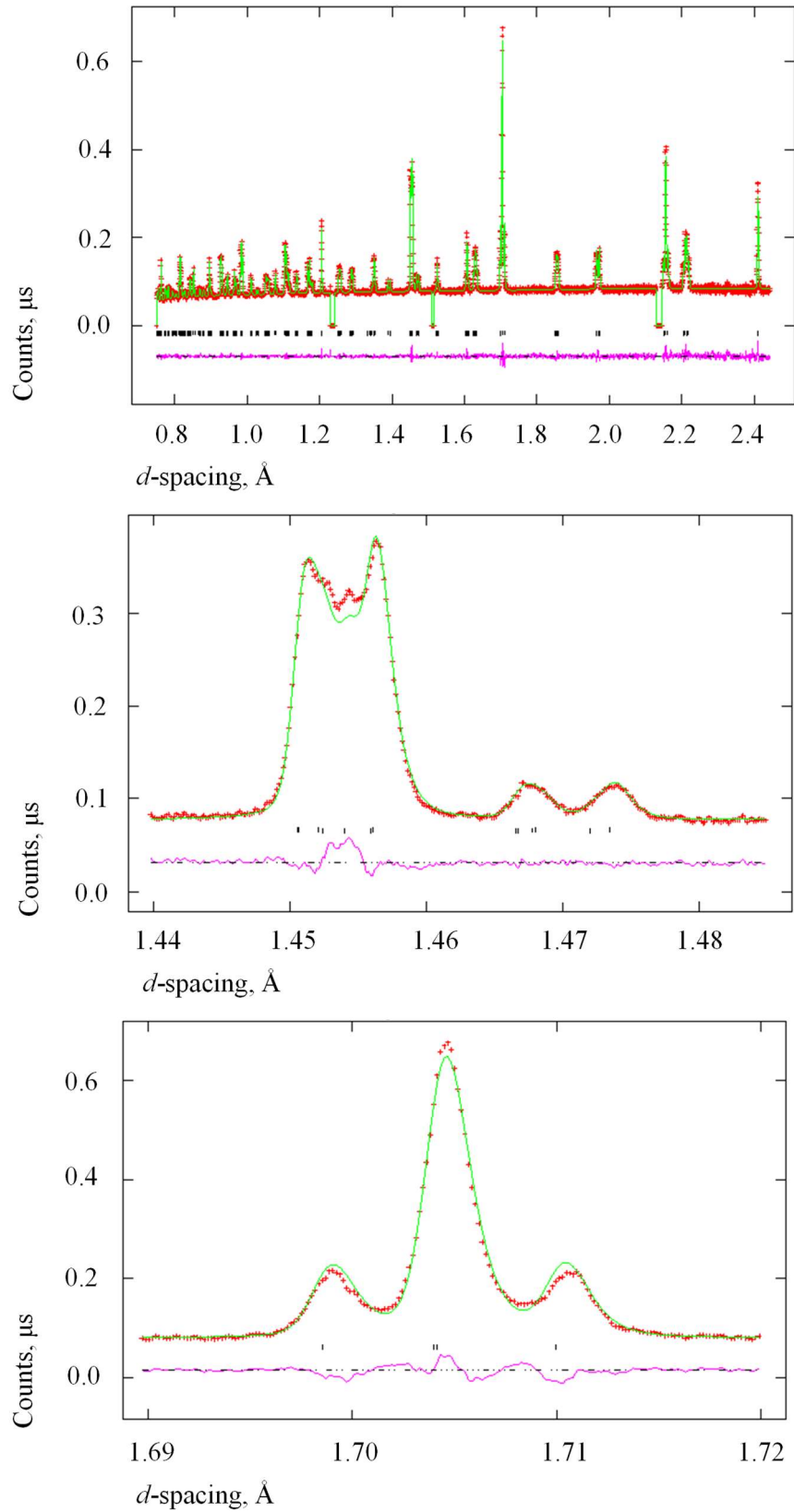


**Figure 39:** Final observed (crosses), calculated (upper full line) and difference (lower full line) neutron diffraction profile at 7 K of  $M\text{-GeV}_4\text{S}_8$ . Backscattering bank,  $2\theta = 168.33^\circ$ . Reflection positions are marked.

**Table 6:** Final refined parameters for GeV<sub>4</sub>S<sub>8</sub> at 32 K.

<i>R</i> -GeV <sub>4</sub> S <sub>8</sub> ( <i>R3m</i> )			<i>C</i> -GeV <sub>4</sub> S <sub>8</sub> ( <i>F4̄3m</i> )		
Weight Fraction / %	3.27(1)		Weight Fraction / %	96.73(5)	
<i>a</i> / Å	6.799208(175)		<i>a</i> / Å	9.640805(10)	
<i>α</i> / °	60.363(2)		<i>V</i> / Å <sup>3</sup>	896.066(3)	
<i>V</i> / Å <sup>3</sup>	224.082(9)		<i>B</i> / Å <sup>2</sup>	0.5953(2)	
<i>B</i> / Å <sup>2</sup>	0.2858(-)		Ge <sup>a</sup>	<i>site</i>	1( <i>a</i> )
	<i>x</i>	0	Ge <sup>a</sup>	<i>x</i>	0
V1	<i>site</i> <sup>b</sup>	1( <i>a</i> )	V	<i>site</i>	16( <i>e</i> )
	<i>x</i>	0.3925(-)	V	<i>x</i>	0.60544(20)
V2	<i>site</i> <sup>c</sup>	3( <i>b</i> )	S1	<i>site</i>	16( <i>e</i> )
	<i>x</i>	0.4070(-)	S1	<i>x</i>	0.369697(44)
	<i>z</i>	0.8179(-)	S2	<i>site</i>	16( <i>e</i> )
S2	<i>site</i>	3( <i>b</i> )	S2	<i>x</i>	0.865015 (37)
	<i>x</i>	0.6322(23)			
	<i>z</i>	0.1096(37)			
S3	<i>site</i>	1( <i>a</i> )			
	<i>x</i>	0.1346(22)			
S4	<i>site</i>	3( <i>b</i> )			
	<i>x</i>	0.1464(22)			
	<i>z</i>	0.6169(35)			
	R <sub>wp</sub> / %				2.77
	χ <sup>2</sup>				2.431

<sup>a</sup> Ge fixed at origin *x x x*<sup>b</sup> 1(*a*) and 16(*e*) sites are special positions at *x x x*<sup>c</sup> 3(*b*) site is a special position at *x 0 z*

**Table 7:** Final refined parameters for GeV<sub>4</sub>S<sub>8</sub> at 31 K.

<b><i>M</i>-GeV<sub>4</sub>S<sub>8</sub> (<i>Cm</i>)</b>			<b><i>R</i>-GeV<sub>4</sub>S<sub>8</sub> (<i>R3m</i>)</b>			<b><i>C</i>-GeV<sub>4</sub>S<sub>8</sub> (<i>F43m</i>)</b>		
Weight Fraction / %		19(1)	Weight Fraction / %		22(1)	Weight Fraction / %		59(1)
<i>a</i> / Å		11.7807(5)	<i>a</i> / Å		6.79727(16)	<i>a</i> / Å		9.64052(4)
<i>b</i> / Å		6.83359(30)						
<i>c</i> / Å		6.80174(28)						
$\beta$ / °		125.087(3)	$\alpha$ / °		60.385(2)			
V / Å <sup>3</sup>		448.070(14)	V / Å <sup>3</sup>		224.005(5)	V / Å <sup>3</sup>		895.985(11)
<i>B</i> / Å <sup>2</sup>		0.2811(6)	<i>B</i> / Å <sup>2</sup>		0.2811(6)	<i>B</i> / Å <sup>2</sup>		0.7856(6)
Ge <sup>a</sup>	<i>site</i>	2( <i>a</i> )	Ge <sup>a</sup>	<i>site</i>	1( <i>a</i> )	Ge <sup>a</sup>	<i>site</i>	4( <i>a</i> )
	<i>x</i>	0		<i>x</i>	0		<i>x</i>	0
V1	<i>site</i> <sup>b</sup>	2( <i>a</i> )	V1	<i>site</i> <sup>c</sup>	1( <i>a</i> )	V	<i>site</i> <sup>c</sup>	16( <i>e</i> )
	<i>x</i>	0.598(25)		<i>x</i>	0.3913(60)		<i>x</i>	0.6101(12)
	<i>z</i>	0.367(47)	V2	<i>site</i> <sup>b</sup>	3( <i>b</i> )	S1	<i>site</i>	16( <i>e</i> )
<i>site</i>	2( <i>a</i> )	<i>x</i>		0.4052(78)	<i>x</i>		0.36965(25)	
<i>x</i>	0.571(21)	<i>y</i>		0.819(12)	S2	<i>site</i>	16( <i>e</i> )	
<i>z</i>	0.769(32)	S1	<i>site</i>	1( <i>a</i> )		<i>x</i>	0.86494(22)	
V3	<i>site</i>		4( <i>b</i> )	S1	<i>x</i>	0.6291(12)		
	<i>x</i>	0.385(20)	S2		<i>site</i>	3( <i>b</i> )		
	<i>y</i>	0.195(20)		<i>x</i>	0.6311(14)			
	<i>z</i>	0.381(33)	<i>z</i>	0.1126(23)				
S1	<i>site</i>	2( <i>a</i> )	S3	<i>site</i>	1( <i>a</i> )			
	<i>x</i>	0.3683(45)		<i>x</i>	0.1350(11)			
	<i>z</i>	0.6335(89)	S4	<i>site</i>	3( <i>b</i> )			
S2	<i>site</i>	2( <i>a</i> )		<i>x</i>	0.1400(12)			
	<i>x</i>	0.3721(41)	<i>z</i>	0.5942(19)				
	<i>z</i>	0.1072(72)						
S3	<i>site</i>	4( <i>b</i> )						
	<i>x</i>	0.6306(30)						
	<i>y</i>	0.7339(36)						
	<i>z</i>	0.6386(48)						
S4	<i>site</i>	2( <i>a</i> )						
	<i>x</i>	0.8620(37)						
	<i>z</i>	0.1138(75)						
S5	<i>site</i>	2( <i>a</i> )						
	<i>x</i>	0.8574(41)						
	<i>z</i>	0.5900(65)						
S6	<i>site</i>	4( <i>b</i> )						
	<i>x</i>	0.1290(31)						
	<i>y</i>	0.7390(37)						
	<i>z</i>	0.1083(52)						
R <sub>wp</sub> / %					6.46			
$\chi^2$					13.21			

<sup>a</sup> Ge fixed at origin *x x x*<sup>b</sup> 2(*a*) and 3(*b*) sites are special positions at *x 0 z*<sup>c</sup> 1(*a*) and 16(*e*) are special positions at *x x x*

**Table 8:** Final refined parameters for GeV<sub>4</sub>S<sub>8</sub> at 30 K.

<i>M</i> -GeV <sub>4</sub> S <sub>8</sub> ( <i>Cm</i> )			<i>R</i> -GeV <sub>4</sub> S <sub>8</sub> ( <i>R3m</i> )			<i>C</i> -GeV <sub>4</sub> S <sub>8</sub> ( <i>F43m</i> )		
Weight Fraction / %	31(1)		Weight Fraction / %	35(1)		Weight Fraction / %	34(1)	
<i>a</i> / Å	11.7822(3)		<i>a</i> / Å	6.79692(11)		<i>a</i> / Å	9.64048(10)	
<i>b</i> / Å	6.83508(21)							
<i>c</i> / Å	6.79869(21)							
$\beta$ / °	125.080(2)		$\alpha$ / °	60.387(1)				
V / Å <sup>3</sup>	448.060(11)		V / Å <sup>3</sup>	223.979(3)		V / Å <sup>3</sup>	895.974(28)	
<i>B</i> / Å <sup>2</sup>	0.3016(6)		<i>B</i> / Å <sup>2</sup>	0.3016(6)		<i>B</i> / Å <sup>2</sup>	1.540(1)	
Ge <sup>a</sup>	<i>site</i>	2( <i>a</i> )	Ge <sup>a</sup>	<i>site</i>	1( <i>a</i> )	Ge <sup>a</sup>	<i>site</i>	4( <i>a</i> )
	<i>x</i>	0		<i>x</i>	0		<i>x</i>	0
V1	<i>site</i> <sup>b</sup>	2( <i>a</i> )	V1	<i>site</i> <sup>c</sup>	1( <i>a</i> )	V	<i>site</i> <sup>c</sup>	16( <i>e</i> )
	<i>x</i>	0.605(15)		<i>x</i>	0.4060(41)		<i>x</i>	0.6107(38)
	<i>z</i>	0.356(28)	V2	<i>site</i> <sup>b</sup>	3( <i>b</i> )	S1	<i>site</i>	16( <i>e</i> )
V2	<i>site</i>	2( <i>a</i> )		<i>x</i>	0.3980(48)		<i>x</i>	0.37027(63)
	<i>x</i>	0.613(18)		<i>y</i>	0.8207(72)	S2	<i>site</i>	16( <i>e</i> )
	<i>z</i>	0.835(25)	S1	<i>site</i>	1( <i>a</i> )		<i>x</i>	0.86421(57)
V3	<i>site</i>	4( <i>b</i> )		S2	<i>x</i>	0.63196(86)		
	<i>x</i>	0.388(10)	<i>site</i>		3( <i>b</i> )			
	<i>y</i>	0.190(12)	S3	<i>x</i>	0.63107(91)			
	<i>z</i>	0.375(17)		<i>z</i>	0.1106(16)			
S1	<i>site</i>	2( <i>a</i> )	S4	<i>site</i>	1( <i>a</i> )			
	<i>x</i>	0.3736(28)		<i>x</i>	0.13658(72)			
	<i>z</i>	0.6350(56)	S4	<i>site</i>	3( <i>b</i> )			
S2	<i>site</i>	2( <i>a</i> )		<i>x</i>	0.13996(85)			
	<i>x</i>	0.3631(28)	<i>z</i>	0.5990(15)				
	<i>z</i>	0.1241(47)						
S3	<i>site</i>	4( <i>b</i> )						
	<i>x</i>	0.6332(18)						
	<i>y</i>	0.7331(25)						
	<i>z</i>	0.6371(32)						
S4	<i>site</i>	2( <i>a</i> )						
	<i>x</i>	0.8645(25)						
	<i>z</i>	0.1318(54)						
S5	<i>site</i>	2( <i>a</i> )						
	<i>x</i>	0.8644(29)						
	<i>z</i>	0.5925(42)						
S6	<i>site</i>	4( <i>b</i> )						
	<i>x</i>	0.1288(19)						
	<i>y</i>	0.7312(26)						
	<i>z</i>	0.1154(30)						
R <sub>wp</sub> / %					6.50			
$\chi^2$					13.72			

<sup>a</sup> Ge fixed at origin *x x x*<sup>b</sup> 2(*a*) and 3(*b*) sites are special positions at *x 0 z*<sup>c</sup> 1(*a*) and 16(*e*) are special positions at *x x x*

**Table 9:** Final refined parameters for GeV<sub>4</sub>S<sub>8</sub> at 29 K.

<i>M</i> -GeV <sub>4</sub> S <sub>8</sub> ( <i>Cm</i> )			<i>R</i> -GeV <sub>4</sub> S <sub>8</sub> ( <i>R3m</i> )			<i>C</i> -GeV <sub>4</sub> S <sub>8</sub> ( <i>F43m</i> )		
Weight Fraction / %		43.4(6)	Weight Fraction / %		35.6(5)	Weight Fraction / %		21.0(6)
<i>a</i> / Å		11.7825(1)	<i>a</i> / Å		6.79669(4)	<i>a</i> / Å		9.64050(8)
<i>b</i> / Å		6.83617(7)						
<i>c</i> / Å		6.79721(12)						
$\beta$ / °		125.088(1)	$\alpha$ / °		60.395(1)			
V / Å <sup>3</sup>		448.001(6)	V / Å <sup>3</sup>		223.997(1)	V / Å <sup>3</sup>		895.982(21)
<i>B</i> / Å <sup>2</sup>		0.3679(3)	<i>B</i> / Å <sup>2</sup>		0.3679(3)	<i>B</i> / Å <sup>2</sup>		2.637(1)
Ge <sup>a</sup>	<i>site</i>	2( <i>a</i> )	Ge <sup>a</sup>	<i>site</i>	1( <i>a</i> )	Ge <sup>a</sup>	<i>site</i>	4( <i>a</i> )
	<i>x</i>	0		<i>x</i>	0		<i>x</i>	0
V1	<i>site</i> <sup>b</sup>	2( <i>a</i> )	V1	<i>site</i> <sup>c</sup>	1( <i>a</i> )	V	<i>site</i> <sup>c</sup>	16( <i>e</i> )
	<i>x</i>	0.6086(68)		<i>x</i>	0.4088(20)		<i>x</i>	0.6107(40)
	<i>z</i>	0.3868(152)	V2	<i>site</i> <sup>b</sup>	3( <i>b</i> )	S1	<i>site</i>	16( <i>e</i> )
V2	<i>site</i>	2( <i>a</i> )		<i>x</i>	0.3943(25)		<i>x</i>	0.37110(68)
	<i>x</i>	0.6066(76)		<i>y</i>	0.8126(42)	S2	<i>site</i>	16( <i>e</i> )
<i>z</i>	0.8255(102)	S1	<i>site</i>	1( <i>a</i> )	<i>x</i>		0.86370(59)	
V3	<i>site</i>		4( <i>b</i> )	S2	<i>x</i>	0.63291(44)		
	<i>x</i>	0.3860(35)	<i>site</i>		3( <i>b</i> )			
	<i>y</i>	0.2019(46)	S3	<i>x</i>	0.63371(47)			
	<i>z</i>	0.3819(93)		<i>z</i>	0.10740(87)			
S1	<i>site</i>	2( <i>a</i> )	S4	<i>site</i>	1( <i>a</i> )			
	<i>x</i>	0.3695(10)		<i>x</i>	0.13541(37)			
	<i>z</i>	0.6275(25)	S4	<i>site</i>	3( <i>b</i> )			
S2	<i>site</i>	2( <i>a</i> )		<i>x</i>	0.13803(46)			
	<i>x</i>	0.3716(12)	<i>z</i>	0.60140(83)				
	<i>z</i>	0.1161(21)						
S3	<i>site</i>	4( <i>b</i> )						
	<i>x</i>	0.63189(65)						
	<i>y</i>	0.73906(85)						
	<i>z</i>	0.6411(12)						
S4	<i>site</i>	2( <i>a</i> )						
	<i>x</i>	0.86672(91)						
	<i>z</i>	0.1373(22)						
S5	<i>site</i>	2( <i>a</i> )						
	<i>x</i>	0.8658(11)						
	<i>z</i>	0.5977(19)						
S6	<i>site</i>	4( <i>b</i> )						
	<i>x</i>	0.13345(66)						
	<i>y</i>	0.72488(78)						
	<i>z</i>	0.1241(13)						
R <sub>wp</sub> / %					2.92			
$\chi^2$					2.766			

<sup>a</sup> Ge fixed at origin *x x x*

<sup>b</sup> 2(*a*) and 3(*b*) sites are special positions at *x 0 z*

<sup>c</sup> 1(*a*) and 16(*e*) are special positions at *x x x*



**Table 10:** Final refined parameters for GeV<sub>4</sub>S<sub>8</sub> at 25 K.

<i>M</i> -GeV <sub>4</sub> S <sub>8</sub> ( <i>Cm</i> )			<i>R</i> -GeV <sub>4</sub> S <sub>8</sub> ( <i>R3m</i> )			<i>C</i> -GeV <sub>4</sub> S <sub>8</sub> ( <i>F4̄3m</i> )		
Weight Fraction / %		41(1)	Weight Fraction / %		39(1)	Weight Fraction / %		20(1)
<i>a</i> / Å		11.7790(3)	<i>a</i> / Å		6.79565(9)	<i>a</i> / Å		9.64073(17)
<i>b</i> / Å		6.83856(15)						
<i>c</i> / Å		6.79463(30)						
$\beta$ / °		125.065(2)	$\alpha$ / °		60.408(1)			
V / Å <sup>3</sup>		447.981(14)	V / Å <sup>3</sup>		223.959(3)	V / Å <sup>3</sup>		896.045(47)
<i>B</i> / Å <sup>2</sup>		0.3695(6)	<i>B</i> / Å <sup>2</sup>		0.3695(6)	<i>B</i> / Å <sup>2</sup>		2.866(3)
Ge <sup>a</sup>	<i>site</i>	2( <i>a</i> )	Ge <sup>a</sup>	<i>site</i>	1( <i>a</i> )	Ge <sup>a</sup>	<i>site</i>	4( <i>a</i> )
	<i>x</i>	0		<i>x</i>	0		<i>x</i>	0
V1	<i>site</i> <sup>b</sup>	2( <i>a</i> )	V1	<i>site</i> <sup>c</sup>	1( <i>a</i> )	V	<i>site</i> <sup>c</sup>	16( <i>e</i> )
	<i>x</i>	0.598(11)		<i>x</i>	0.4073(40)		<i>x</i>	0.6139(94)
	<i>z</i>	0.368(23)	V2	<i>site</i> <sup>b</sup>	3( <i>b</i> )	S1	<i>site</i>	16( <i>e</i> )
<i>site</i>	2( <i>a</i> )	<i>x</i>		0.4087(49)	<i>x</i>		0.3720(16)	
<i>x</i>	0.601(15)	<i>y</i>		0.8021(84)	S2	<i>site</i>	16( <i>e</i> )	
<i>z</i>	0.829(23)	S1	<i>site</i>	1( <i>a</i> )		<i>x</i>	0.8644(13)	
V3	<i>site</i>		4( <i>b</i> )	S1	<i>x</i>	0.63137(89)		
	<i>x</i>	0.3898(86)	S2		<i>site</i>	3( <i>b</i> )		
	<i>y</i>	0.2086(99)		<i>x</i>	0.63056(84)			
	<i>z</i>	0.396(23)	<i>z</i>	0.1122(15)				
S1	<i>site</i>	2( <i>a</i> )	S3	<i>site</i>	1( <i>a</i> )			
	<i>x</i>	0.3723(20)		<i>x</i>	0.13431(72)			
	<i>z</i>	0.6435(44)	S4	<i>site</i>	3( <i>b</i> )			
S2	<i>site</i>	2( <i>a</i> )		<i>x</i>	0.14037(77)			
	<i>x</i>	0.3684(22)	<i>z</i>	0.5946(13)				
	<i>z</i>	0.1110(46)						
S3	<i>site</i>	4( <i>b</i> )						
	<i>x</i>	0.6282(14)						
	<i>y</i>	0.7307(15)						
	<i>z</i>	0.6374(32)						
S4	<i>site</i>	2( <i>a</i> )						
	<i>x</i>	0.8604(19)						
	<i>z</i>	0.1327(44)						
S5	<i>site</i>	2( <i>a</i> )						
	<i>x</i>	0.8614(20)						
	<i>z</i>	0.6057(44)						
S6	<i>site</i>	4( <i>b</i> )						
	<i>x</i>	0.1328(14)						
	<i>y</i>	0.7339(17)						
	<i>z</i>	0.1254(32)						
R <sub>wp</sub> / %					6.37			
$\chi^2$					13.00			

<sup>a</sup> Ge fixed at origin *x x x*

<sup>b</sup> 2(*a*) and 3(*b*) sites are special positions at *x 0 z*

<sup>c</sup> 1(*a*) and 16(*e*) are special positions at *x x x*

**Table 11:** Final refined parameters for GeV<sub>4</sub>S<sub>8</sub> at 20 K.

<i>M</i> -GeV <sub>4</sub> S <sub>8</sub> ( <i>Cm</i> )			<i>R</i> -GeV <sub>4</sub> S <sub>8</sub> ( <i>R3m</i> )			<i>C</i> -GeV <sub>4</sub> S <sub>8</sub> ( <i>F43m</i> )		
Weight Fraction / %		44(1)	Weight Fraction / %		40(1)	Weight Fraction / %		16(1)
<i>a</i> / Å		11.7804(3)	<i>a</i> / Å		6.795207(85)	<i>a</i> / Å		9.64063(21)
<i>b</i> / Å		6.83886(15)						
<i>c</i> / Å		6.79385(28)						
$\beta$ / °		125.076(2)	$\alpha$ / °		60.421(1)			
V / Å <sup>3</sup>		447.939(13)	V / Å <sup>3</sup>		223.979(3)	V / Å <sup>3</sup>		896.016(57)
<i>B</i> / Å <sup>2</sup>		0.3521(5)	<i>B</i> / Å <sup>2</sup>		0.3521(5)	<i>B</i> / Å <sup>2</sup>		2.629(4)
Ge <sup>a</sup>	<i>site</i>	2( <i>a</i> )	Ge <sup>a</sup>	<i>site</i>	1( <i>a</i> )	Ge <sup>a</sup>	<i>site</i>	4( <i>a</i> )
	<i>x</i>	0		<i>x</i>	0		<i>x</i>	0
V1	<i>site</i> <sup>b</sup>	2( <i>a</i> )	V1	<i>site</i> <sup>c</sup>	1( <i>a</i> )	V	<i>site</i> <sup>c</sup>	16( <i>e</i> )
	<i>x</i>	0.607(14)		<i>x</i>	0.4048(44)		<i>x</i>	0.612(11)
	<i>z</i>	0.392(33)	V2	<i>site</i> <sup>b</sup>	3( <i>b</i> )	S1	<i>site</i>	16( <i>e</i> )
<i>site</i>	2( <i>a</i> )	<i>x</i>		0.3915(46)	<i>x</i>		0.3686(19)	
<i>x</i>	0.605(16)	<i>y</i>		0.8149(84)	S2	<i>site</i>	16( <i>e</i> )	
<i>z</i>	0.825(24)	S1	<i>site</i>	1( <i>a</i> )		<i>x</i>	0.8648(18)	
V3	<i>site</i>	4( <i>b</i> )	S1	<i>x</i>	0.63273(89)			
	<i>x</i>	0.3893(83)		S2	<i>site</i>	3( <i>b</i> )		
	<i>y</i>	0.204(10)	<i>x</i>		0.63254(97)			
	<i>z</i>	0.399(20)	<i>z</i>	0.1104(17)				
S1	<i>site</i>	2( <i>a</i> )	S3	<i>site</i>	1( <i>a</i> )			
	<i>x</i>	0.3707(23)		<i>x</i>	0.13500(72)			
	<i>z</i>	0.6284(58)	S4	<i>site</i>	3( <i>b</i> )			
S2	<i>site</i>	2( <i>a</i> )		<i>x</i>	0.13921(88)			
	<i>x</i>	0.3738(23)	<i>z</i>	0.5970(16)				
	<i>z</i>	0.1184(47)						
S3	<i>site</i>	4( <i>b</i> )						
	<i>x</i>	0.6286(14)						
	<i>y</i>	0.7347(18)						
	<i>z</i>	0.6386(31)						
S4	<i>site</i>	2( <i>a</i> )						
	<i>x</i>	0.8661(20)						
	<i>z</i>	0.1386(48)						
S5	<i>site</i>	2( <i>a</i> )						
	<i>x</i>	0.8622(19)						
	<i>z</i>	0.5956(42)						
S6	<i>site</i>	4( <i>b</i> )						
	<i>x</i>	0.1347(14)						
	<i>y</i>	0.7307(19)						
	<i>z</i>	0.1299(33)						
R <sub>wp</sub> / %					6.39			
$\chi^2$					13.34			

<sup>a</sup> Ge fixed at origin *x x x*

<sup>b</sup> 2(*a*) and 3(*b*) sites are special positions at *x 0 z*

<sup>c</sup> 1(*a*) and 16(*e*) are special positions at *x x x*

**Table 12:** Final refined parameters for GeV<sub>4</sub>S<sub>8</sub> at 19 K.

<i>M</i> -GeV <sub>4</sub> S <sub>8</sub> ( <i>Cm</i> )			<i>R</i> -GeV <sub>4</sub> S <sub>8</sub> ( <i>R3m</i> )			<i>C</i> -GeV <sub>4</sub> S <sub>8</sub> ( <i>F43m</i> )					
Weight Fraction / %		47(1)	Weight Fraction / %		36(1)	Weight Fraction / %		17(1)			
<i>a</i> / Å		11.7826(3)	<i>a</i> / Å		6.795033(91)		<i>a</i> / Å		9.64049(23)		
<i>b</i> / Å		6.83914(14)									
<i>c</i> / Å		6.79415(25)									
$\beta$ / °		125.091(2)	$\alpha$ / °		60.421(1)						
V / Å <sup>3</sup>		447.982(12)	V / Å <sup>3</sup>		223.964(3)		V / Å <sup>3</sup>		895.977(63)		
<i>B</i> / Å <sup>2</sup>		0.3632(6)	<i>B</i> / Å <sup>2</sup>		0.3632(6)		<i>B</i> / Å <sup>2</sup>		2.905(4)		
Ge <sup>a</sup>	<i>site</i>	2( <i>a</i> )	Ge <sup>a</sup>	<i>site</i>	1( <i>a</i> )	Ge <sup>a</sup>	<i>site</i>	4( <i>a</i> )			
	<i>x</i>	0		<i>x</i>	0		<i>x</i>	0			
V1	<i>site</i> <sup>b</sup>	2( <i>a</i> )	V1	<i>site</i> <sup>c</sup>	1( <i>a</i> )	V	<i>site</i> <sup>c</sup>	16( <i>e</i> )			
	<i>x</i>	0.606(13)		<i>x</i>	0.4124(41)		<i>x</i>	0.611(12)			
	<i>z</i>	0.378(31)	V2	<i>site</i> <sup>b</sup>	3( <i>b</i> )	S1	<i>site</i>	16( <i>e</i> )			
V2	<i>site</i>	2( <i>a</i> )		<i>x</i>	0.3981(53)		<i>x</i>	0.3732(16)			
	<i>x</i>	0.602(13)		<i>y</i>	0.8104(91)	S2	<i>site</i>	16( <i>e</i> )			
	<i>z</i>	0.814(22)	S1	<i>site</i>	1( <i>a</i> )		<i>x</i>	0.8603(14)			
V3	<i>site</i>	4( <i>b</i> )		<i>x</i>	0.63361(87)						
	<i>x</i>	0.3837(68)	S2	<i>site</i>	3( <i>b</i> )						
	<i>y</i>	0.2022(87)		<i>x</i>	0.63597(98)						
	<i>z</i>	0.384(21)	<i>z</i>	0.1045(18)							
S1	<i>site</i>	2( <i>a</i> )	S3	<i>site</i>	1( <i>a</i> )						
	<i>x</i>	0.3675(20)		<i>x</i>	0.13565(76)						
	<i>z</i>	0.6194(51)	S4	<i>site</i>	3( <i>b</i> )						
S2	<i>site</i>	2( <i>a</i> )		<i>x</i>	0.13801(97)						
	<i>x</i>	0.3659(22)	<i>z</i>	0.6000(17)							
	<i>z</i>	0.1062(42)									
S3	<i>site</i>	4( <i>b</i> )									
	<i>x</i>	0.6296(11)									
	<i>y</i>	0.7385(16)									
	<i>z</i>	0.6328(29)									
S4	<i>site</i>	2( <i>a</i> )									
	<i>x</i>	0.8613(18)									
	<i>z</i>	0.1266(43)									
S5	<i>site</i>	2( <i>a</i> )									
	<i>x</i>	0.8646(21)									
	<i>z</i>	0.5935(39)									
S6	<i>site</i>	4( <i>b</i> )									
	<i>x</i>	0.1254(11)									
	<i>y</i>	0.7271(15)									
	<i>z</i>	0.1154(27)									
R <sub>wp</sub> / %					6.42						
$\chi^2$					13.37						

<sup>a</sup> Ge fixed at origin *x x x*

<sup>b</sup> 2(*a*) and 3(*b*) sites are special positions at *x 0 z*

<sup>c</sup> 1(*a*) and 16(*e*) are special positions at *x x x*

**Table 13:** Final refined parameters for GeV<sub>4</sub>S<sub>8</sub> at 18 K.

<i>M</i> -GeV <sub>4</sub> S <sub>8</sub> ( <i>Cm</i> )			<i>R</i> -GeV <sub>4</sub> S <sub>8</sub> ( <i>R3m</i> )			<i>C</i> -GeV <sub>4</sub> S <sub>8</sub> ( <i>F43m</i> )		
Weight Fraction / %	50(1)		Weight Fraction / %	36(1)		Weight Fraction / %	14(1)	
<i>a</i> / Å	11.7845(3)		<i>a</i> / Å	6.79521(10)		<i>a</i> / Å	9.64098(36)	
<i>b</i> / Å	6.83855(15)							
<i>c</i> / Å	6.79472(16)		<i>a</i> / °	60.419(1)				
<i>β</i> / °	125.106(2)							
V / Å <sup>3</sup>	447.966(6)		V / Å <sup>3</sup>	223.968(4)		V / Å <sup>3</sup>	896.11(10)	
<i>B</i> / Å <sup>2</sup>	0.2937(5)		<i>B</i> / Å <sup>2</sup>	0.2937(5)		<i>B</i> / Å <sup>2</sup>	2.688(5)	
Ge <sup>a</sup>	<i>site</i>	2( <i>a</i> )	Ge <sup>a</sup>	<i>site</i>	1( <i>a</i> )	Ge <sup>a</sup>	<i>site</i>	4( <i>a</i> )
	<i>x</i>	0		<i>x</i>	0		<i>x</i>	0
V1	<i>site</i> <sup>b</sup>	2( <i>a</i> )	V1	<i>site</i> <sup>c</sup>	1( <i>a</i> )	V	<i>site</i> <sup>c</sup>	16( <i>e</i> )
	<i>x</i>	0.599(12)		<i>x</i>	0.4039(50)		<i>x</i>	0.618(17)
	<i>z</i>	0.383(23)	V2	<i>site</i> <sup>b</sup>	3( <i>b</i> )	S1	<i>site</i>	16( <i>e</i> )
V2	<i>site</i>	2( <i>a</i> )		<i>x</i>	0.3922(52)		<i>x</i>	0.3732(26)
	<i>x</i>	0.606(11)		<i>y</i>	0.8170(86)	S2	<i>site</i>	16( <i>e</i> )
	<i>z</i>	0.803(18)	S1	<i>site</i>	1( <i>a</i> )		<i>x</i>	0.8643(21)
V3	<i>site</i>	4( <i>b</i> )		S1	<i>x</i>	0.6303(10)		
	<i>x</i>	0.3788(65)	S2		<i>site</i>	3( <i>b</i> )		
	<i>y</i>	0.2017(75)		<i>x</i>	0.6340(11)			
	<i>z</i>	0.383(18)	<i>z</i>	0.1107(19)				
S1	<i>site</i>	2( <i>a</i> )	S3	<i>site</i>	1( <i>a</i> )			
	<i>x</i>	0.3680(19)		<i>x</i>	0.13490(81)			
	<i>z</i>	0.6284(44)	S4	<i>site</i>	3( <i>b</i> )			
S2	<i>site</i>	2( <i>a</i> )		<i>x</i>	0.1393(10)			
	<i>x</i>	0.3634(18)	<i>z</i>	0.5974(18)				
	<i>z</i>	0.0957(31)						
S3	<i>site</i>	4( <i>b</i> )						
	<i>x</i>	0.6267(13)						
	<i>y</i>	0.7364(16)						
	<i>z</i>	0.6307(28)						
S4	<i>site</i>	2( <i>a</i> )						
	<i>x</i>	0.8597(17)						
	<i>z</i>	0.1280(39)						
S5	<i>site</i>	2( <i>a</i> )						
	<i>x</i>	0.8669(19)						
	<i>z</i>	0.5995(32)						
S6	<i>site</i>	4( <i>b</i> )						
	<i>x</i>	0.1305(12)						
	<i>y</i>	0.7279(16)						
	<i>z</i>	0.1237(27)						
R <sub>wp</sub> / %					6.39			
$\chi^2$					13.17			

<sup>a</sup> Ge fixed at origin *x x x*

<sup>b</sup> 2(*a*) and 3(*b*) sites are special positions at *x 0 z*

<sup>c</sup> 1(*a*) and 16(*e*) are special positions at *x x x*

**Table 14:** Final refined parameters for  $M\text{-GeV}_4\text{S}_8$  at 15 K and 7 K.

T / K		15	7
$a / \text{\AA}$		11.78212(17)	11.79171(25)
$b / \text{\AA}$		6.83613(7)	6.839798(26)
$c / \text{\AA}$		6.79653(11)	6.794112(25)
$\beta / ^\circ$		125.081(1)	125.170(1)
$V / \text{\AA}^3$		447.942(1)	447.931(1)
$B / \text{\AA}^2$		0.1171(2)	0.1234(2)
Ge <sup>a</sup>	<i>site</i>	2( <i>a</i> )	
	<i>x</i>	0	0
V1	<i>site</i> <sup>b</sup>	2( <i>a</i> )	
	<i>x</i>	0.6023(34)	0.6067(68)
	<i>z</i>	0.4121(70)	0.410(11)
V2	<i>site</i>	2( <i>a</i> )	
	<i>x</i>	0.6130(39)	0.6084(71)
	<i>z</i>	0.8256(41)	0.8202(85)
V3	<i>site</i>	4( <i>b</i> )	
	<i>x</i>	0.3877(12)	0.3888(12)
	<i>y</i>	0.2014(13)	0.2058(13)
	<i>z</i>	0.3890(62)	0.389(10)
S1	<i>site</i>	2( <i>a</i> )	
	<i>x</i>	0.3674(6)	0.36826(85)
	<i>z</i>	0.6376(11)	0.6367(14)
S2	<i>site</i>	2( <i>a</i> )	
	<i>x</i>	0.3679(7)	0.36808(90)
	<i>z</i>	0.1186(10)	0.1183(15)
S3	<i>site</i>	4( <i>b</i> )	
	<i>x</i>	0.6287(2)	0.62878(24)
	<i>y</i>	0.7375(3)	0.73709(26)
	<i>z</i>	0.6281(9)	0.6257(10)
S4	<i>site</i>	2( <i>a</i> )	
	<i>x</i>	0.8634(7)	0.8646(12)
	<i>z</i>	0.1317(12)	0.1368(16)
S5	<i>site</i>	2( <i>a</i> )	
	<i>x</i>	0.8645(7)	0.8626(12)
	<i>z</i>	0.5969(11)	0.5986(20)
S6	<i>site</i>	4( <i>b</i> )	
	<i>x</i>	0.1329(2)	0.13241(22)
	<i>y</i>	0.7291(2)	0.72888(23)
	<i>z</i>	0.1443(7)	0.14263(75)
$R_{\text{wp}} / \%$		2.85	2.88
$\chi^2$		2.614	2.701

<sup>a</sup> Ge fixed at origin  $x x x$ <sup>b</sup> 2(*a*) site is a special position at  $x 0 z$

**Table 15:** Selected bond lengths of  $C\text{-GeV}_4\text{S}_8$ .

T / K	32	31	30	29	
Bond lengths / Å	Ge-S2	2.254(6)	2.255(4)	2.267(9)	2.276(10)
	V1-V1	2.875(6)	3.003(33)	3.02(10)	3.02(11)
	V1-S1	2.2979(15)	2.335(10)	2.332(32)	2.323(35)
	V1-S2	2.5348(24)	2.480(14)	2.47(4)	2.46(5)
T / K	25	20	19	18	
Bond lengths / Å	Ge-S2	2.268(21)	2.258(30)	2.332(23)	2.267(35)
	V1-V1	3.10(26)	3.06(29)	3.04(32)	3.2(5)
	V1-S1	2.34(9)	2.36(9)	2.31(10)	2.36(16)
	V1-S2	2.43(11)	2.46(12)	2.43(14)	2.39(19)

**Table 16:** Selected bond lengths and angles of *R*-GeV<sub>4</sub>S<sub>8</sub>.

T / K	32	31	30	29	
Bond lengths / Å	Ge-S3	2.24(4)	2.241(18)	2.267(12)	2.248(6)
	Ge-S4	3 × 2.149(19)	2.264(10)	2.238(8)	2.224(5)
	V1-V2	2.99311(7)	3.00(11)	2.77(7)	2.651(31)
	V2-V2	2.80871(10)	2.83(11)	2.89(7)	2.86(4)
	V1-S2	2.332(22)	2.33(5)	2.225(28)	2.234(13)
	V1-S4	2.376(21)	2.44(7)	2.61(5)	2.659(25)
	V2-S1	2.329(25)	2.17(8)	2.27(5)	2.332(24)
	V2-S2	2.362(17)	2.34(6)	2.324(33)	2.276(14)
	V2-S3	2.646(17)	2.63(7)	2.55(5)	2.537(24)
	V2-S4	2.627(14)	2.50(6)	2.54(4)	2.599(18)
	V2-V1-V2	55.964(2)	56.2(29)	63.0(21)	65.3(11)
	V1-V2-V2	62.018(2)	61.9(15)	58.5(11)	57.3(5)
	T / K	25	20	19	18
	Bond lengths / Å	Ge-S3	2.232(12)	2.240(12)	2.251(13)
Ge-S4		2.261(7)	2.249(9)	2.232(10)	3 × 2.247(10)
V1-V2		2.69(7)	2.70(6)	2.61(7)	3 × 2.73(7)
V2-V2		2.70(8)	2.89(8)	2.82(9)	3 × 2.90(9)
V1-S2		2.208(25)	2.246(30)	2.235(25)	3 × 2.26(4)
V1-S4		2.63(5)	2.60(5)	2.70(5)	3 × 2.59(6)
V2-S1		2.18(5)	2.36(4)	2.30(5)	2.32(5)
V2-S2		2.29(4)	2.261(27)	2.293(31)	2 × 2.266(31)
V2-S3		2.67(5)	2.51(5)	2.57(5)	2.52(5)
V2-S4		2.58(4)	2.59(4)	2.59(4)	2 × 2.57(4)
Bond angles / °	V2-V1-V2	60.4(22)	64.8(20)	65.3(24)	64.3(23)
	V1-V2-V2	59.8(11)	57.6(10)	57.3(12)	57.9(11)

**Table 17:** Selected bond lengths and angles of *M*-GeV<sub>4</sub>S<sub>8</sub>.

T / K	31	30	29	25	20	
Bond lengths / Å	Ge-S4	2.165(25)	2.235(18)	2.241(8)	2.277(16)	2.254(17)
	Ge-S5	2.28(4)	2.267(23)	2.237(10)	2.206(23)	2.249(23)
	Ge-S6	2.179(21)	2.219(15)	2.280(5)	2.223(11)	2.254(11)
	V1-V2	2.93(29)	3.20(21)	3.00(7)	3.11(15)	2.95(14)
	V1-V3	2.89(20)	2.93(13)	2.95(5)	2.92(10)	2.94(10)
	V2-V3	2.63(21)	2.99(15)	2.96(5)	2.91(11)	2.89(11)
	V3-V3	2.66(28)	2.60(16)	2.76(6)	2.84(14)	2.79(14)
	V1-S2	2.19(25)	2.33(15)	2.30(7)	2.22(11)	2.27(14)
	V1-S3	2.46(15)	2.52(10)	2.39(5)	2.47(8)	2.38(11)
	V1-S5	2.52(23)	2.51(15)	2.50(6)	2.55(10)	2.48(12)
	V1-S6	2.58(13)	2.41(9)	2.50(5)	2.50(8)	2.54(11)
	V2-S1	2.00(22)	2.32(18)	2.30(8)	2.23(15)	2.28(16)
	V2-S3	2.30(14)	2.36(10)	2.30(5)	2.39(11)	2.32(12)
	V2-S4	2.83(20)	2.44(17)	2.53(7)	2.52(14)	2.54(14)
	V2-S6	2.58(15)	2.40(12)	2.42(6)	2.42(11)	2.47(13)
	V3-S1	2.27(17)	2.28(10)	2.26(6)	2.31(12)	2.19(10)
	V3-S2	2.22(16)	2.03(9)	2.20(5)	2.29(11)	2.28(10)
	V3-S3	2.42(20)	2.42(10)	2.406(35)	2.34(8)	2.35(8)
V3-S4	2.68(16)	2.60(10)	2.56(5)	2.57(11)	2.60(9)	
V3-S5	2.65(15)	2.69(8)	2.60(4)	2.58(9)	2.55(9)	
V3-S6	2.51(18)	2.56(9)	2.487(32)	2.52(8)	2.50(8)	
Bond angles / °	V2-V1-V3	54(5)	58.3(34)	59.7(13)	57.6(27)	58.6(31)
	V3-V1-V3	55(8)	53(4)	55.8(18)	58(4)	56(4)
	V1-V2-V3	62(7)	56(4)	59.3(19)	58.0(34)	61(4)
	V3-V2-V3	61(9)	51(4)	55.6(17)	58(4)	58(4)
	V1-V3-V2	64(9)	65(5)	61.0(18)	64.3(34)	60.9(34)
	V1-V3-V3	63(4)	63.7(22)	62.1(9)	60.9(18)	61.8(18)
	V2-V3-V3	60(5)	64.3(20)	62.2(9)	60.8(19)	61.2(20)



**Table 17 continued:** Selected bond lengths and angles of *M*-GeV<sub>4</sub>S<sub>8</sub>.

T / K	19	18	15	7
Ge-S4	2.243(16)	2.268(14)	2.24761(1)	2.263(11)
Ge-S5	2.260(22)	2.226(18)	2.23949(1)	2.230(11)
Ge-S6	2.225(9)	2 × 2.247(9)	2 × 2.25371(1)	2 × 2.2522(15)
V1-V2	2.99(12)	2.81(10)	2.73993(1)	2.775(25)
V1-V3	2.99(11)	2 × 2.94(10)	2 × 2.80543(1)	2 × 2.86(6)
V2-V3	2.90(11)	2 × 2.90(11)	2 × 2.94587(2)	2 × 2.92(6)
V3-V3	2.77(12)	2.76(10)	2.75474(1)	2.815(18)
V1-S2	2.33(14)	2.30(12)	2.29616(2)	2.33(7)
V1-S3	2.39(11)	2 × 2.36(8)	2 × 2.22486(1)	2 × 2.238(30)
V1-S5	2.51(12)	2.61(11)	2.58092(2)	2.51(6)
V1-S6	2.47(11)	2 × 2.53(8)	2 × 2.57813(1)	2 × 2.55(4)
V2-S1	2.27(13)	2.33(11)	2.39914(2)	2.35(7)
V2-S3	2.30(11)	2 × 2.24(6)	2 × 2.31202(1)	2 × 2.325(35)
V2-S4	2.53(12)	2.50(11)	2.44395(2)	2.50(7)
V2-S6	2.45(12)	2 × 2.56(8)	2 × 2.57174(1)	2 × 2.57(4)
V3-S1	2.20(11)	2.23(8)	2.29605(1)	2.31(6)
V3-S2	2.25(11)	2.31(9)	2.19864(1)	2.22(5)
V3-S3	2.41(7)	2.43(6)	2.36061(2)	2.346(12)
V3-S4	2.60(10)	2.60(7)	2.59507(1)	2.55(4)
V3-S5	2.57(9)	2.57(8)	2.58534(1)	2.58(4)
V3-S6	2.54(6)	2.44(6)	2.50308(2)	2.512(11)
V2-V1-V3	58.0(30)	60.6(31)	64.2(9)	62.4(20)
V3-V1-V3	55.2(34)	56.0(30)	58.7(8)	58.9(13)
V1-V2-V3	61(4)	61.9(34)	59.1(10)	60.3(21)
V3-V2-V3	57(4)	56.7(32)	55.7(7)	57.6(14)
V1-V3-V3	62.4(17)	62.0(15)	60.7(4)	60.5(7)
V1-V3-V2	61.1(32)	57.5(25)	56.7(5)	57.4(6)
V2-V3-V3	61.5(18)	61.6(16)	62.15(34)	61.2(7)

Bond lengths / Å

Bond angles / °

The crystal structures of  $C\text{-GeV}_4\text{S}_8$  (Figure 40),  $R\text{-GeV}_4\text{S}_8$  (Figure 41) and  $M\text{-GeV}_4\text{S}_8$  (Figure 42) are depicted below, showing the heterocubane-like  $\text{V}_4\text{S}_4^{4+}$  units and  $\text{GeV}_4^{4+}$  tetrahedra.

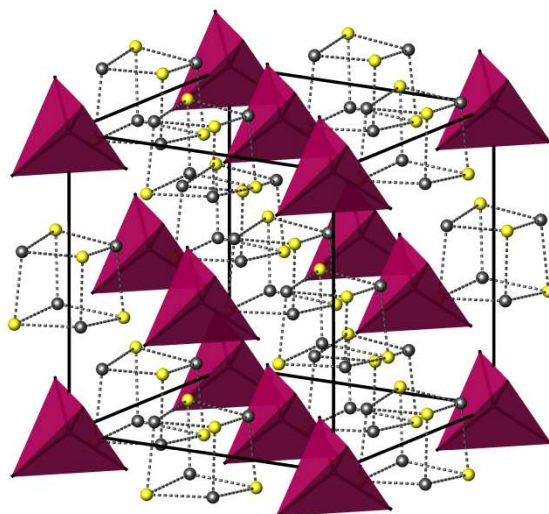


**Figure 40:**  $C\text{-GeV}_4\text{S}_8$  in  $F\bar{4}3m$  at 29K. Sulphur atoms are shown as yellow spheres, vanadium atoms as grey spheres, with a solid line representing a V-S bond.  $\text{GeV}_4^{4+}$  units are represented by pink tetrahedra.

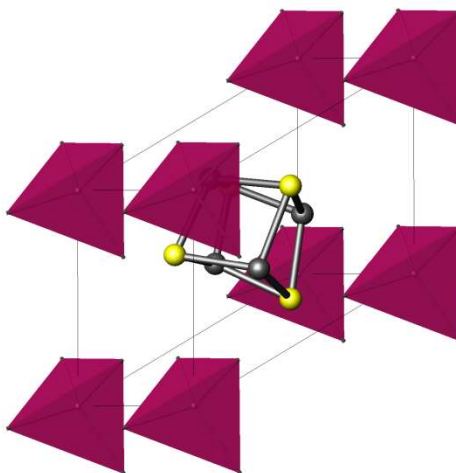


**Figure 41:**  $R\text{-GeV}_4\text{S}_8$  in  $R3m$  at 29K. Sulphur atoms are shown as yellow spheres, vanadium atoms as grey spheres, with a solid line representing a V-S bond.  $\text{GeV}_4^{4+}$  units are represented by pink tetrahedra.

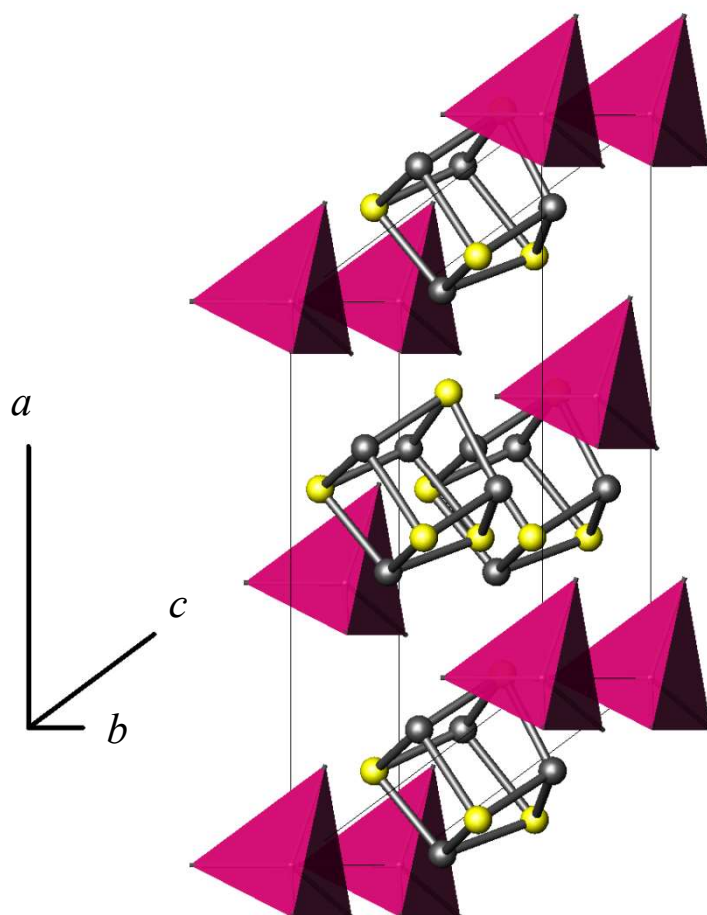


**Figure 42:**  $M\text{-GeV}_4\text{S}_8$  in  $Cm$  at 29K. Sulphur atoms are shown as yellow spheres, vanadium atoms as grey spheres, with a solid line representing a V-S bond.  $\text{GeV}_4^{4+}$  units are represented by pink tetrahedra.

The fraction of  $C\text{-GeV}_4\text{S}_8$ ,  $R\text{-GeV}_4\text{S}_8$  and  $M\text{-GeV}_4\text{S}_8$  polymorphs present in  $\text{GeV}_4\text{S}_8$  is shown in Figure 43. The observed changes in powder neutron diffraction data can be attributed to the varying amounts of the  $C\text{-GeV}_4\text{S}_8$ ,  $R\text{-GeV}_4\text{S}_8$  and  $M\text{-GeV}_4\text{S}_8$  phases present and the individual distortions associated with each polymorph at a given temperature.

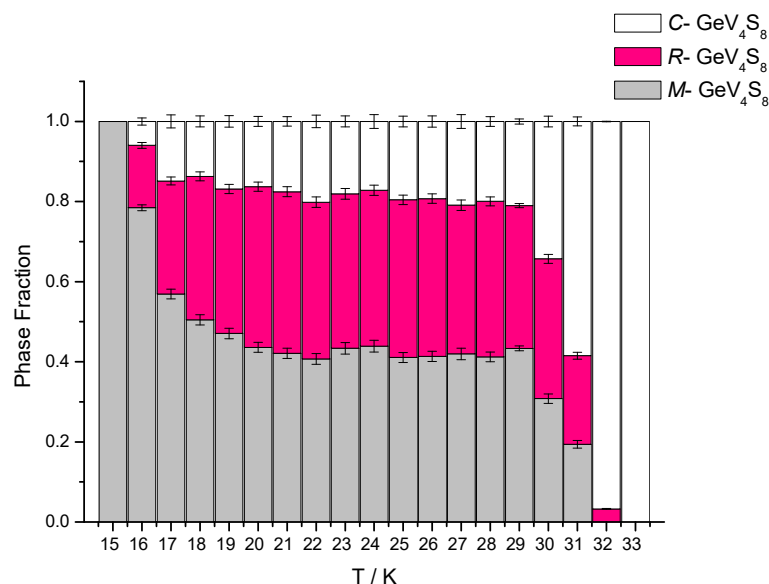


**Figure 43:** Graph showing temperature dependence of each polymorph of GeV<sub>4</sub>S<sub>8</sub>. Above 32 K GeV<sub>4</sub>S<sub>8</sub> is cubic ( $F\bar{4}3m$ ). Below 16 K GeV<sub>4</sub>S<sub>8</sub> is monoclinic ( $Cm$ ). Error bars are shown.

The trends observed in the phase fractions, determined by Rietveld refinement, are consistent with the profile of the raw data (Figure 24 and Figure 25). There are three obvious regions; at higher temperatures there is an increasing amount of C-GeV<sub>4</sub>S<sub>8</sub>; throughout the middle of the range,  $20 \leq T / K \leq 29$ , the phase fractions remain constant, within error; at lower temperatures there is an increasing amount of M-GeV<sub>4</sub>S<sub>8</sub>.

At 32 K, 96.73(5) % of the composition is C-GeV<sub>4</sub>S<sub>8</sub>. The fraction of C-GeV<sub>4</sub>S<sub>8</sub> then decreases rapidly over 3 K to 21.0(6) %, where it then remains, within error, before decreasing again beyond 20 K.

R-GeV<sub>4</sub>S<sub>8</sub> is the only polymorph where the amount progressively increases from zero to 40(1) % before then decreasing to zero at 15 K, i.e. R-GeV<sub>4</sub>S<sub>8</sub> never exists as a single phase. The rhombohedral phase shows a horseshoe shaped trend as both lattice parameters vary with temperature (Figure 44). When the amount of R-GeV<sub>4</sub>S<sub>8</sub> increases, the unit cell length decreases. The unit cell angle,  $\alpha$ , exhibits the converse. As the fraction increases, the cell angle increases.

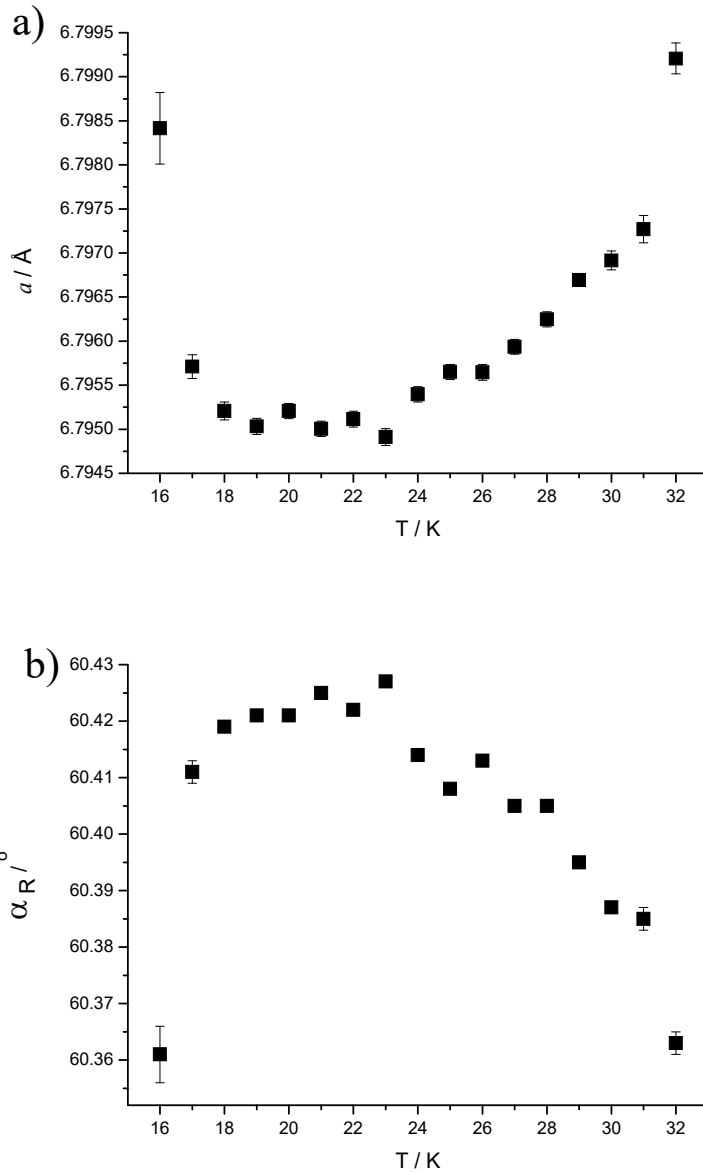


**Figure 44:** Temperature dependence of unit cell parameters for  $R\text{-GeV}_4\text{S}_8$ ; a)  $a$  lattice constant; b)  $\alpha$  angle. Error bars are shown.

There is 19(1) %  $M\text{-GeV}_4\text{S}_8$  present at 31 K. The fraction increases to 43.4(6) % at 29 K, between 28 K and 21 K there is a plateau, before increasing again from 43.6(13) % at 20 K to 100 % at 15 K. The fractional increase of  $M\text{-GeV}_4\text{S}_8$  results from an expansion of the  $a$  lattice parameter and the  $\beta$  angle within the unit cell (Figure 45). The temperature dependences of the  $b$  and  $c$  lattice parameters do not follow the same trend as that observed in  $a$ , in fact  $b$  increases rapidly between 31 K and 21 K and  $c$  decreases. Both, however, do show a small discontinuity at 18 K (Figure 46).

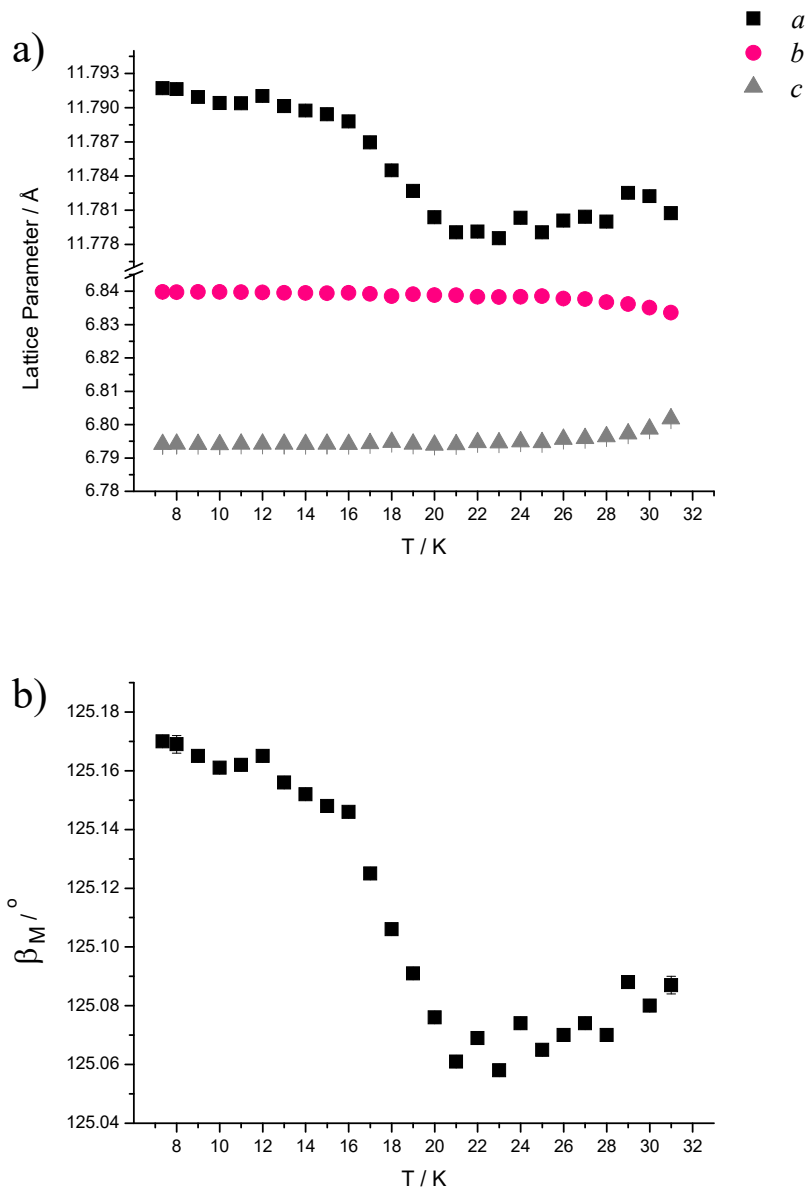


**Figure 45:** Temperature dependence of the unit cell parameters for  $M\text{-GeV}_4\text{S}_8$ ; a)  $a$ ,  $b$ ,  $c$  lattice constants; b)  $\beta$  angle. Error bars are shown.

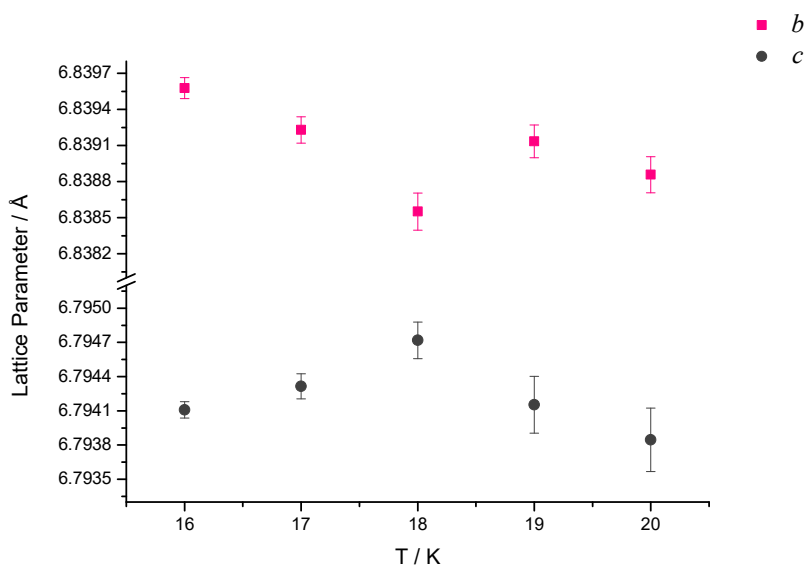


**Figure 46:** Graph showing discontinuities at 18 K in the  $b$  and  $c$  lattice parameters of  $M\text{-GeV}_4\text{S}_8$ . Error bars are shown.

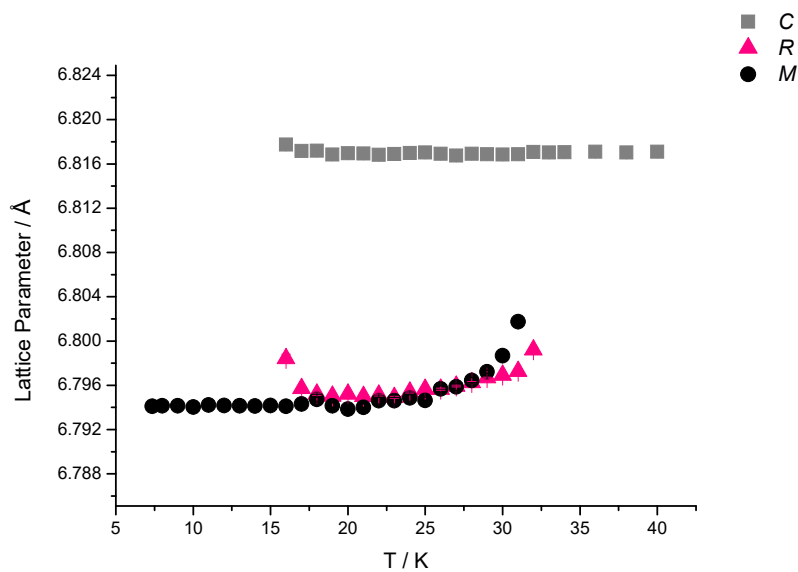


**Figure 47:** Comparison of the temperature dependence of the unit cell parameters for  $C\text{-GeV}_4\text{S}_8$  (grey squares),  $R\text{-GeV}_4\text{S}_8$  (pink triangles) and  $M\text{-GeV}_4\text{S}_8$  (black circles). Error bars are shown.<sup>a</sup>

<sup>a</sup> To aid comparison, lattice parameters for the cubic structure have been converted to a rhombohedral unit cell through  $a_R = a_C / \sqrt{2}$ . For  $M\text{-GeV}_4\text{S}_8$ ,  $c_M$  is geometrically equivalent to  $a_R$  and is thus shown here.

Phase transitions in  $\text{GeV}_4\text{S}_8$  are influenced by the distortions within the  $\text{V}_4\text{S}_4^{4+}$  cubane-like units. These distortions are observed in the temperature variation of the lattice parameters (Figure 47). The distortions can be quantified using the following expression[11]:

$$t = \frac{1}{6} \sum_{i=1}^6 |\langle d \rangle - d_i|$$

**Equation (40)**

where  $t$  is the extent of the distortion,  $\langle d \rangle$  is the mean V-V distance and  $d_i$  are the individual V-V distances. The summation is over all bonds within the  $\text{V}_4$ -cluster. The transition from cubic to rhombohedral symmetry results in an average  $t$  of *ca.* 15 %. However, from cubic to monoclinic the distortion is less pronounced with an average  $t$  of *ca.* 8 %.

Upon cooling from 32 K, the cubic unit cell exhibits a simple expansion of the  $\text{V}_4$ -cluster until the vanadium atoms are no longer within bonding distance at 16 K. This is a marker for the second transition occurring in this lower temperature region.

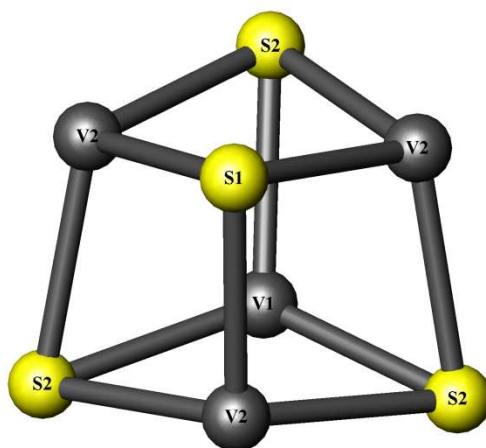


**Figure 48:**  $R\text{-GeV}_4\text{S}_8$ :  $\text{V}_4\text{S}_4^{4+}$  cubane unit.

As the symmetry is reduced from  $F\bar{4}3m$  to  $R3m$ , a contraction occurs along a threefold rotation axis. The V1-V2 bond (see Figure 48 for schematic) is shortened from 2.909(4) Å at room temperature, to 2.651(31) Å at 29 K, whilst the V2-V2 bond length is 2.84(6) Å. This contraction expands the



V(2)-V(1)-V(2) angle from  $60^\circ$  to  $65.3(11)^\circ$  at 29 K. At 17 K, prior to the transition where the rhombohedral phase is no longer present, the V1-V2 bonding distance increases to  $3.00(18)$  Å. This is also a marker for the transition occurring in this lower temperature region.

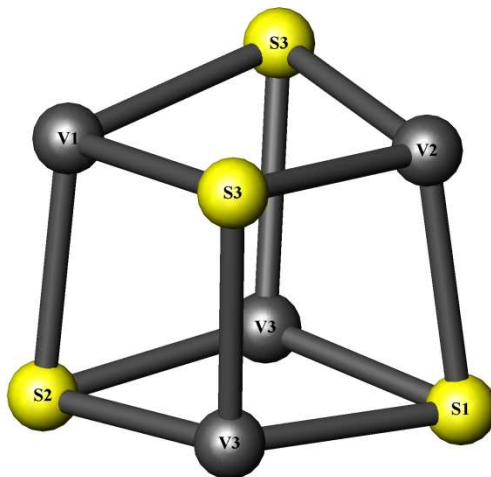


**Figure 49:** *M-GeV<sub>4</sub>S<sub>8</sub>*:  $V_4S_4^{4+}$  cubane unit.

When the symmetry is further reduced to *Cm*, this 3-fold axis is destroyed and only a mirror plane remains through the atoms S2-V1-V2-S1 within the  $V_4S_4^{4+}$  cubane-like unit. The distortion to a monoclinic unit cell, from the rhombohedral, is then associated with the expansion of one V-V bond. At 31 K the bond lengths within the  $V_4$ -cluster of *M-GeV<sub>4</sub>S<sub>8</sub>* show the same trend as the rhombohedral phase in that there are two shorter bonds, V2-V3 is  $2.63(21)$  Å and V3-V3 is  $2.66(28)$  Å and two longer bonds, V1-V2 is  $2.93(29)$  Å and V1-V3 is  $2.89(20)$  Å. At 29 K the  $V_4$ -cluster of *M-GeV<sub>4</sub>S<sub>8</sub>* has one short V-V bond, V3-V3 is  $2.76(6)$  Å, with the remaining three, V1-V2, V1-V3 and V2-V3 measuring  $3.00(7)$  Å,  $2.95(5)$  Å and  $2.96(5)$  Å respectively. One shorter bond within the  $V_4$ -cluster, compared with two of the rhombohedral phase, results in smaller bond angles between the vanadium atoms within the mirror plane, V1 and V2, and those either side of it, the V3 site, Figure 49. The V3-V1-V3 angle is  $55.8(18)^\circ$  and V3-V2-V3 angle is  $55.6(17)^\circ$ . This trend persists to 19 K. At 18 K the V1-V2 bond then starts to contract from  $2.99(12)$  Å at 19 K to  $2.775(25)$  Å at 7 K. The V3-V1-V3 angle is, therefore, now increased from  $55.8(18)^\circ$  at 29 K to  $58.9(13)^\circ$  at 7 K and the V3-V2-V3 angle to  $57.6(14)^\circ$ .

#### 3.4.4 Magnetic measurements of GeV<sub>4</sub>S<sub>8</sub>

Magnetic susceptibility data collected for GeV<sub>4</sub>S<sub>8</sub> at a field of 1000 G are presented in Figure 50. Zero-field-cooled and field-cooled data overlie each other throughout the majority of the temperature range, a slight deviation is seen at 2 K and 3 K. The data were fitted using Curie-Weiss law. The magnetic parameters have been derived from the fits to the reciprocal susceptibility data. In a previous experiment [20], these data were fitted using a temperature independent term,  $\chi_0 = 5.0(2) \times 10^{-4} \text{ cm}^3 \text{ mol}^{-1}$ . This was not possible due to the limited temperature region that was investigated on this sample.

The magnetic susceptibility data show two discontinuities. The first, at 31 K, is consistent with the onset of the structural distortions, i.e.  $T_S = 31.001 \text{ K}$ . In the region above this discontinuity,  $32 \leq T / \text{K} \leq 40$ , the Weiss temperature is  $\theta = -42.0(2) \text{ K}$  and the Curie constant,  $C = 1.185(7)$ . The effective magnetic moment is  $\mu_{\text{eff}} = 1.539(7) \mu_B$ . In the region below this discontinuity,  $18 \leq T / \text{K} \leq 30$ , the Weiss temperature is  $\theta = -47.1(8) \text{ K}$  and the Curie constant,  $C = 1.27(1)$ . The effective magnetic moment is  $\mu_{\text{eff}} = 1.59(1) \mu_B$ . The negative Weiss constants suggest that the dominant exchange interactions are antiferromagnetic in origin. The onset of antiferromagnetic order is observed at 19 K,  $T_N = 17.8 \text{ K}$ . The transition temperatures were determined by differentiating the molar susceptibility with respect to temperature. Antiferromagnetic ordering is not obvious in the neutron data; this could be because the Bragg peaks are superimposed on the magnetic peaks.

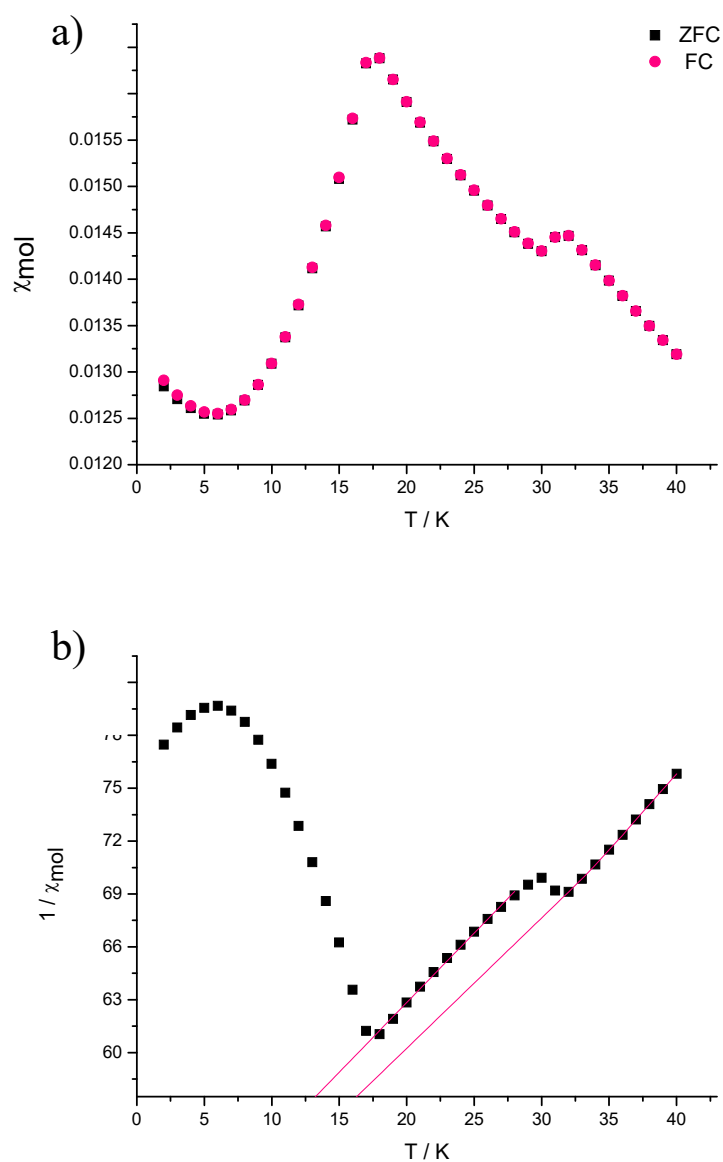


**Figure 50:** a) zero-field cooled and field cooled molar magnetic susceptibilities measured in a field of 1000 G. b) observed (points) and calculated (red line) reciprocal susceptibility data. The calculated line is derived from the fit to Curie-Weiss law.

### 3.5 Discussion

High resolution neutron diffraction experiments have revealed that there are three distinct trends in the behaviour of  $\text{GeV}_4\text{S}_8$  as the material is cooled to 7 K. Structural refinements of these data reveal that there are three distinct polymorphs, of which one has not been previously determined.  $\text{GeV}_4\text{S}_8$  adopts a defect spinel structure, space group  $F\bar{4}3m$ , as observed in previous work [13] and the  $\text{GaMo}_4\text{S}_8$ -type phases [6, 21], at room temperature. Neutron diffraction experiments reveal a series of peak splittings and broadenings upon cooling to indicate a deviation from the face-centred cubic structure. It is quite clear that the fine structure is qualitatively different at 25 K compared with 10 K, a result that is only acknowledged by Chudo *et al.*. The data presented by Johrendt *et al.*, Figure 51, show the disappearance of the central peak intensity occurring simultaneously with the appearance of the satellite peaks followed by the addition of intensity back into the central peak at 10K. This observed temperature dependence of the diffraction profile is the same in both the neutron and the X-ray experiments (see Figure 25 for neutron data). Johrendt *et al.*, have reported a phase transition directly from the cubic to the orthorhombic structure but this would be characterised by only a decrease in the central peak intensity with the simultaneous, gradual, appearance of the satellite peaks. However, what is observed is different. After the appearance of the satellite peaks at 30 K, the intensities remain level before the central peak increases again at 17 K. An orthorhombic phase cannot fit a reduced size central peak in this plateau region whilst still maintaining intensity in the satellites. This is because the allowed profile for the three orthorhombic reflections, originating from the cubic [440], is a 1:4:1 ratio.

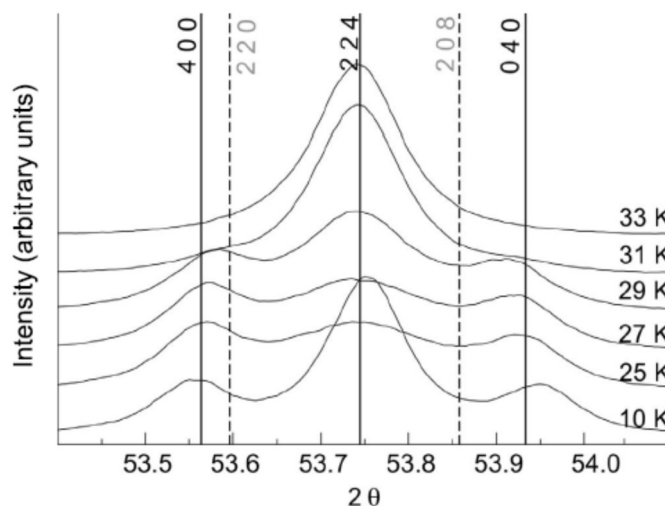


**Figure 51:** X-ray diffraction data ( $1.694 \leq d / \text{\AA} \leq 1.714$ ) collected by Johrendt *et al.* for  $10 \leq T / \text{K} \leq 33$ . Reflection positions are marked for  $O\text{-GeV}_4\text{S}_8$  (solid lines) and  $R\text{-GeV}_4\text{S}_8$  (dashed lines)[14].

A reduction in symmetry to  $R3m$ , at  $T_S = 32 \text{ K}$ , is in sharp contrast with the report of Johrendt *et al.*, who see no such distortion, but is consistent with that of Chudo *et al.*. However, Chudo *et al.* have never published any diffraction data or structural refinements. The reduction in symmetry is a result of an elongation of a  $C_3$  rotation axis resulting in  $\alpha > 60^\circ$ . This distortion is well known in other materials of this type, namely  $\text{GaMo}_4\text{S}_8$ ,  $\text{GaMo}_4\text{Se}_8$  and  $\text{GaV}_4\text{S}_8$  [20] the same expansion occurs in the  $\text{Mo}_4$ -clusters and results in  $\alpha = 60.533(1)^\circ$  for  $\text{GaMo}_4\text{S}_8$ . In contrast, a contraction is observed in  $\text{GaV}_4\text{S}_8$  that results in  $\alpha = 59.66(2)^\circ$  [22]. This can be rationalised by a model of the cluster orbitals, Figure 52. According to Johrendt, the metal centred electrons can occupy six bonding and six antibonding molecular orbitals (MO's) in the cubic phase. The three highest bonding MO's, the  $t_2$ -level, are threefold degenerate with respect to the  $\bar{4}3m$  symmetry of the  $V_4$ -cluster. The elongation of the V-V bond below 33 K removes the degeneracy of the  $t_2$  ( $T_d$ ) MO. The threefold degeneracy is lifted by the splitting of it into a twofold degenerate level with  $e$  symmetry and a single level with  $a_1$  symmetry ( $C_{3v}$ ). The point group of the  $V_4$ -cluster is further reduced to  $C_s$  upon the transformation to  $M\text{-GeV}_4\text{S}_8$  losing the threefold axis. The  $a_1$  orbital is transformed to a level with  $a'$  symmetry. The twofold degeneracy of the  $e$  MO is then lifted by the splitting of it into two levels with  $a'$  and  $a''$  symmetry. In

$C_s$  there is now a possible interaction, which is symmetry-forbidden in the point group  $C_{3v}$ , between the  $a'$  levels.

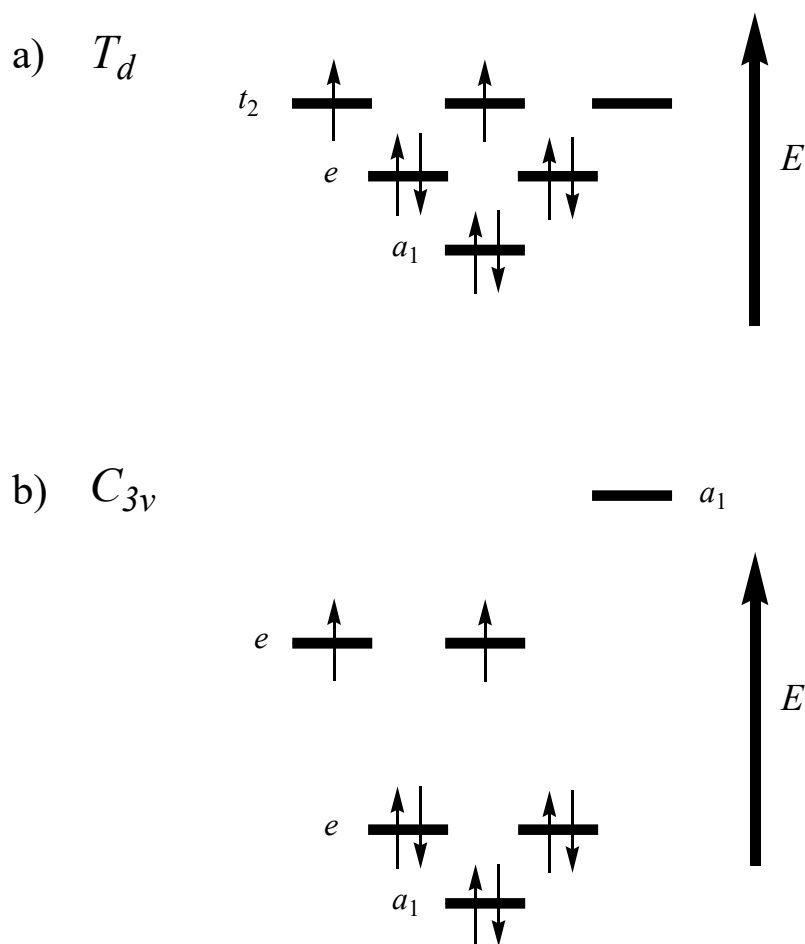


**Figure 52:** Cluster MO scheme for a)  $C\text{-GeV}_4\text{S}_8$  and b)  $R\text{-GeV}_4\text{S}_8$ [23].

The availability of high resolution diffraction data can enable the precise determination of whether a phase transition is complete or not. At 4.2 K, the transition from  $F\bar{4}3m$  to  $R3m$  of  $\text{GaV}_4\text{S}_8$  is almost complete, *ca.* 7% cubic phase remains. However,  $\text{GaMo}_4\text{S}_8$  exhibits an incomplete transition whereby *ca.* 40% remains cubic at this temperature [11]. In contrast to the aforementioned gallium containing spinels, the coexistence of three different polymorphs as a result of two successive reductions in symmetry is observed in  $\text{GeV}_4\text{S}_8$ . Currently there are no published examples of such an occurrence within the defect thiospinel family, though the coexistence of three phases in the copper-oxygen plane of some high- $T_c$  superconductors is known [24].

The onset of series of structural distortions in  $\text{GeV}_4\text{S}_8$  at  $T_S = 32$  K is associated with a change in paramagnetic behaviour observed in the magnetic

susceptibility data. The high temperature paramagnetic moment has been previously calculated over the range  $35 \leq T / \text{K} \leq 295$  to be  $\mu_{\text{eff}} = 2.41(1) \mu_{\text{B}}$ , incorporating a temperature independent term [20]. As the data presented here were unable to be fitted using this function it is possible that this value was appropriate for these data. The effective magnetic moment is then reduced to  $\mu_{\text{eff}} = 1.59(1) \mu_{\text{B}}$ , below  $T_{\text{S}}$ , consistent with the occurrence of magnetic frustration above  $T_{\text{N}}$ . Antiferromagnetic ordering is then associated with a second successive phase transition at  $T_{\text{N}} = 18 \text{ K}$ . At  $T_{\text{N}}$  it is the pronounced lengthening in the  $a$  lattice parameter and an increase in  $\beta$  of  $M\text{-GeV}_4\text{S}_8$  that coincides with the antiferromagnetic ordering of  $\text{GeV}_4\text{S}_8$ . Discontinuities are also observed, at 18 K, in the  $b$  and  $c$  lattice parameters of this phase. A purely monoclinic phase, whereby the cubic and rhombohedral phases are no longer observed, is reached after the onset of antiferromagnetic ordering.

### 3.6 References

- [1] Y. Dong, M.A. McGuire, H. Yun, F.J. DiSalvo, *Journal of Solid State Chemistry* 183 (2010) 606-612.
- [2] J. Krok-Kowalski, J. Warczewski, K. Krajewski, H. Duda, P. Gusin, T. Śliwińska, A. Pacyna, T. Mydlarz, S. Matyjasik, E. Malicka, A. Kita, *Journal of Alloys and Compounds* 430 (2007) 47-53.
- [3] J. Philip, T.R.N. Kutty, *Materials Letters* 39 (1999) 311-317.
- [4] Q.F. Li, L.F. Chen, J.G. Yin, *Physics Letters A* 374 (2010) 1555-1559.
- [5] A. Castets, M. Nauciel-Bloch, *Solid State Communications* 10 (1972) 1121-1125.
- [6] H. BARZ, *Materials Research Bulletin* 8 (1973) 983-988.
- [7] D. Bichler, H. Slavik, D. Johrendt, *Zeitschrift Fur Naturforschung Section B-a Journal of Chemical Sciences* 64 (2009) 915-921.
- [8] J.M. Vandenberg, D. Brasen, *Journal of Solid State Chemistry* 14 (1975) 203-208.
- [9] M. Nauciel-Bloch, A. Castets, R. Plumier, *Physics Letters A* 39 (1972) 311-312.

- [10] M.L.E. Moubtassim, J. Olivier-Fourcade, J. Senegas, J.C. Jumas, *Materials Research Bulletin* 28 (1993) 1083-1092.
- [11] A. Powell, A. McDowall, I. Szkoda, K. Knight, B. Kennedy, T. Vogt, *Chemistry of Materials* 19 (2007) 5035-5044.
- [12] H. Muller, W. Kockelmann, D. Johrendt, *Chemistry of Materials* 18 (2006) 2174-2180.
- [13] H. Chudo, C. Michloka, H. Nakamura, K. Yoshimura, *Physica B-Condensed Matter* 378-80 (2006) 1150-1151.
- [14] D. Bichler, V. Zinth, D. Johrendt, O. Heyer, M. Forthaus, T. Lorenz, M. Abd-Elmeguid, *Physical Review B* 77 (2008) 212102.
- [15] A.C. Larson, R.B. Dreele, Los Alamos National Laboratory Report.
- [16] Y. Sahoo, A.K. Rastogi, *Physica B* 215 (1995) 233-242.
- [17] M. Ruman, A. Rastogi, *Journal of Physics and Chemistry of Solids* 64 (2003) 77-85.
- [18] M. Jeyaratnam, N. Nagar, *Standard Reference Material 1878. Respirable Alpha Quartz*. Office of Standard Reference Materials, Washington, D.C., 1983.
- [19] A. McDowell, *The Preparation and Characterisation of Intercalation Compounds of Molybdenum Sulphide and Related Phases*. Heriot-Watt University, 2003.
- [20] I. Szkoda, P. Vaqueiro, A. McDowall, A. Powell, C. Ritter, *Journal of Solid State Chemistry* 182 (2009) 2806-2814.
- [21] T. Murugesan, S. Ramesh, J. Gopalakrishnan, C. Rao, *Journal of Solid State Chemistry* 44 (1982) 119-125.
- [22] R. Pocha, D. Johrendt, R. Pottgen, *Chemistry of Materials* 12 (2000) 2882-2887.
- [23] D. Johrendt, *Zeitschrift Fur Anorganische Und Allgemeine Chemie* 624 (1998) 952-958.
- [24] G.G. Sergeeva, V.Y. Gonchar, A.V. Voitsenya, *Low Temperature Physics* 27 (2001) 468-472.



## Chapter 4: Structural, Physical and Magnetic Properties of $\text{Cr}_{1-x}\text{In}_x\text{GeTe}_3$

### 4.1 Introduction

The new series of mixed-metal tellurides has been prepared through substitution of chromium with indium in the series  $\text{Cr}_{1-x}\text{In}_x\text{GeTe}_3$  ( $0 \leq x \leq 1$ ) to investigate the effects of diluting the magnetic cation on the structural, physical and magnetic properties. Neutron experiments were completed on POLARIS at ISIS.

### 4.2 Background

There is an interesting group of materials whose structure is made up of slabs of edge-sharing octahedra, centred by transition-metal ions and *pairs* of main-group ions, Figure 53.  $\text{CrXY}_3$ , where  $X = \text{Si}, \text{Ge}$ , and  $Y = \text{Se}, \text{Te}$ , show obvious similarities to the  $\text{MPS}_3$ -type structure; consisting of a hexagonal close packed arrangement of tellurium atoms where the octahedral sites are fully occupied in an ordered manner every other layer, analogous to  $\text{CdCl}_2$ .

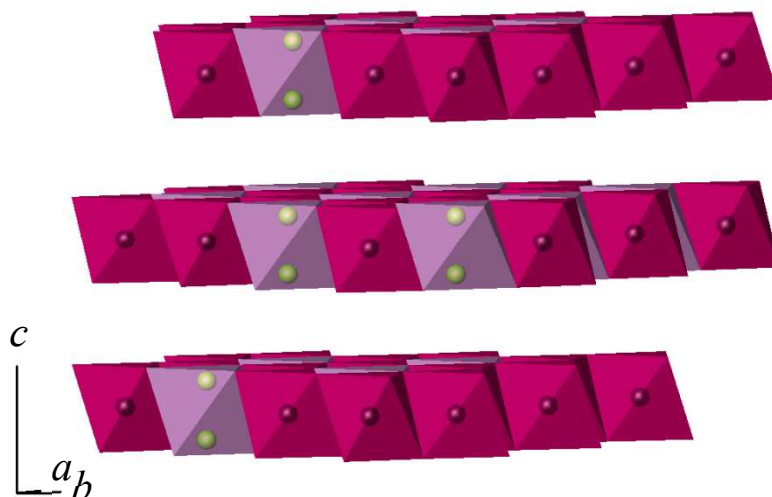


**Figure 53:** The three-layer structure of  $\text{CrGeTe}_3$ . Pink polyhedra represent  $\text{CrTe}_6$  units; grey polyhedral represent  $\text{Ge}_2\text{Te}_6$  units.[1]

Throughout the occupied layer, 2/3 of the octahedra are centred with a transition-metals ion, the remaining 1/3 with a X<sub>2</sub> pair. [1, 2] Amongst chalcogenides this paired species centering an octahedra is unusual; Si<sub>2</sub>Te<sub>3</sub>, K<sub>6</sub>Si<sub>2</sub>Te<sub>6</sub>, Mn<sub>3</sub>Si<sub>2</sub>Te<sub>6</sub> and Tl<sub>6</sub>Si<sub>2</sub>Te<sub>6</sub> with an Si<sub>2</sub> unit; Na<sub>8</sub>Ge<sub>4</sub>Se<sub>10</sub>, Na<sub>6</sub>Ge<sub>2</sub>Se<sub>6</sub>, K<sub>6</sub>Ge<sub>2</sub>Te<sub>6</sub> with a Ge<sub>2</sub> pair. [3, 4] The van der Waals' gap could be tuned to fabricate devices with channels that are extremely thin for applications in field-effect transistors. [5]

With this in mind, CrGeTe<sub>3</sub> was synthesised. The magnetic structure and properties of CrGeTe<sub>3</sub> had been determined by neutron powder diffraction and susceptibility and magnetisation measurements made. Below 61 K, CrGeTe<sub>3</sub> is ferromagnetic with spins aligned along the *c* axis of the cell. The resistivity at room temperature was reported to be,  $\rho = 0.02 \text{ } \Omega\text{cm}$ , advantageous for thermoelectric applications.

Initial physical property measurements were made to assess whether or not these materials could be utilised in thermoelectric applications. The Seebeck coefficient was measured,  $S = 468 \text{ } \mu\text{VK}^{-1}$  at 324 K and the thermal conductivity,  $\kappa = 0.72 \text{ Wm}^{-1}\text{K}^{-1}$  at 373 K. This supported the suggestion that low dimensional structures are potentially technologically useful thermoelectric materials. However contrary to the original report, the measured electrical resistivity of CrGeTe<sub>3</sub> was relatively high, 82  $\Omega\text{cm}$ , and required reducing to improve the thermoelectric efficiency. With a view to controlling the charge carrier density and reducing this resistivity, chemical substitution at the cationic sites was made with indium.

### 4.3 Synthesis

The series Cr<sub>1-x</sub>In<sub>x</sub>GeTe<sub>3</sub> ( $0 \leq x \leq 1$ ) was synthesized by high-temperature solid-state reaction. Stoichiometric amounts of high-purity, chromium, indium, germanium, and tellurium were loaded into a silica tube. The silica tubes were evacuated to  $\leq 10^{-4}$  Torr and sealed. Samples were fired at 773 K for 24 hours then ramped to between 973 K and 1273 K depending on the value of *x*. Samples were typically fired three times, each for a four day period with intermittent re-grinding to ensure maximum homogeneity. Reaction mixtures were inserted into a room temperature furnace and upon completion

of the heating period were cooled at varying ramp rates depending on the sample. A summary of the required conditions is given in Table 18. The progress of the reaction was followed by powder X-ray diffraction. Powder X-ray diffraction data were collected using a D8 Advance Bruker diffractometer fitted with a Bruker LynxEye linear detector, see section Powder X-ray Diffraction. Data were collected over the angular range  $10 \leq 2\theta/\circ \leq 120$  counting for 5 seconds at each  $0.02^\circ$  step. Resistivity and thermal conductivity measurements were made using the details given in Physical Property Studies.  $\text{Cr}_{1-x}\text{In}_x\text{GeTe}_3$  forms a selection of fine, loose, dark grey powders.

**Table 18:** Reaction conditions for  $\text{Cr}_{1-x}\text{In}_x\text{GeTe}_3$ .

$x$ in $\text{Cr}_x\text{In}_{1-x}\text{GeTe}_3$	1 <sup>st</sup> Firing	2 <sup>nd</sup> Firing	3 <sup>rd</sup> Firing	4 <sup>th</sup> Firing
1	300°C 1 day, 900°C 4 days, slow cool @ 0.1°C/min	Into furnace at 400°C 2 days, slow cool @ 0.1°C/min	400°C 5 days, slow cool @ 0.1°C/min	-
0.9	300°C 2 days, 900°C 4 days, slow cool @ 0.1°C/min	400°C 4 days, slow cool @ 0.1°C/min	-	-
0.8	300°C 2 days, 900°C 4 days, slow cool @ 0.1°C/min	400°C 4 days, slow cool @ 0.1°C/min	400°C 3 days, slow cool @ 0.1°C/min	-
0.5	400°C 2 days, 1000°C 4 days, slow cool @ 0.1°C/min	500°C 1 week 1°C/min ramp rate heating and cooling	-	-
0.4	300°C 1 day, 900°C 4 days, slow cool @ 0.1°C/min	400°C 3 days, slow cool @ 0.1°C/min	400°C 6 days, slow cool @ 0.1°C/min	-
0.3	400°C 1 day, 700°C 3 days	400°C 4 days	Pressed pellets, 400°C 5 days	Pressed pellets, 400°C 4 days
0.2	400°C 1 day, 700°C 3 days	400°C 4 days	400°C 5 days	Pressed pellets, 400°C 4 days
0.1	400°C 2 days, 700°C 5 days	400°C 4 days	Pressed pellets, 400°C 4 days	-
0	400°C 1 day, 700°C 4 days, slow cool @ 2°C/min	400°C 12 days	Pressed pellets, 400°C 5 days	-

## 4.4 Results

### 4.4.1 Structural Studies on $\text{Cr}_{1-x}\text{In}_x\text{GeTe}_3$ at Room Temperature

The end-member phase,  $\text{CrGeTe}_3$ , crystallises in space group  $R\bar{3}$  with a three-layer repeating unit, Figure 53 [1]. It consists of hexagonally close packed layers of  $\text{Te}^{2-}$  ions, with  $\text{Cr}^{3+}$  ions and  $(\text{Ge}_2)^{6+}$  dumbbell pairs occupying octahedral holes in every other layer and providing a van der Waals' gap.

X-ray and neutron diffraction data were refined using the Rietveld method in the GSAS program [6]. Refinements of  $\text{CrGeTe}_3$  X-ray data were initiated using lattice parameters from a TOPAS refinement and the previously determined structural model for  $\text{CrGeTe}_3$ . Backgrounds of the X-ray data were modelled using a reciprocal interpolation function; the peak shape was described using Simpson's rule integration of a pseudovoigt function. Background coefficients during neutron data analysis were modelled using an expansion of the exponential function, Equation (39), with the peak shape being described using a convolution of two back-to-back exponentials together with a pseudo-Voigt function to account for the Lorentzian broadening.

Rietveld analysis commenced with the refinement of the scale factors, background coefficients and zero point where appropriate. Lattice parameters were then introduced, followed by atomic coordinates and thermal parameters. The thermal parameters in X-ray diffraction data for the parent phase were constrained to be equal across all cationic and anionic sites, however for  $x = 0.5, 0.6$  and all neutron data these were refined parameters, with constraints applied on individual mixed metal sites for the values to be equal. Finally the peak shape was optimised. For neutron refinements, regions centred at  $d = 2.1\text{-}2.2, 1.5\text{-}1.6$  and  $1.2\text{-}1.3$  Å were excluded in the Rietveld analysis due to the presence of reflections, [110], [200] and [211] respectively, originating from vanadium, of which the sample can was fabricated.

All materials were initially investigated using laboratory powder X-ray diffraction at room temperature. These data show that the substructure

persists for  $0 \leq x \leq 1$ , Figure 54, however  $x = 0.5$  shows a different superstructure.

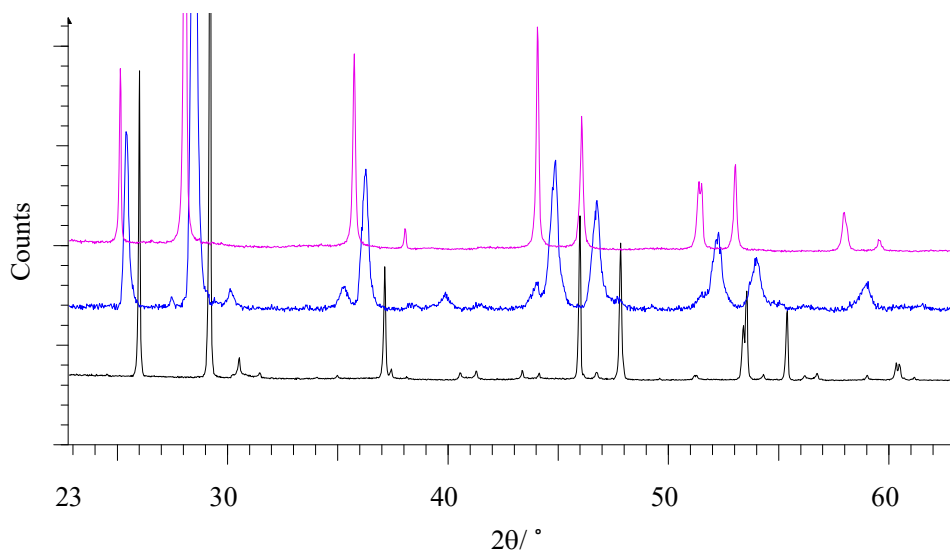


**Figure 54:** Room temperature X-ray diffraction data for  $\text{CrGeTe}_3$  (black line),  $\text{Cr}_{0.5}\text{In}_{0.5}\text{GeTe}_3$  (blue line) and  $\text{InGeTe}_3$  (pink line).

Using TOPAS[7], an initial unit cell parameter refinement of  $\text{Cr}_{1-x}\text{In}_x\text{GeTe}_3$  in  $R\bar{3}$ , show that as  $x$  increases, the unit cell increases in both the  $a$  and  $c$  lattice parameter, Figure 55.

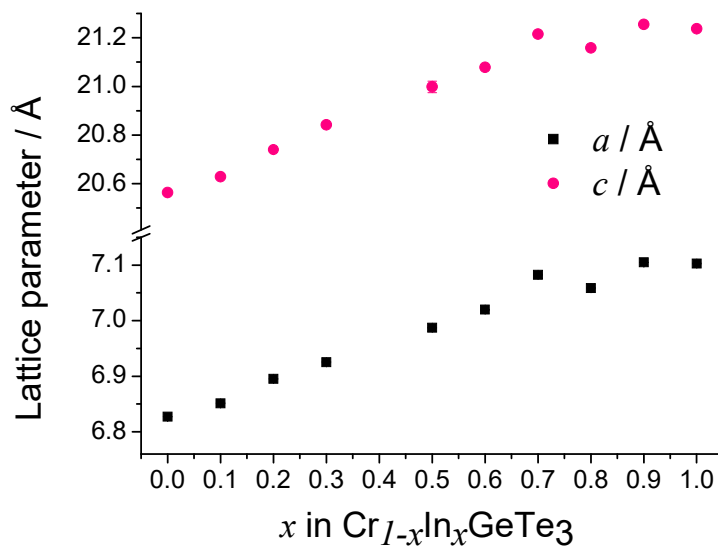


**Figure 55:** Lattice parameters as a function of indium substitution in  $\text{Cr}_{1-x}\text{In}_x\text{GeTe}_3$  ( $0 \leq x \leq 1$ ) determined by TOPAS analysis in space group  $R\bar{3}$ .

Error bars are shown.

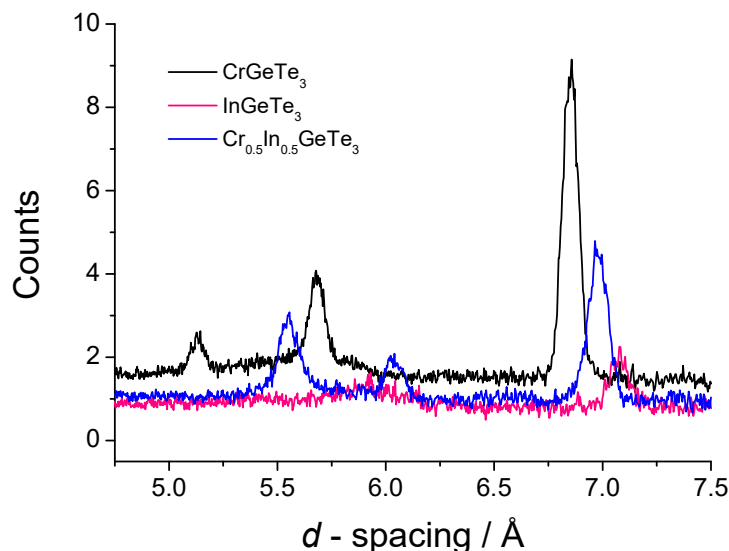


**Figure 56:** POLARIS neutron diffraction data showing the differences in superlattice peaks and  $[00l]$  reflections between  $\text{CrGeTe}_3$  (black),  $\text{InGeTe}_3$  (pink) and  $\text{Cr}_{0.5}\text{In}_{0.5}\text{GeTe}_3$  (blue) in the  $4.75 \leq d / \text{\AA} \leq 7.5$  region.

Room temperature neutron diffraction experiments, however, emphasise three very different superstructures across the compositional range. Neutron diffraction data was utilised to determine this changing cationic ordering across the series. Data were collected on the POLARIS diffractometer and are shown in Figure 56. These data show the shifting  $[00l]$  reflections, centred  $\sim 7 \text{\AA}$ , and the changes in observed superlattice peaks between  $5 \leq d / \text{\AA} \leq 6.25$ . A three-layer repeating unit in the  $c$ -axis has a  $[003]$  reflection centred at  $\sim 7 \text{\AA}$ , however this structure only persists to  $x = 0.1$ , below which indium ions induce a change in the stacking sequence of the metal-telluride slabs. At  $x = 0.1$ , the incorporation of indium does result in a two phase mixture of the substituted phases, Table 21. Within the range  $0.2 \leq x \leq 0.6$ , the reflection centred at  $\sim 7 \text{\AA}$ , becomes the  $[002]$ . This structure is currently best described in space group  $P\bar{3}1c$  with the same two-dimensional ordering of  $\text{Cr}^{3+} / \text{In}^{3+}$  ions and  $(\text{Ge}_2)^{6+}$  pairs as in  $R\bar{3}$  but with a two-layer repeat along the  $[00l]$  plane, Figure 57. From the Rietveld refinements there are some discrepancies with inadequately modelled peak shape; these were originally attributed to preferred orientation however further investigation is required in order to fully elucidate the structure.

An initial model for  $\text{Cr}_{0.5}\text{In}_{0.5}\text{GeTe}_3$  in  $P\bar{3}1c$  was derived from the trigonal  $\text{Cr}_2\text{S}_3$  structure. A layered array is achieved when all the  $2(c)$  sites are unoccupied.



**Figure 57:** The two-layer structure of  $\text{Cr}_{0.5}\text{In}_{0.5}\text{GeTe}_3$ .

At higher levels of indium substitution ( $x \geq 0.7$ ) the superlattice peaks become weak and diffuse.  $\text{InGeTe}_3$  potentially crystallises in centrosymmetric space group  $P6_3/mmc$ . The Two-dimensional cationic ordering doubles the primitive  $a$  lattice parameter, whilst in three-dimensions, a three layer repeat is observed. Table 19 provides a summary of the unit cell data across the series. For direct comparison across the series, Figure 58 shows the primitive lattice parameters as a function of indium substitution.

A plethora of different models were utilised in order to determine the atomic structure of  $\text{InGeTe}_3$  however this proved unsuccessful.  $P6_3/mmc$  provided a suitable starting point, however in the backscattering bank, Figure 64 c), it becomes apparent that there is some peak broadening that cannot merely be attributed to the peak shape; further investigation could liberate what these anomalies are.



**Table 19:** Unit cell data for  $\text{Cr}_{1-x}\text{In}_x\text{GeTe}_3$  ( $0 \leq x \leq 1$ ).

$x$ in $\text{Cr}_{1-x}\text{In}_x\text{GeTe}_3$	0, 0.1	0.2, 0.5, 0.6	0.7, 0.8, 0.9, 1
Hermann-Mauguin Symbol	$R\bar{3}$	$P\bar{3}1c$	$P6_3/mmc$
Space Group Number	148	163	194
$a$ primitive	$\sqrt{3}a$	$\sqrt{3}a$	$2a$
$c$ primitive	$3c$	$2c$	$3c$

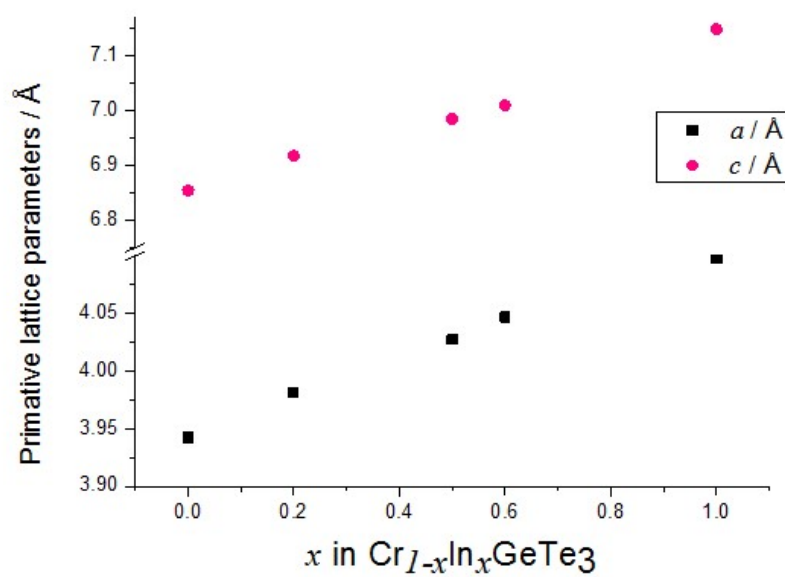


**Figure 58:** Primitive lattice parameters as a function of indium substitution as determined by Rietveld refinement.

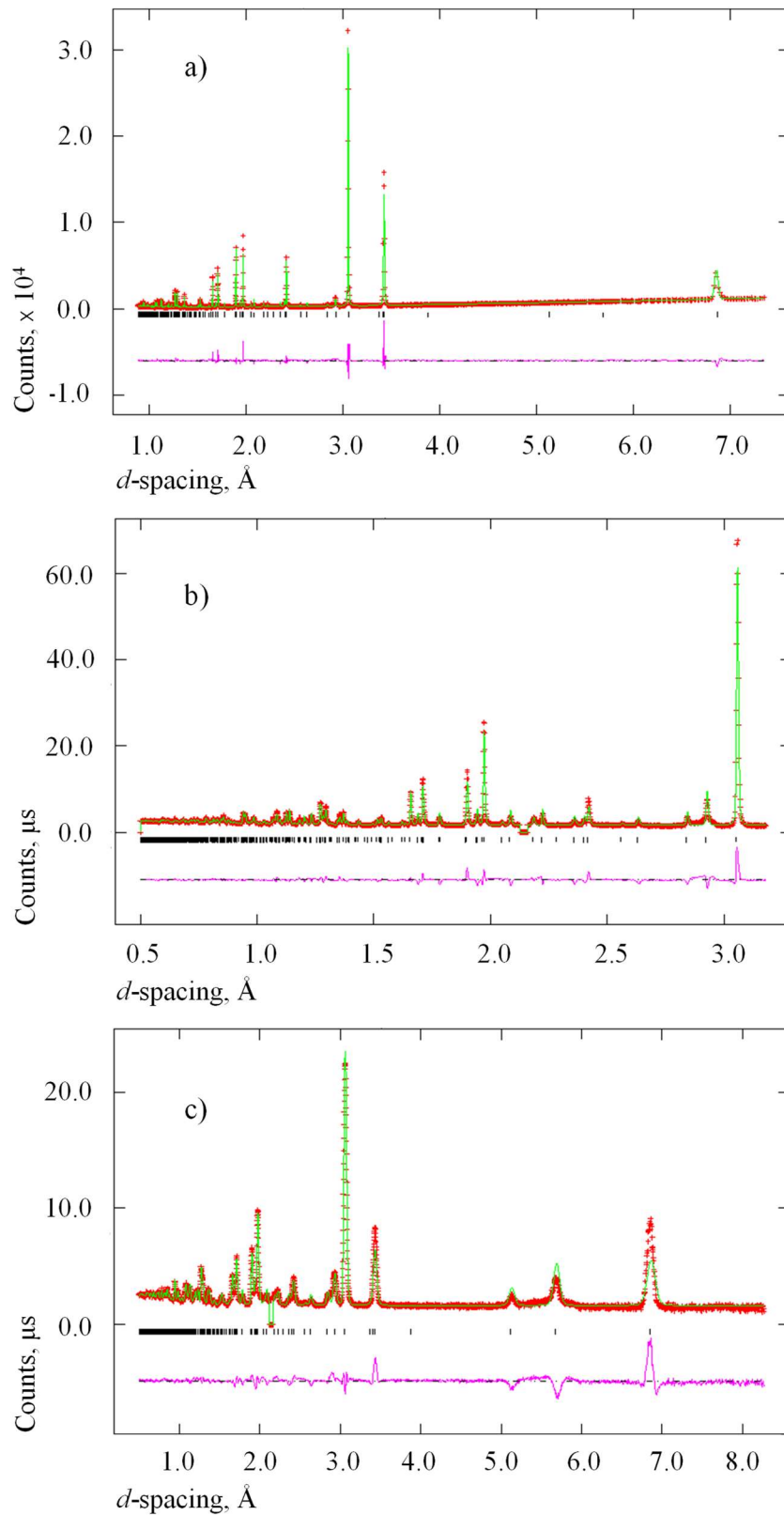


**Figure 59:** Final observed (crosses), calculated (upper full line) and difference (lower full line) X-ray and neutron diffraction profiles for CrGeTe<sub>3</sub> at room temperature. a) X-ray; b) Neutron, backscattering bank,  $2\theta = 145^\circ$ ; c) Neutron, low angle bank,  $2\theta = 35^\circ$ .

Reflection positions are marked.

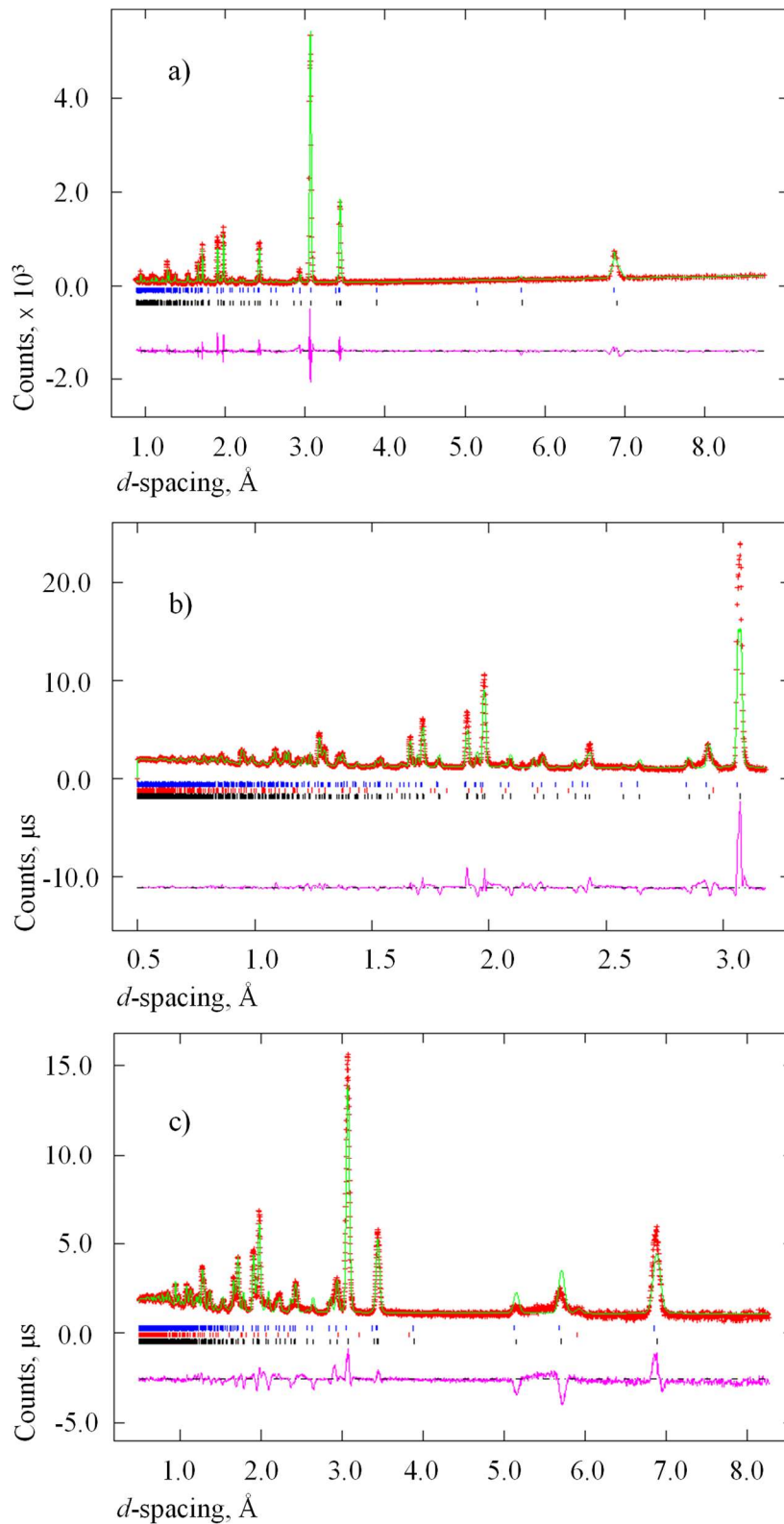


**Figure 60:** Final observed (crosses), calculated (upper full line) and difference (lower full line) X-ray and neutron diffraction profiles for  $\text{Cr}_{0.9}\text{In}_{0.1}\text{GeTe}_3$  at room temperature. a) X-ray; b) Neutron, backscattering bank,  $2\theta = 145^\circ$ ; c) Neutron, low angle bank,  $2\theta = 35^\circ$ . Reflection positions are marked; black,  $\text{CrGeTe}_3$ ; blue,  $\text{Cr}_{0.9}\text{In}_{0.1}\text{GeTe}_3$ ; red, Te.

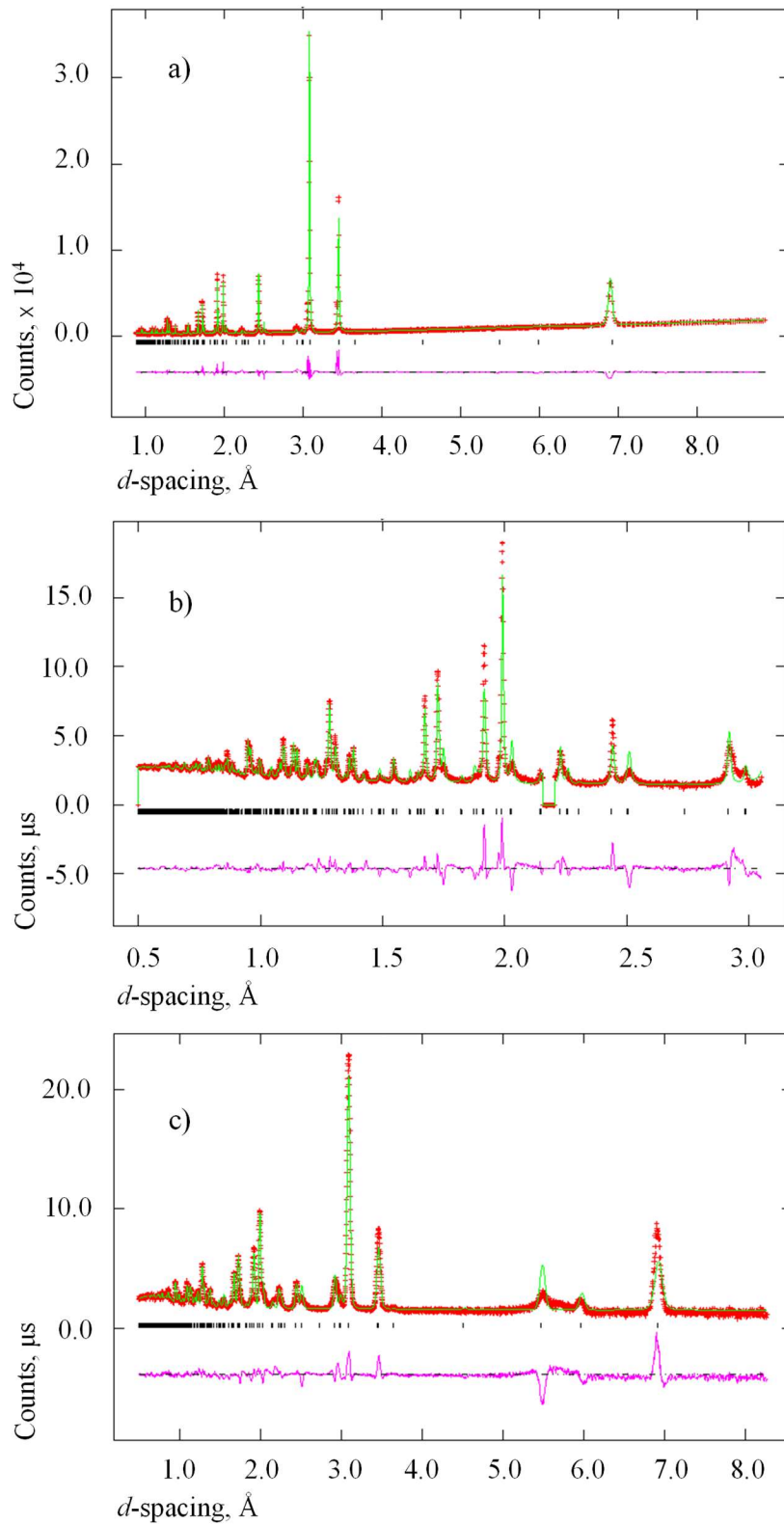


**Figure 61:** Final observed (crosses), calculated (upper full line) and difference (lower full line) X-ray and neutron diffraction profiles for  $\text{Cr}_{0.8}\text{In}_{0.2}\text{GeTe}_3$  at room temperature. a) X-ray; b) Neutron, backscattering bank,  $2\theta = 145^\circ$ ; c) Neutron, low angle bank,  $2\theta = 35^\circ$ .

Reflection positions are marked.

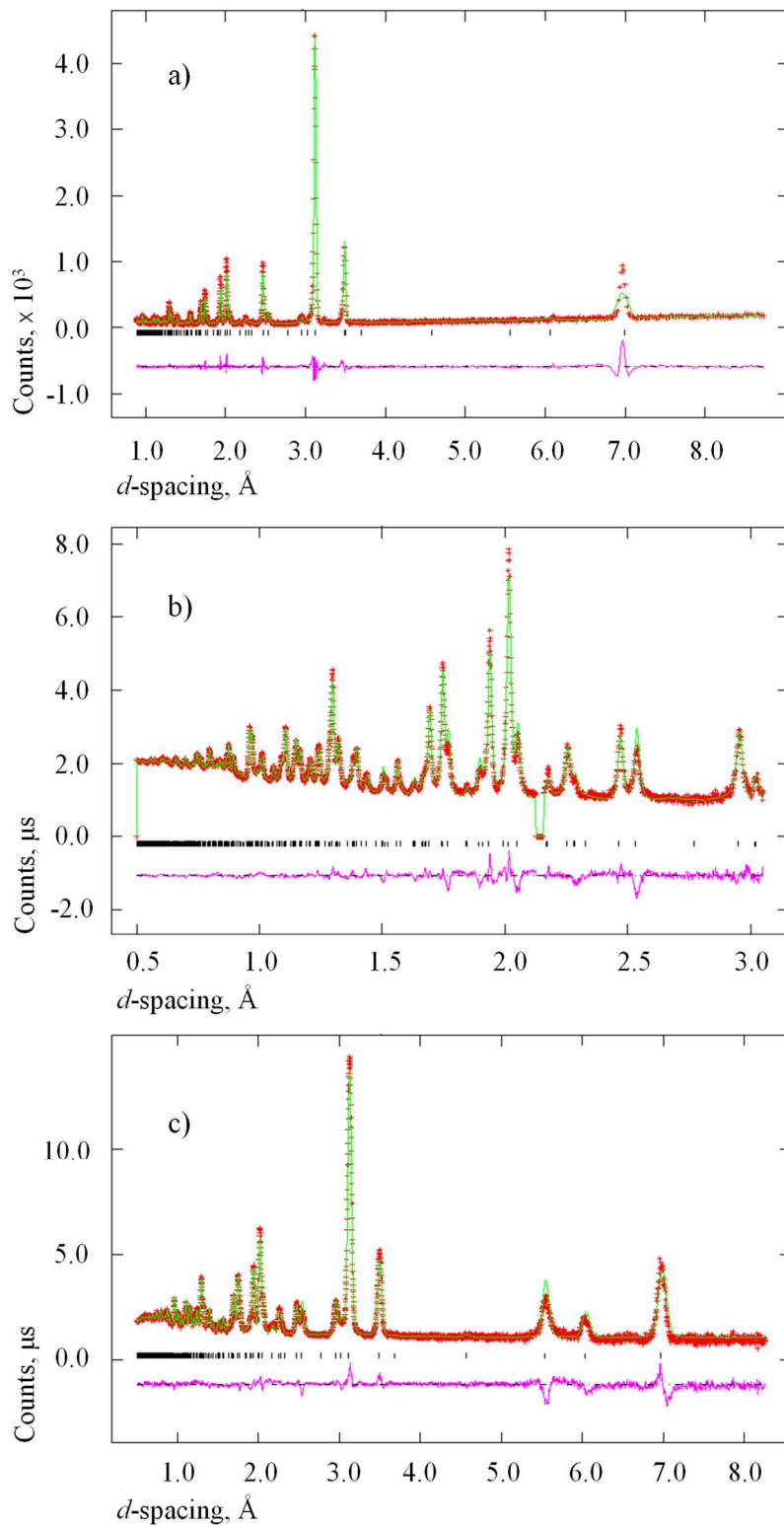


**Figure 62:** Final observed (crosses), calculated (upper full line) and difference (lower full line) X-ray and neutron diffraction profiles for  $\text{Cr}_{0.5}\text{In}_{0.5}\text{GeTe}_3$  at room temperature. a) X-ray; b) Neutron, backscattering bank,  $2\theta = 145^\circ$ ; c) Neutron, low angle bank,  $2\theta = 35^\circ$ .

Reflection positions are marked.

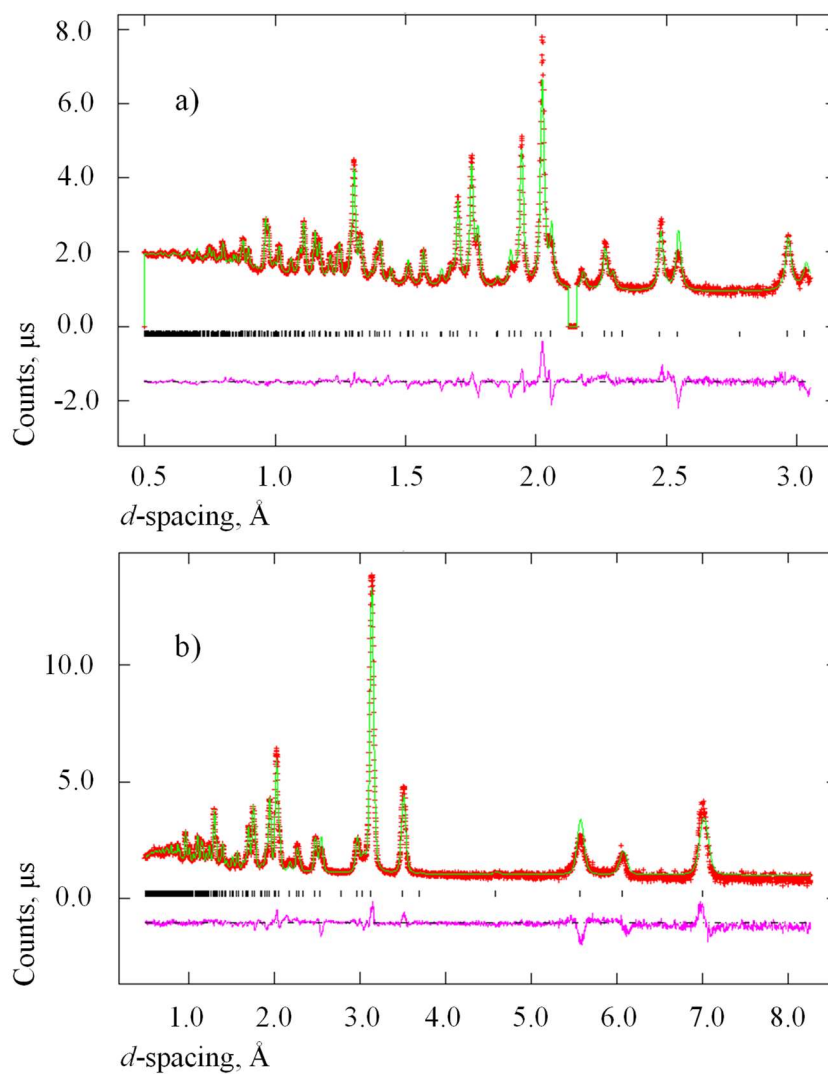


**Figure 63:** Final observed (crosses), calculated (upper full line) and difference (lower full line) neutron diffraction profiles, for  $\text{Cr}_{0.4}\text{In}_{0.6}\text{GeTe}_3$  at room temperature. a) Neutron, backscattering bank,  $2\theta = 145^\circ$ ; b) Neutron, low angle bank,  $2\theta = 35^\circ$ . Reflection positions are marked.

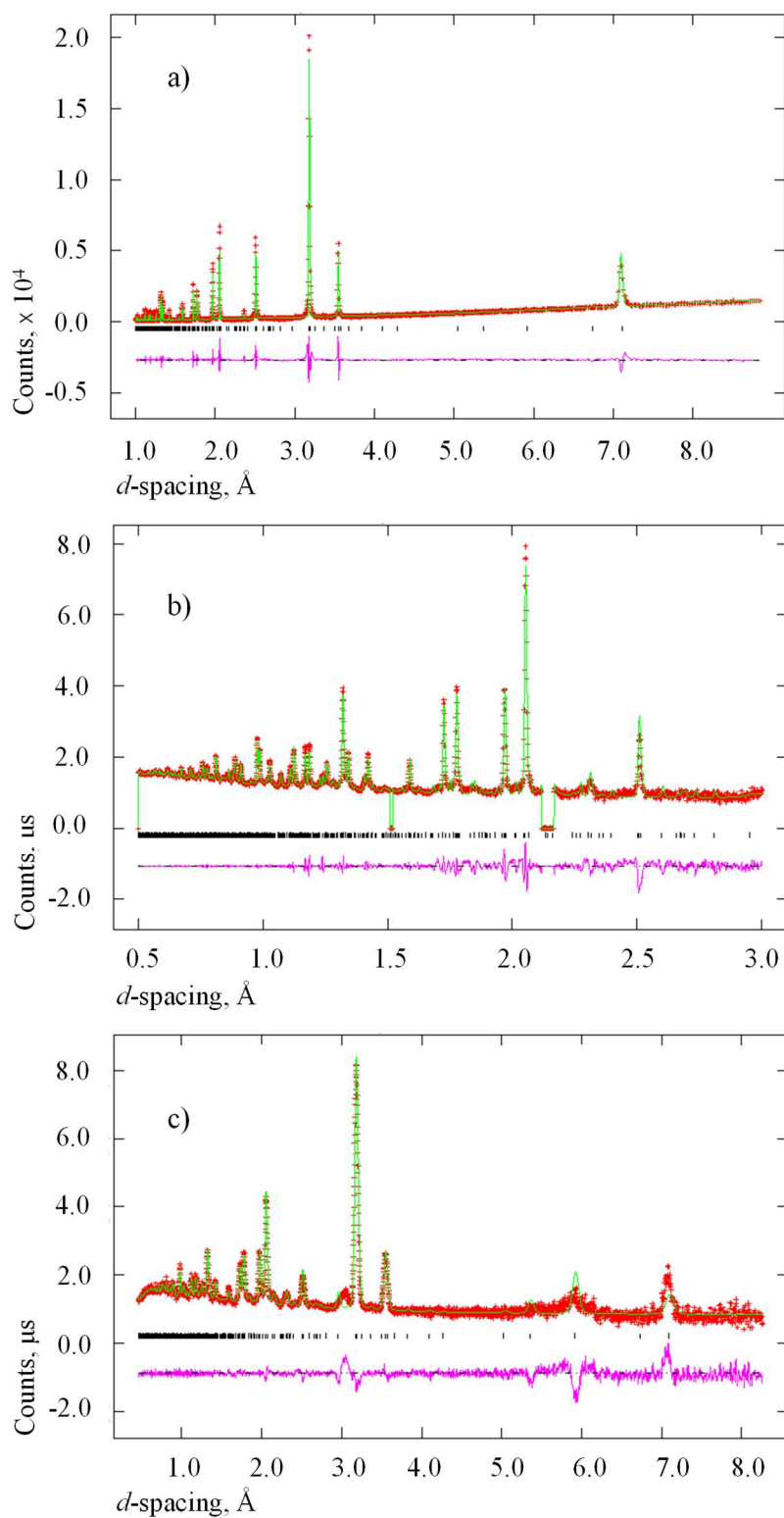


**Figure 64:** Final observed (crosses), calculated (upper full line) and difference (lower full line) X-ray and neutron diffraction profiles, using le Bail refinement, for InGeTe<sub>3</sub> at room temperature. a) X-ray; b) Neutron, backscattering bank,  $2\theta = 145^\circ$ ; c) Neutron, low angle bank,  $2\theta = 35^\circ$ .

Reflection positions are marked.

**Table 20:** Final refined parameters for CrGeTe<sub>3</sub> in space group  $R\bar{3}$  at room temperature.

Source		X-ray	Neutron
$a / \text{\AA}$		6.82821(20)	6.82711(15)
$c / \text{\AA}$		20.56214(67)	20.5664(31)
$V / \text{\AA}^3$		830.256(63)	830.16(13)
Cr <sup>a</sup>	<i>Site</i>	6( <i>c</i> )	
	<i>Z</i>	0.33412(51)	0.33407(27)
	<i>B</i>	0.67981(54)	1.46385(77)
Ge <sup>a</sup>	<i>Site</i>	6( <i>c</i> )	
	<i>Z</i>	0.05857(32)	0.058387(98)
	<i>B</i>	0.67981(54)	1.33831(47)
Te	<i>Site</i>	18 ( <i>f</i> )	
	<i>X</i>	0.66608(65)	0.66792(28)
	<i>Y</i>	-0.02409(42)	-0.02929(18)
	<i>Z</i>	0.24792(17)	0.249532(99)
	<i>B</i>	0.67981(54)	0.35135(24)
R <sub>wp</sub> / % Backscattering bank: 2θ = 145°			4.44
R <sub>wp</sub> / % Low angle bank: 2θ = 35°			7.06
R <sub>wp</sub> / %		18.1	4.79
$\chi^2$		12.75	14.69

---

<sup>a</sup> 6(*c*) site is a special position at  $0\ 0\ z$



**Table 21:** Final refined neutron data parameters for  $\text{Cr}_{0.9}\text{In}_{0.1}\text{GeTe}_3$  in space group  $R\bar{3}$  at room temperature.

Phase	$\text{Cr}_{0.9}\text{In}_{0.1}\text{GeTe}_3$	$\text{CrGeTe}_3$
$a / \text{\AA}$	6.86556(34)	6.83777(26)
$c / \text{\AA}$	20.6696(17)	20.5820(18)
$V / \text{\AA}^3$	843.753(77)	833.390(74)
% $\text{Cr}_{0.9}\text{In}_{0.1}\text{GeTe}_3$	49.6	
% $\text{CrGeTe}_3$	48.93(6)	
% Te	1.50(1)	
Atomic coordinates for $\text{Cr}_{0.9}\text{In}_{0.1}\text{GeTe}_3$		
$\text{Cr}^a$	Site	6( <i>c</i> )
	<i>Z</i>	0.3360
	<i>B</i>	1.888(1)
$\text{In}^a$	Site	6( <i>c</i> )
	<i>Z</i>	0.3360
	<i>B</i>	1.888(1)
$\text{Ge}^a$	Site	6( <i>c</i> )
	<i>Z</i>	0.0581
	<i>B</i>	1.4118(8)
Te	Site	18 ( <i>f</i> )
	<i>x</i>	0.6673
	<i>y</i>	-0.0312
	<i>z</i>	0.2488
	<i>B</i>	1.888(1)
$R_{\text{wp}} / \%$ Backscattering bank: $2\theta = 145^\circ$	4.76	
$R_{\text{wp}} / \%$ Low angle bank: $2\theta = 35^\circ$	9.68	
$R_{\text{wp}} / \%$	5.5	
$\chi^2$	12.54	

---

<sup>a</sup> 6(*c*) site is a special position at  $0\ 0\ z$

**Table 22:** Final refined parameters for  $\text{Cr}_{0.8}\text{In}_{0.2}\text{GeTe}_3$  in space group  $P\bar{3}1c$  at room temperature.

Source		X-ray	Neutron
$a / \text{\AA}$		6.90148(26)	6.89514(15)
$c / \text{\AA}$		13.8407(13)	13.83415(74)
$V / \text{\AA}^3$		570.92(13)	569.600(27)
Cr	$site^a$	2( $a$ )	
	$B$	1.34068(77)	2.6537(29)
	$SOF$	0.8	
In	$site^a$	2( $a$ )	
	$B$	1.34068(77)	2.6537(29)
	$SOF$	0.2	
Cr	$site^b$	2( $d$ )	
	$B$	1.34068(77)	6.3465(45)
	$SOF$	0.8	
In	$site^b$	2( $d$ )	
	$B$	1.34068(77)	6.3465(45)
	$SOF$	0.2	
Ge	$site$	4( $f$ )	
	$z$	0.16749(45)	0.16464(20)
	$B$	1.34068(77)	3.7283(11)
Te	$site$	12( $i$ )	
	$x$	0.33924(97)	0.33789(44)
	$y$	0.01627(58)	0.02626(26)
	$z$	0.37921(25)	0.37450(22)
	$B$	1.34068(77)	1.23015(44)
$R_{wp} / \%$ Backscattering bank: $2\theta = 145^\circ$			4.81
$R_{wp} / \%$ Low angle bank: $2\theta = 35^\circ$			9.00
$R_{wp} / \%$		12.69	5.43
$\chi^2$		10.46	14.81

<sup>a</sup> 2( $a$ ) site is a special position at  $0\ 0\ \frac{1}{4}$

<sup>b</sup> 2( $d$ ) site is a special position at  $\frac{2}{3}\ \frac{1}{3}\ \frac{1}{4}$

**Table 23:** Final refined parameters for  $\text{Cr}_{0.5}\text{In}_{0.5}\text{GeTe}_3$  in space group  $P\bar{3}1c$  at room temperature.

Source		X-ray	Neutron
$a / \text{\AA}$		6.98675(23)	6.97532(14)
$c / \text{\AA}$		13.98487(74)	13.96894(50)
$V / \text{\AA}^3$		591.206(32)	588.602(18)
Cr	$site^a$	2( $a$ )	
	$B$	0.0473(42)	1.3327(12)
	$SOF$	0.5	
In	$site^a$	2( $a$ )	
	$B$	0.0473(42)	1.3327(12)
	$SOF$	0.5	
Cr	$site^b$	2( $d$ )	
	$B$	3.5672(50)	1.7733(10)
	$SOF$	0.5	
In	$site^b$	2( $d$ )	
	$B$	3.5672(50)	1.7733(10)
	$SOF$	0.5	
Ge	$site$	4( $f$ )	
	$z$	0.16534(54)	0.165247(84)
	$B$	1.7015(38)	1.16146(34)
Te	$site$	12( $i$ )	
	$x$	0.34270(85)	0.34303(26)
	$y$	0.02597(45)	0.02652(18)
	$z$	0.38087(23)	0.37900(11)
	$B$	0.45242(62)	0.95143(27)
$R_{wp} / \%$ Backscattering bank: $2\theta = 145^\circ$			1.93
$R_{wp} / \%$ Low angle bank: $2\theta = 35^\circ$			5.34
$R_{wp} / \%$		12.75	2.53
$\chi^2$		2.12	2.64

<sup>a</sup> 2( $a$ ) site is a special position at  $0\ 0\ \frac{1}{4}$

<sup>b</sup> 2( $d$ ) site is a special position at  $\frac{2}{3}\ \frac{1}{3}\ \frac{1}{4}$

**Table 24:** Final refined parameters for  $\text{Cr}_{0.4}\text{In}_{0.6}\text{GeTe}_3$  in space group  $P\bar{3}1c$  at room temperature.

Source		Neutron
$a / \text{\AA}$		7.00908(16)
$c / \text{\AA}$		14.01836(57)
$V / \text{\AA}^3$		596.417(21)
Cr(1)	$site^a$	2( $a$ )
	$B$	2.12472(16)
	$SOF$	0.4
In(1)	$site^a$	2( $a$ )
	$B$	2.12472(16)
	$SOF$	0.6
Cr(2)	$site^b$	2( $d$ )
	$B$	2.5289(13)
	$SOF$	0.4
In(2)	$site^b$	2( $d$ )
	$B$	2.5289(13)
	$SOF$	0.6
Ge	$site$	4( $f$ )
	$Z$	0.165885(93)
	$B$	1.86732(45)
Te	$site$	12( $i$ )
	$x$	0.34258(30)
	$y$	0.02439(2)
	$z$	0.37945(12)
	$B$	1.32252(31)
$R_{wp} / \%$ Backscattering bank: $2\theta = 145^\circ$		2.25
$R_{wp} / \%$ Low angle bank: $2\theta = 35^\circ$		5.6
$R_{wp} / \%$		2.83
$\chi^2$		3.54

<sup>a</sup> 2( $a$ ) site is a special position at  $0\ 0\ \frac{1}{4}$

<sup>b</sup> 2( $d$ ) site is a special position at  $\frac{2}{3}\ \frac{1}{3}\ \frac{1}{4}$

**Table 25:** Final le Bail refined parameters for  $\text{InGeTe}_3$  in space group  $P6_3/mmc$  at room temperature.

Source	X-ray	Neutron
$a / \text{\AA}$	8.19521(18)	8.1945(11)
$c / \text{\AA}$	21.45519(72)	21.44435(44)
$V / \text{\AA}^3$	1247.911(49)	1247.064(28)
$R_{\text{wp}} / \%$ Backscattering bank: $2\theta = 145^\circ$		2.12
$R_{\text{wp}} / \%$ Low angle bank: $2\theta = 35^\circ$		5.63
Total $R_{\text{wp}} / \%$	18.1	2.74
$\chi^2$	12.75	1.79

**Table 26:** Bond lengths and bond angles extracted from neutron data for  $\text{Cr}_{1-x}\text{In}_x\text{GeTe}_3$ ,  $x = 0$ .

CrGeTe <sub>3</sub>		
Space Group	$R\bar{3}$	
Bond lengths / $\text{\AA}$	Ge-Ge	2.402(4)
	Ge-Te	$2.5345(10) \times 3$
	Te-Cr	2.784(4)
	Te-Cr	2.775(4)
	Te-Ge	2.5345(10)
	Cr-Te	$2.784(4) \times 3$
	Cr-Te	$2.775(4) \times 3$
Bond angles / $^\circ$	Te-Cr-Te	$85.11(15) \times 3$
	Te-Cr-Te	$89.69(5) \times 3$
	Te-Cr-Te	$172.673(35) \times 3$
	Te-Cr-Te	$99.61(5) \times 3$
	Te-Cr-Te	$86.09(14) \times 3$
	Cr-Te-Cr	90.31(5)
	Cr-Te-Ge	101.62(7)
	Cr-Te-Ge	101.54(7)

**Table 27:** Bond lengths and bond angles extracted from neutron data for series  $\text{Cr}_{1-x}\text{In}_x\text{GeTe}_3$ ,  $x = 0.2, 0.5, 0.6$ , where M applies to both chromium and indium.

$x$ in $\text{Cr}_{1-x}\text{In}_x\text{GeTe}_3$ ( $0 \leq x \leq 1$ )	0.2	0.5	0.6
Space Group	$P\bar{3}1c$		
Ge-Ge	2.362(6)	2.3678(23)	2.3583(26)
Ge-Te	2.5227(16) $\times 3$	2.5529(12) $\times 3$	2.5558(13) $\times 3$
Te-M(1)	2.8293(27)	2.9264(15)	2.9457(17)
Te-M(2)	2.7908(27)	2.8447(15)	2.8676(17)
Te-Ge	2.5227(16)	2.5529(12)	2.5558(13)
M(1)-Te	2.8293(27) $\times 6$	2.9264(15) $\times 6$	2.9457(17) $\times 6$
M(2)-Te	2.7908(27) $\times 6$	2.8447(15) $\times 6$	2.8676(17) $\times 6$
Te-M(1)-Te	86.80(9) $\times 6$	86.06(5) $\times 6$	86.03(5) $\times 6$
Te-M(1)-Te	97.75(8) $\times 3$	98.41(5) $\times 3$	98.06(5) $\times 3$
Te-M(1)-Te	89.02(11) $\times 3$	89.84(6) $\times 3$	90.19(6) $\times 3$
Te-M(1)-Te	173.65(6) $\times 3$	173.72(4) $\times 3$	174.24(5) $\times 3$
Te-M(2)-Te	85.91(8) $\times 6$	84.15(4) $\times 6$	84.22(5) $\times 6$
Te-M(2)-Te	174.68(8) $\times 3$	175.91(6) $\times 3$	176.33(6) $\times 3$
Te-M(2)-Te	90.59(11) $\times 3$	93.17(6) $\times 3$	93.37(7) $\times 3$
Te-M(2)-Te	97.85(8) $\times 3$	98.68(5) $\times 3$	98.32(5) $\times 3$
M(1)-Te-M(2)	90.20(8) $\times 2$	88.49(4) $\times 2$	88.22(4)
M(1)-Te-Ge	101.61(10)	99.78(4)	99.78(5)
M(2)-Te-Ge	102.68(11)	101.96(5)	101.85(6)
Te-Ge-Te	115.53(7) $\times 3$	114.336(29) $\times 3$	114.033(32) $\times 3$
Te-Ge-Te	102.39(10) $\times 3$	104.01(4) $\times 3$	104.40(4) $\times 3$

#### 4.4.2 Low Temperature Neutron Diffraction

CrGeTe<sub>3</sub> undergoes magnetic ordering at 61 K as confirmed by powder neutron diffraction (G4.1, LLB). Below 61 K magnetic scattering is superimposed upon the nuclear Bragg peaks indicating a propagation vector  $\mathbf{k} = [0,0,0]$ . To ensure the onset of magnetic ordering, CrGeTe<sub>3</sub> was studied at 4.2 K on POLARIS. The magnetic structure of CrGeTe<sub>3</sub> has been solved in  $R\bar{3}$  with lattice parameters  $a = 6.8337(1) \text{ \AA}$ ,  $c = 20.4141(8) \text{ \AA}$  at 4.2 K. The moments are consistent with the presence of Cr<sup>3+</sup> and at 4 K are aligned along the c-axis superimposed with the crystallographic unit cell. It was found that cation distribution varied from slab to slab. It has been suggested that these defects may be responsible for the differences in stacking of equivalent slabs that result in the reduction in symmetry from  $R\bar{3}$  to  $P6_3/mmc$ .

Low temperature neutron diffraction data were collected on CrGeTe<sub>3</sub> at ISIS, on POLARIS are shown in Figure 65.

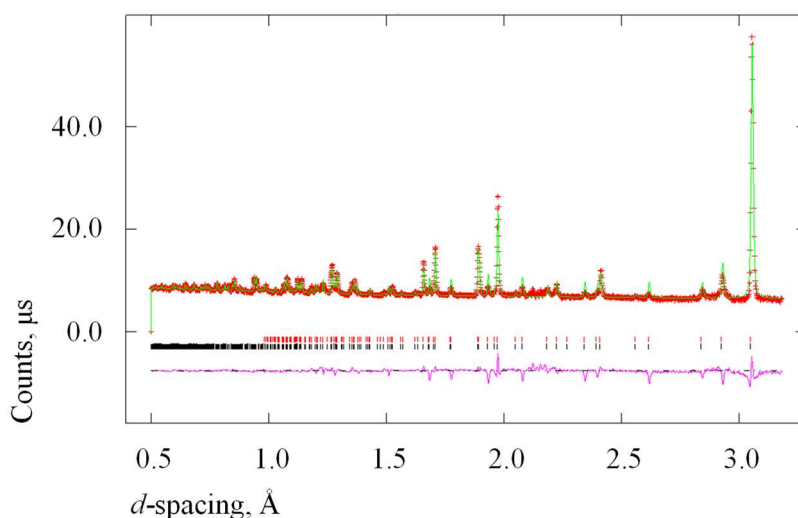


**Figure 65:** Final observed (crosses), calculated (upper full line) and difference (lower full line) neutron diffraction profile for CrGeTe<sub>3</sub> at 4.2 K; backscattering bank  $2\theta = 145^\circ$ . Reflection positions are marked; lower markers refer to crystallographic unit cell, upper markers to the superimposed magnetic unit cell.

**Table 28:** Final refined parameters for CrGeTe<sub>3</sub> in space group  $R\bar{3}$  at 4.2 K.

Source		Neutron
$a / \text{\AA}$		6.8337(1)
$c / \text{\AA}$		20.4141(8)
$V / \text{\AA}^3$		825.609(32)
Cr <sup>a</sup>	<i>site</i>	6( <i>c</i> )
	<i>z</i>	0.3346(4)
	<i>B</i>	4.14
	Moment/ $\mu_B$	2.1(3)
Ge <sup>a</sup>	<i>site</i>	6( <i>c</i> )
	<i>z</i>	0.0587(1)
	<i>B</i>	1.30
Te	<i>site</i>	18( <i>f</i> )
	<i>x</i>	0.6669(5)
	<i>y</i>	-0.0284(3)
	<i>z</i>	0.2490(1)
	<i>B</i>	0.79
R <sub>wp</sub> / % Backscattering bank: 2 $\theta$ = 145°		1.92
$\chi^2$		13.42

---

<sup>a</sup> 6(*c*) site is a special position at  $0\ 0\ z$



#### 4.4.3 High Temperature X-ray Diffraction

X-ray diffraction experiments (Section 2.2.1) were carried out at elevated temperatures for the series  $\text{Cr}_{1-x}\text{In}_x\text{GeTe}_3$ . Diffraction patterns were collected in  $20^\circ$  steps from  $30^\circ\text{C}$  to  $150^\circ\text{C}$  and in  $50^\circ$  increments between  $150^\circ\text{C}$  and  $700^\circ\text{C}$ . These experiments were carried out in order to investigate the changes in crystallinity and cationic ordering across the series with the aim of improving the synthesis procedure. As shown in Figure 66 and Figure 67 the experiments did not yield a particular temperature whereby the materials became more crystalline, indeed they decomposed into GeTe and  $\text{CrO}_3$ ; the indium containing samples also had  $\text{In}_2\text{Te}_3$  and  $\text{In}_2\text{O}_3$  in the final decomposed product. If the experimental set up could provide an air tight environment, this type of investigation could be used to provide a detailed reaction mechanism in order to optimise the synthesis of this type of materials.

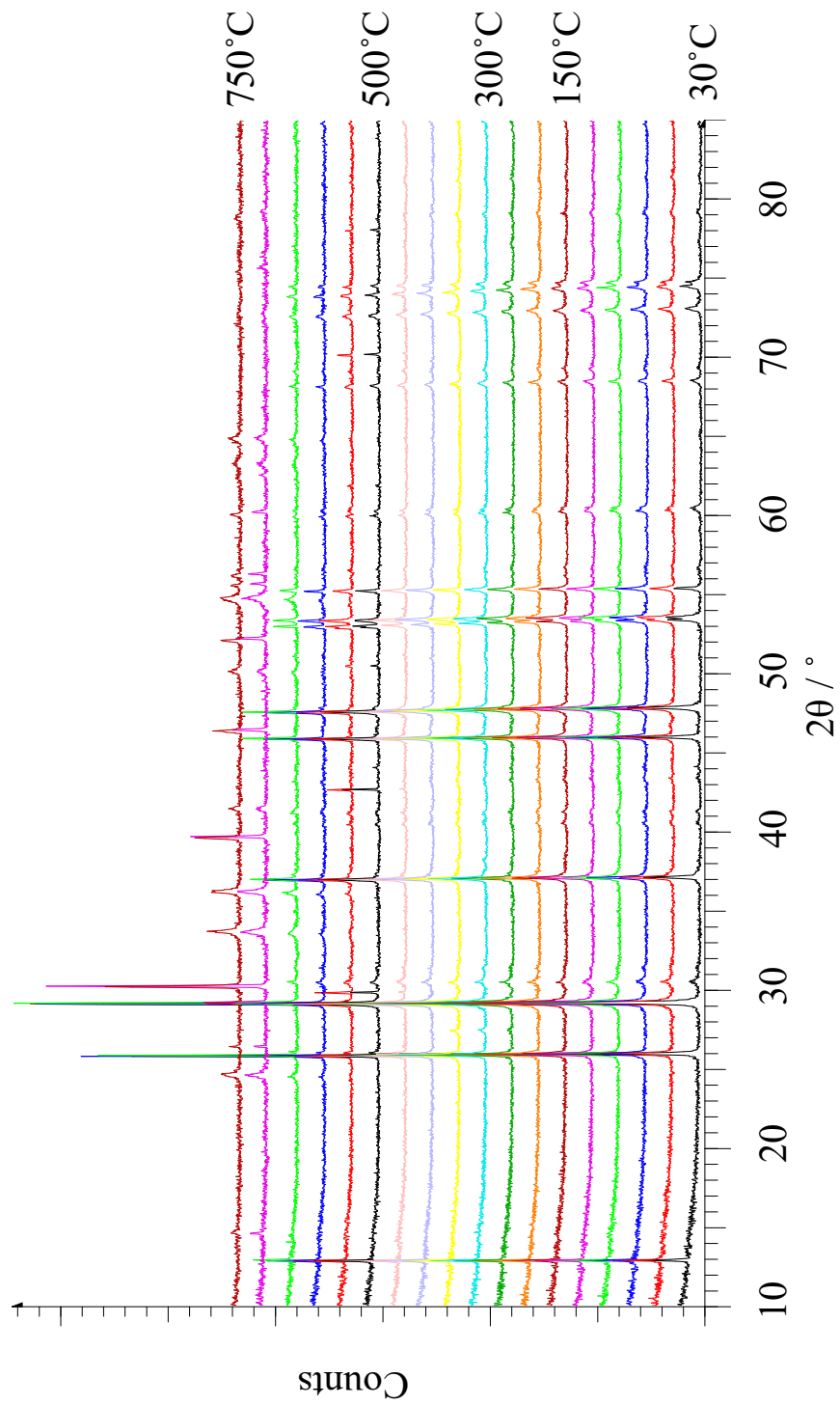


**Figure 66:** High temperature X-ray diffraction data for CrGeTe<sub>3</sub>.

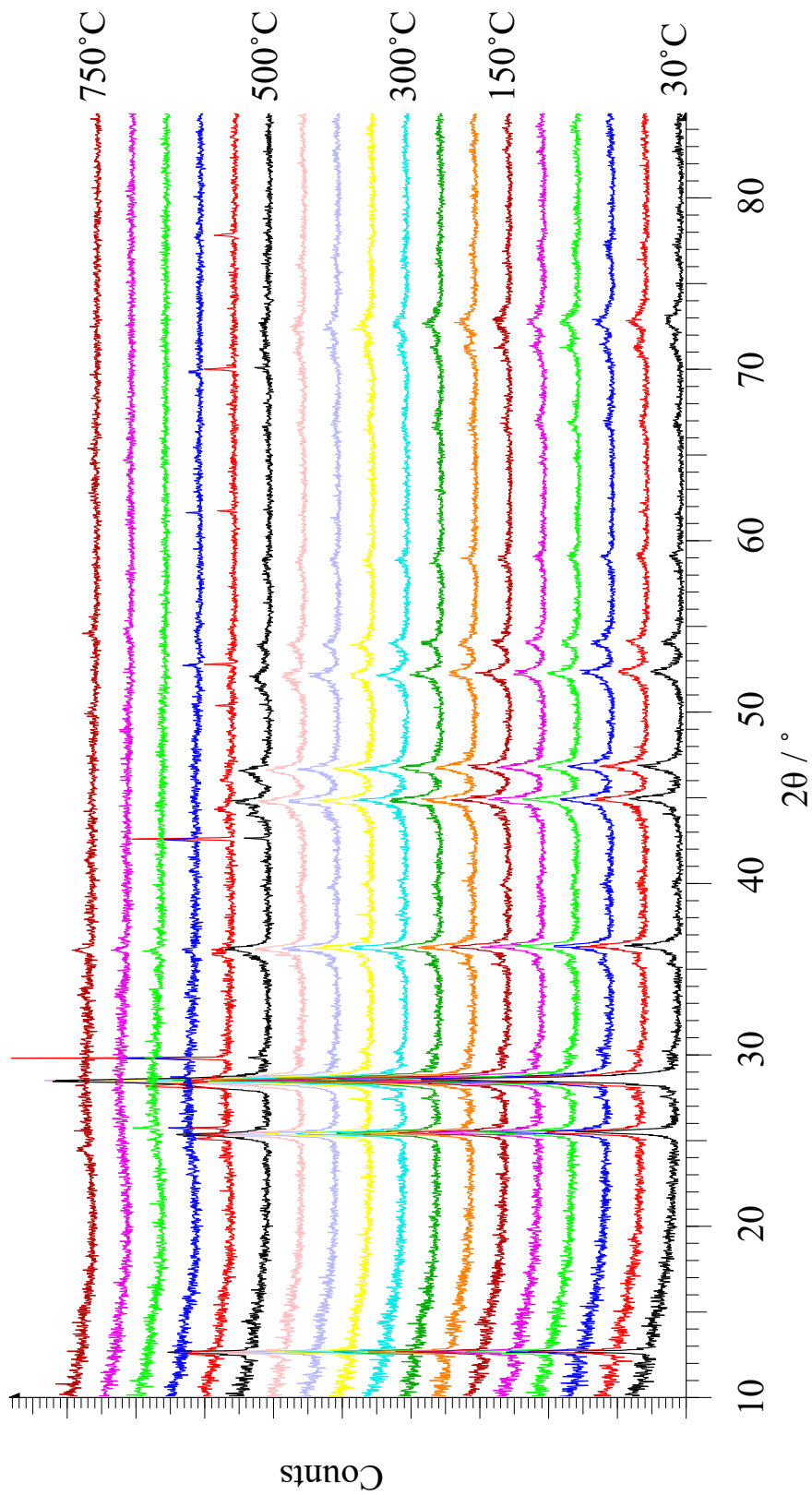


Figure 67: High temperature X-ray diffraction data for  $\text{Cr}_{0.5}\text{In}_{0.5}\text{GeTe}_3$ .

#### 4.4.4 Resistivity Measurements

Electrical resistivity measurements for all samples were conducted as outlined in Section 2.3.1 Electron Transport Measurements. Samples throughout the series exhibited semiconducting behaviour (Figure 68, Figure 69), however,  $x = 0.4$  (Figure 71) showed markedly lower resistivity than other members of the series. Analysis of these semiconducting data showed samples did not exhibit thermally activated conduction in that a plot of  $\ln(\rho)$  against  $1/T$  did not result in a linear trend line. Data were, however, found to fit a variable-range-hopping model that represents electrical conductivity in three-dimensions by the following equation [8], where  $\nu = 1/4$ .

$$\rho = \rho_0 \left(\frac{T}{T_0}\right)^{1/2} e \left[ \left(\frac{T_0}{T}\right)^\nu \right]$$

**Equation (41)**

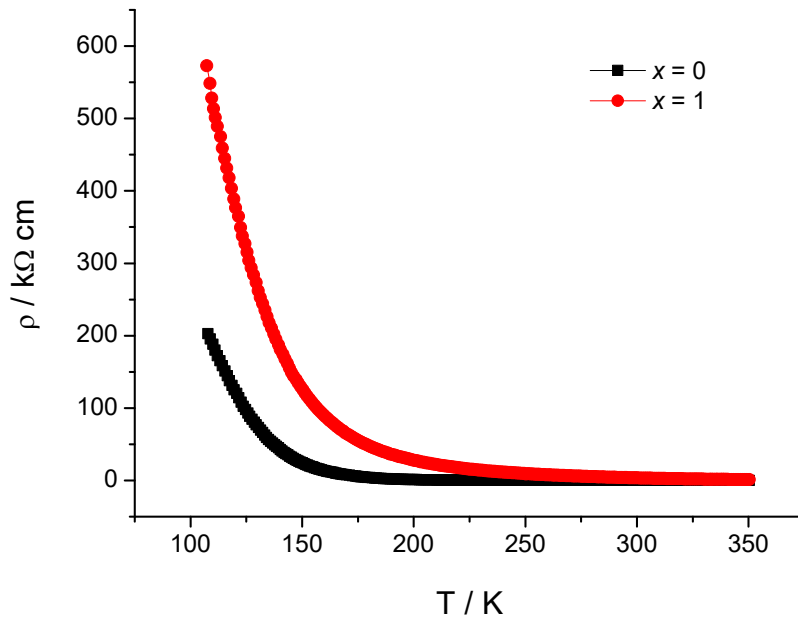


**Figure 68:** Electrical resistivity data for end-members of the  $\text{Cr}_{1-x}\text{In}_x\text{GeTe}_3$  series.

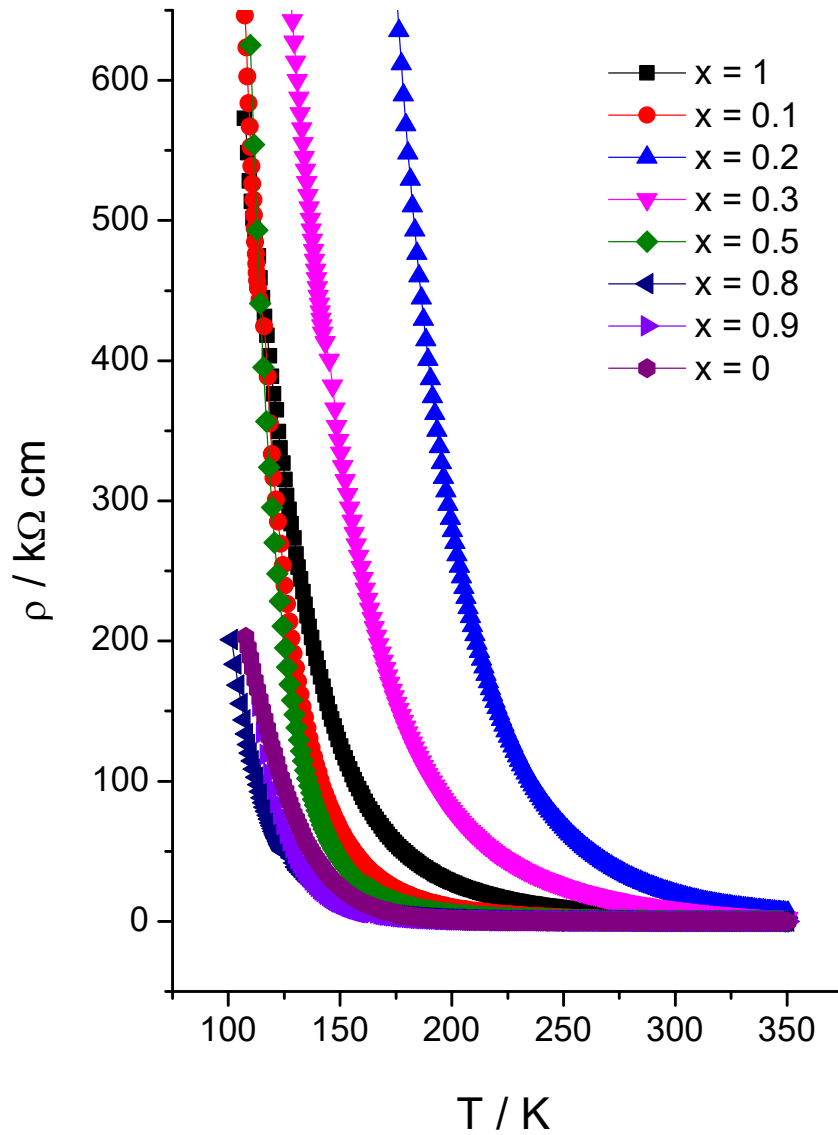


**Figure 69:** Electrical resistivity data for the series  $\text{Cr}_{1-x}\text{In}_x\text{GeTe}_3$ .

Carteaux *et al.* determined the thermal evolution of the resistivity can be fitted using  $\rho = e^{-A/kT}$  where  $A = 0.2$  eV. The band structure and crystal orbitals of  $\text{CrGeTe}_3$  were also calculated using the extended Huckel method and indicated no gap but highly localized Cr 3d states, giving evidence of a hopping mechanism for  $\text{CrGeTe}_3$  electrical conductivity. [9]

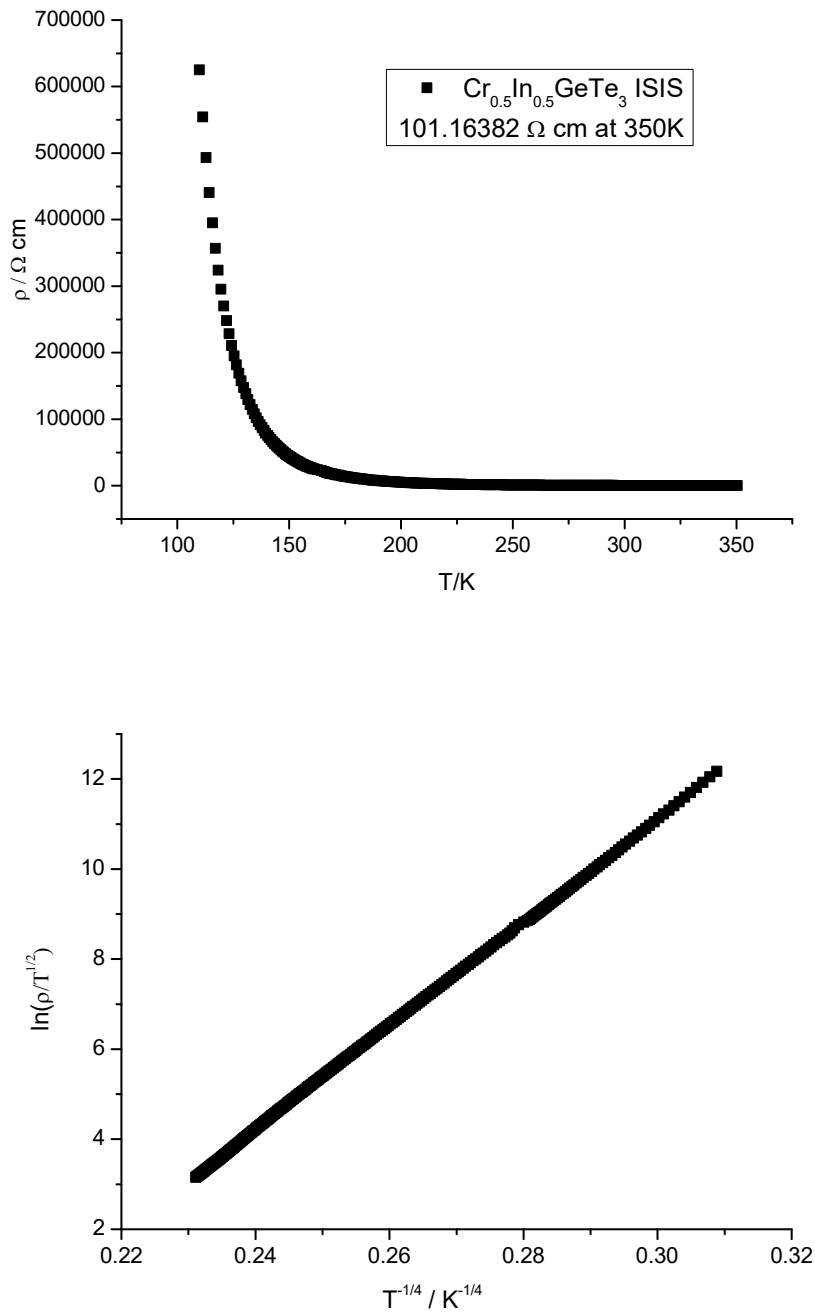


**Figure 70:** Temperature dependence of  $\text{Cr}_{0.5}\text{In}_{0.5}\text{GeTe}_3$  using a variable-range-hopping relation;  $\ln(\rho/T^{1/2})$  versus  $T^{-\nu}$  where  $\nu = 1/4$ .

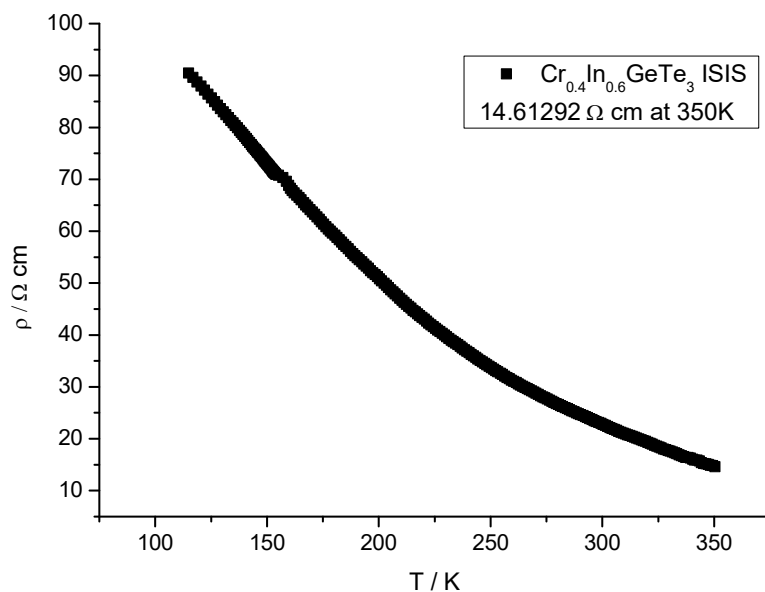


**Figure 71:** Electrical resistivity of  $\text{Cr}_{0.4}\text{In}_{0.6}\text{GeTe}_3$  over the range  $115 \leq T / \text{K} \leq 350$ .

#### 4.4.5 Seebeck Coefficient

Seebeck coefficient measurements were performed as outlined in Section 2.3.2 Seebeck Measurements. Data were collected between 100 K and room temperature. For  $x = 0$  and  $x = 0.1$  in  $\text{Cr}_x\text{In}_{1-x}\text{GeTe}_3$ , the Seebeck coefficient is large and positive, Figure 72, indicating that the dominant charge carriers are holes. Through progressive substitution of chromium for indium this remains the case. However at  $x = 0$ ,  $\text{InGeTe}_3$  shows markedly different behaviour. It undergoes a change in the dominant charge carriers from electrons to holes at 245 K. The dramatic change in Seebeck coefficient at 245 K could be structural in origin.

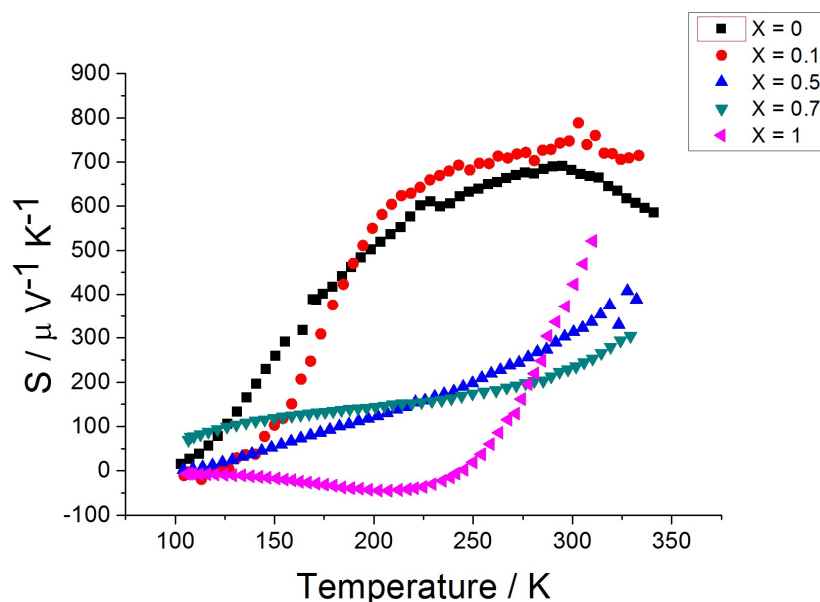


**Figure 72:** Selected Seebeck coefficient data for the series  $\text{Cr}_{1-x}\text{In}_x\text{GeTe}_3$  collected between  $100 \leq T/\text{K} \leq \text{RT}$ .

#### 4.4.6 Thermal Conductivity

Thermal conductivity measurements were made across the series over the temperature range  $100 \leq T/\text{K} \leq 400$ . As the amount of indium substitution is increased, the thermal conductivity decreases, Figure 73. The phonon contribution to the thermal conductivity is reduced with the increase in atomic mass from chromium to indium.

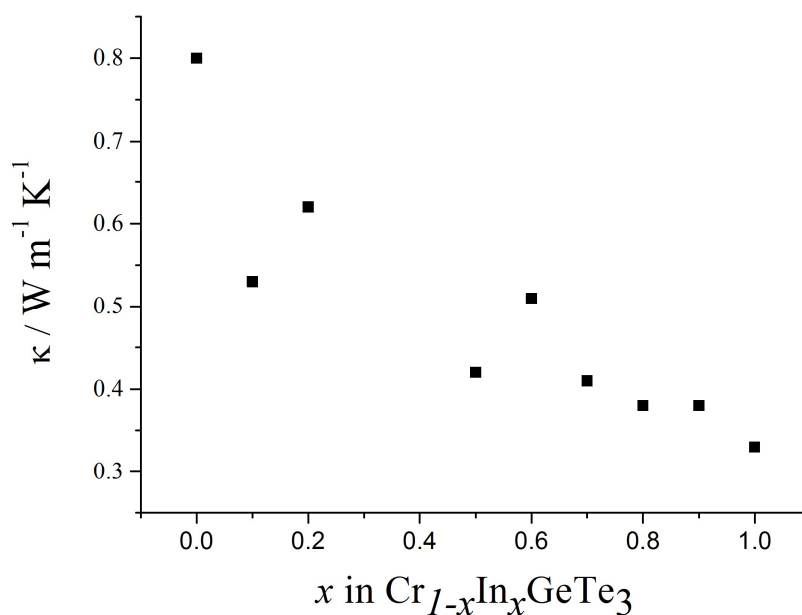


**Figure 73:** Thermal conductivity data for  $\text{Cr}_{1-x}\text{In}_x\text{GeTe}_3$  at 300 K.



#### 4.4.7 Thermoelectric Figure of Merit

These materials do not have a thermoelectric figure a merit,  $ZT$ , value that would justify further research in order to make them commercially viable and available, Table 29.

**Table 29:**  $ZT$  values for  $\text{Cr}_{1-x}\text{In}_x\text{GeTe}_3$  ( $0 \leq x \leq 1$ ).

$x$ in $\text{Cr}_{1-x}\text{In}_x\text{GeTe}_3$	$ZT$
0	0.00277
0.1	0.0110
0.5	0.000226
0.7	$3.45 \times 10^{-6}$
1	$6.25 \times 10^{-5}$

#### 4.4.8 Magnetic Studies

The magnetic properties for  $\text{Cr}_{1-x}\text{In}_x\text{GeTe}_3$  have been measured as a function of chromium content and the data processed according to Section 2.3.4. For the end-member,  $x = 0$ , the susceptibilities were measured under a field of 1000 G with an increment of  $5^\circ$  in the temperature range  $5 \leq T / \text{K} \leq 150$ . Ferromagnetism is characterised by a large susceptibility at low temperatures that decreases, increasingly rapidly with rising temperature. [10]  $\text{Cr}_{1-x}\text{In}_x\text{GeTe}_3$  samples therefore show ferromagnetic ordering below the Curie temperature,  $T_C$ . The field cooled and zero-field cooled data points overlap each other above  $T_C$ , where materials revert back to paramagnetic. The ferromagnetic transition temperatures are estimated in Table 29 and appear to decrease as the chromium ions are diluted by indium. In  $\text{Cr}_{1-x}\text{In}_x\text{GeTe}_3$ ,  $x = 0, 0.1, 0.2, 0.5, 0.6, 0.8$  materials, a Curie-Weiss law can be applied; data are shown through Figure 74 - Figure 82.

Spin glass behaviour is the occurrence of a transition in which spin orientations freeze without establishing long-range order.[11] For the spin orientations to freeze without establishing any long-order, they must be subject to severe

competing interactions, typically found with a combination magnetic site disorder and frustration favouring geometries.  $\text{Cr}_{1-x}\text{In}_x\text{GeTe}_3$ ,  $x = 0.1, 0.2, 0.5, 0.6$  samples have a range of ferromagnetism that can be described using Curie-Weiss law, but they also have regions of spin glass dominated behaviour below the ‘freeze’ temperature,  $T_f$ . A characteristic of this behaviour is clearly distinguished ZFC and FC susceptibility against temperature dependences. The peak in the ZFC curve indicates  $T_f$ . For samples  $x \geq 0.7$ , ferromagnetism is still evident in the susceptibility against temperature data, though Curie-Weiss law is no longer appropriate, Figure 82, at any temperature. Here, materials show dominant spin-glass behaviour.

Table 30 presents a summary of the magnetic parameters of the six samples that were characterised; the end-member,  $\text{InGeTe}_3$ , was not studied due to limited experimental time. Figure 75, Figure 78 and Figure 80 show the temperature dependence of the effective magnetic moment per ion in  $\text{Cr}_{1-x}\text{In}_x\text{GeTe}_3$ .

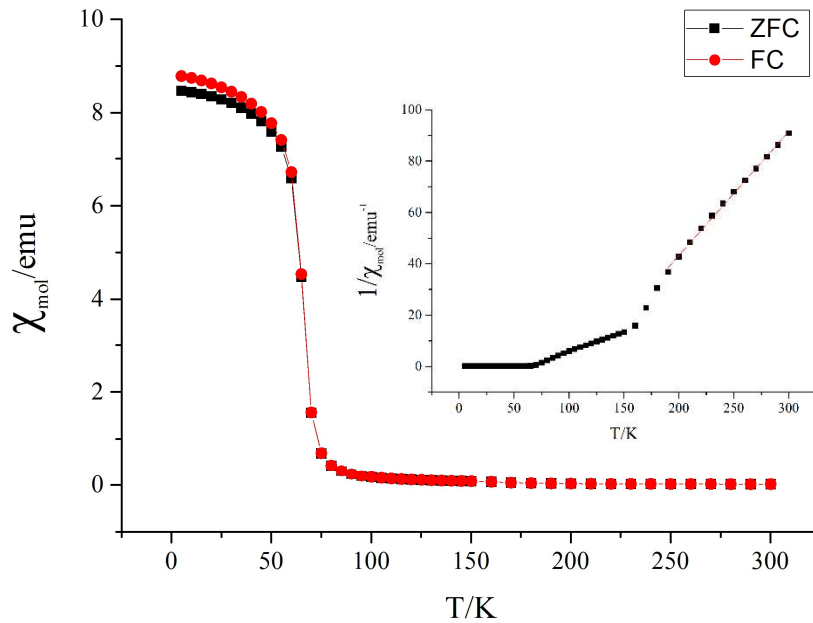


**Figure 74:** Magnetic susceptibility data for  $\text{CrGeTe}_3$  measured in a field of 100 G. Red circles represent field cooled and black squares show zero-field cooled data. The inset shows the fit of a Curie-Weiss expression to the reciprocal susceptibility.

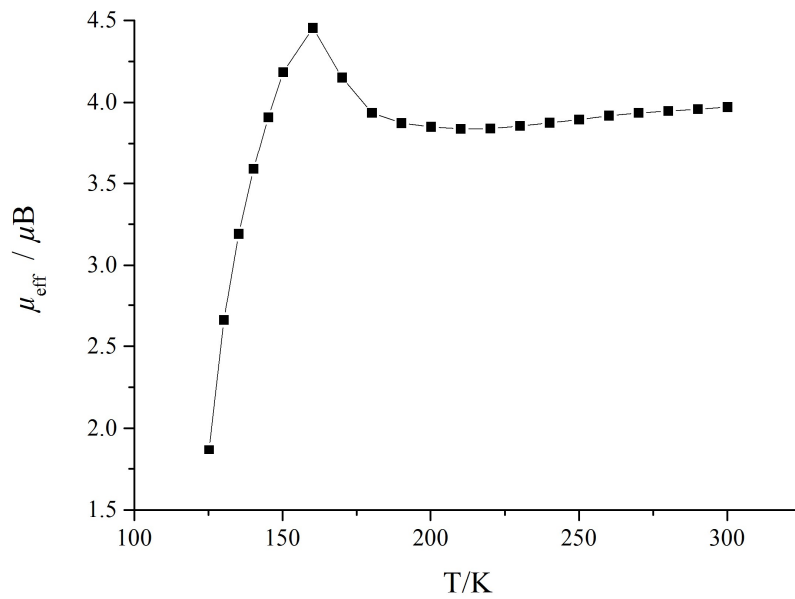


**Figure 75:** Plot showing the temperature dependence of the effective magnetic moment per ion in CrGeTe<sub>3</sub>.

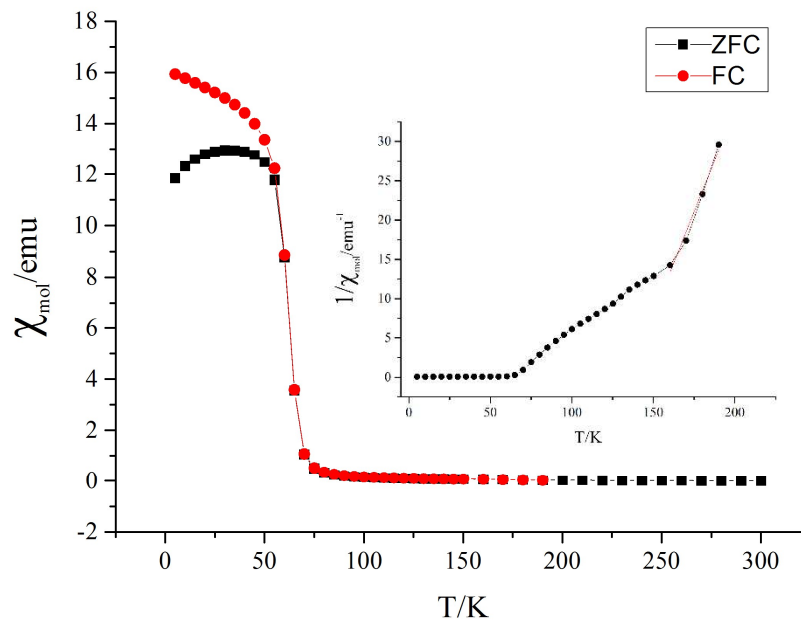


**Figure 76:** Magnetic susceptibility data for Cr<sub>0.9</sub>In<sub>0.1</sub>GeTe<sub>3</sub> measured in a field of 100 G. Red circles represent field cooled and black squares show zero-field cooled data. The inset shows the fit of a Curie-Weiss expression to the reciprocal susceptibility.

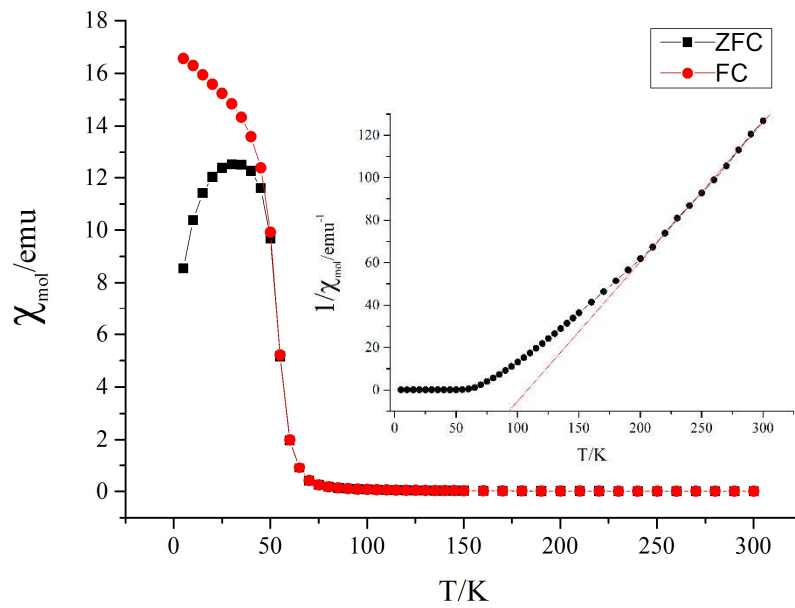


**Figure 77:** Magnetic susceptibility data for  $\text{Cr}_{0.8}\text{In}_{0.2}\text{GeTe}_3$  measured in a field of 100 G. Red circles represent field cooled and black squares show zero-field cooled data. The inset shows the fit of a Curie-Weiss expression to the reciprocal susceptibility.

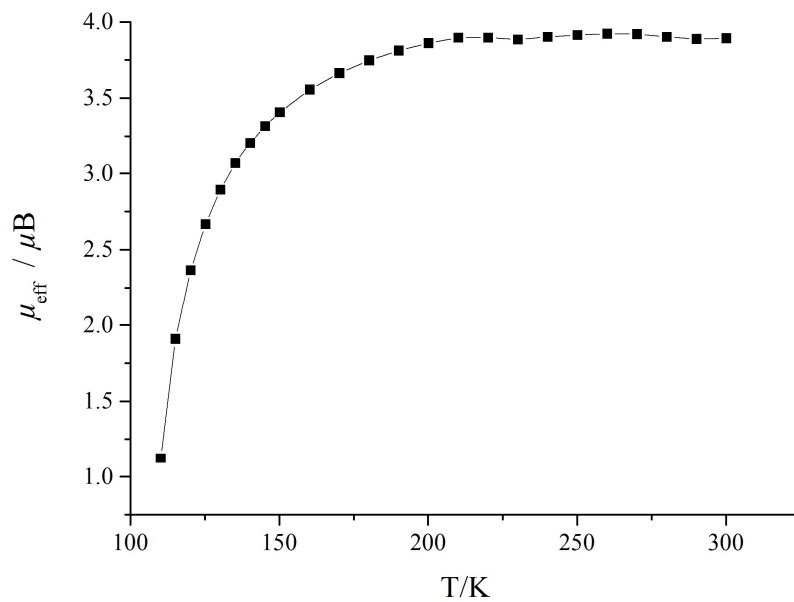


**Figure 78:** Plot showing the temperature dependence of the effective magnetic moment per ion in  $\text{Cr}_{0.8}\text{In}_{0.2}\text{GeTe}_3$ .

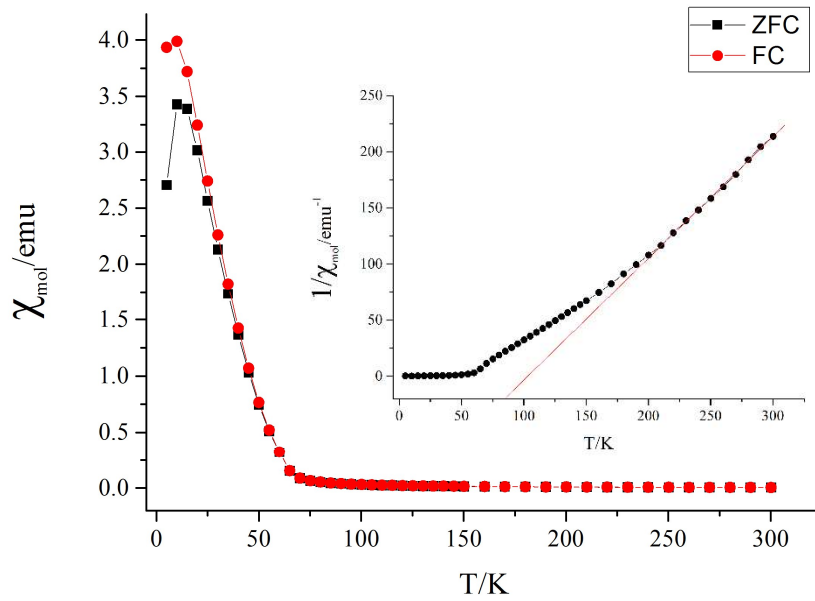


**Figure 79:** Magnetic susceptibility data for  $\text{Cr}_{0.5}\text{In}_{0.5}\text{GeTe}_3$  measured in a field of 100 G. Red circles represent field cooled and black squares show zero-field cooled data. The inset shows the fit of a Curie-Weiss expression to the reciprocal susceptibility.

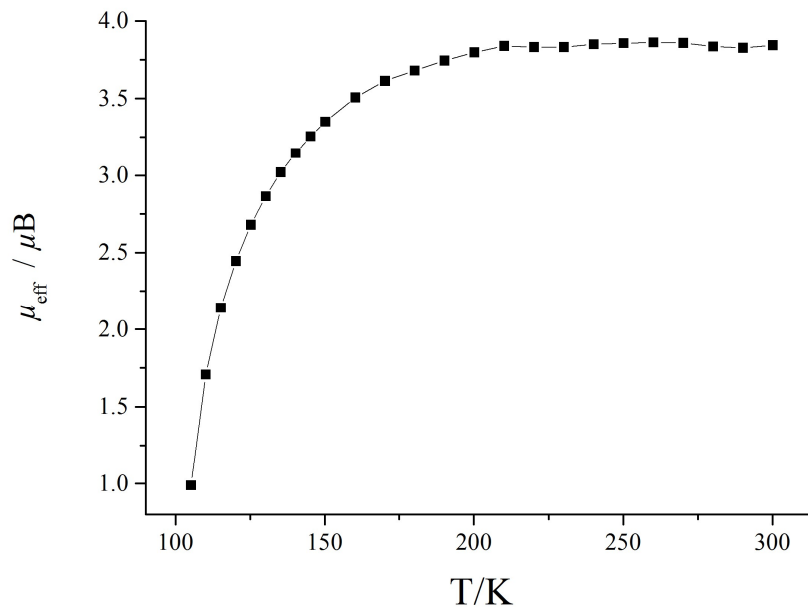


**Figure 80:** Plot showing the temperature dependence of the effective magnetic moment per ion in  $\text{Cr}_{0.5}\text{In}_{0.5}\text{GeTe}_3$ .

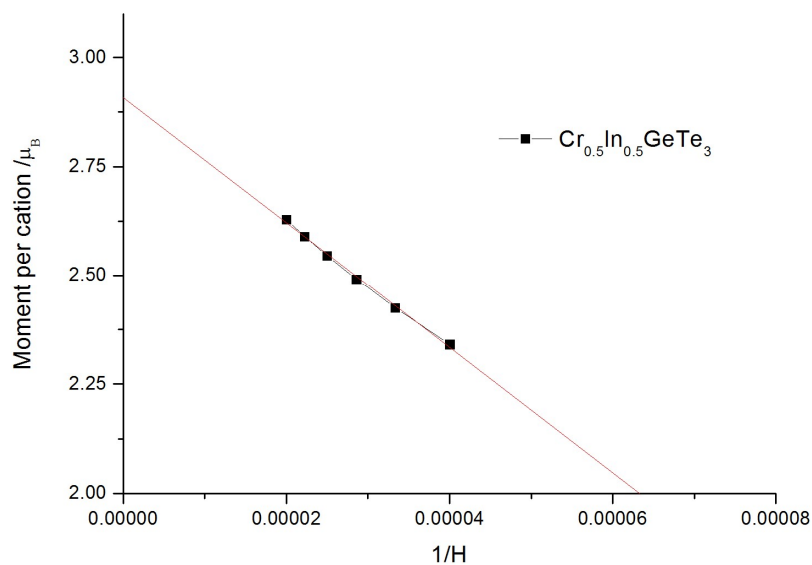


**Figure 81:** Plot showing the saturation magnetisation of  $2.91(1) \mu_B$  for  $\text{Cr}_{0.5}\text{In}_{0.5}\text{GeTe}_3$ .

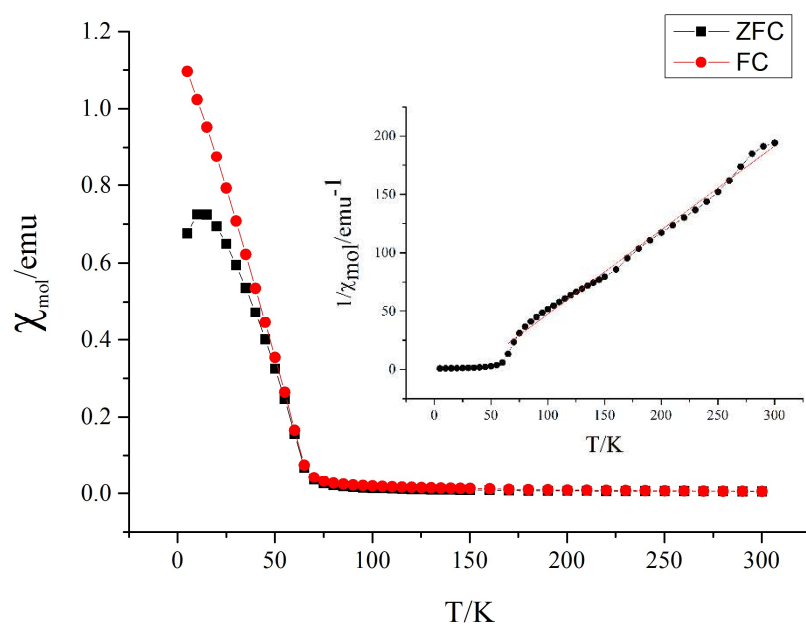


**Figure 82:** Magnetic susceptibility data for  $\text{Cr}_{0.2}\text{In}_{0.8}\text{GeTe}_3$  measured in a field of 100 G. Red circles represent field cooled and black squares show zero-field cooled data. The inset demonstrates the poor fit of a Curie-Weiss expression to the reciprocal susceptibility.

**Table 30:** Summary of parameters derived from magnetic susceptibility data using Curie-Weiss law.

$x$ in $\text{Cr}_{1-x}\text{In}_x\text{GeTe}_3$	0	0.1	0.2	0.5	0.6	0.8
$C$	1.92	1.65	1.52	0.926	1.39	1.39
$\theta / \text{K}$	+ 121	+ 141	+ 108	+ 103	+ 81	+ 34
$T_C / \text{K}$	75	70	65	65	65	65
$T_f / \text{K}$	-	30	30	10	10	10
$\mu_{\text{eff}} / \mu_B$	3.91	3.82	3.90	3.85	5.27	7.46

## 4.5 Discussion

As substitution of chromium with indium in the series  $\text{Cr}_{1-x}\text{In}_x\text{GeTe}_3$  ( $0 \leq x \leq 1$ ) progresses there is an increase in crystal symmetry and size of the unit cell, Figure 55. The Ge-Ge dumbbell is maintained throughout the solved structures with a gradual decrease in the bond length from 2.402(4) Å to 2.3585(3) Å, resulting from an increase in the Te-M bond length as the smaller atom is substituted for the larger indium.

At  $x \geq 0.2$ , the model used to describe  $\text{CrGeTe}_3$  is no longer representative. For values of  $x$ ,  $0.2 \leq x \leq 0.8$ , materials adopt a two layer repeating unit in space group  $P\bar{3}1c$ , similar to  $\text{Mn}_3\text{Si}_2\text{Te}_6$ . The chromium indium germanium tellurides consist of a layer of tellurium octahedra with fully occupied central cationic sites followed by an unoccupied layer, a van de Waals' gap that repeats along the  $c$ -axis with a van de Waals' gap. There are two fully occupied layers in the unit cell, resulting from the ordering of the central octahedral cation.  $\text{Mn}_3\text{Si}_2\text{Te}_6$  possesses a similar size unit cell,  $a = 7.029(2)$ ,  $c = 14.255(3)$  Å, but an excess of manganese is inserted into what would be an unoccupied slab, to become partially filled. The surroundings of Si and Ge atoms are similar to the ones found in  $\text{Si}_2\text{Te}_3$  and  $\text{K}_6\text{Ge}_2\text{Te}_6$  and the fully occupied layer of octahedra may be compared to  $\text{Fe}_2\text{P}_2\text{Se}_6$ . [3]

As chromium is replaced with indium, the electrical resistivity increases, Figure 69.  $\text{Cr}^{3+} [\text{Ar}] 3d^3$  has three unpaired electrons, compared with  $\text{In}^+ [\text{Kr}] 4d^{10}5s^2$ . As the concentration of charge carriers decreases, so will the electrical conductivity. The same principal of diluting the charge carrier

applies to the Seebeck coefficient also; as the chromium concentration is decreased the magnitude of the Seebeck coefficient is reduced.

The parent compound CrGeTe<sub>3</sub> exhibits ferromagnetic ordering below 70 K, however there are different dominant spin behaviours as chromium is substituted. As the concentration of chromium is decreased, there is a reduction in long range order. Rietveld refinements of diffraction data showed no improvement when the structural models ordered the chromium and indium cations. This cationic disorder throughout the series could result in the spin glass behaviour that is observed beyond CrGeTe<sub>3</sub>.

## 4.6 References

- [1] V. Carreaux, D. Brunet, G. Ouvrard, G. Andre, *Journal of Physics-Condensed Matter* 7 (1995) 69-87.
- [2] G. Ouvrard, E. Sandre, R. Brec, *Journal of Solid State Chemistry* 73 (1988) 27-32.
- [3] H. Vincent, D. Leroux, D. Bijaoui, R. Rimet, C. Schlenker, *Journal of Solid State Chemistry* 63 (1986) 349-352.
- [4] A. Assoud, N. Soheilnia, H. Kleinke, *Journal of Solid State Chemistry* 179 (2006) 2707-2713.
- [5] X. Chen, J. Qi, D. Shi, *Physics Letters A* 379 (2015) 60-63.
- [6] A.C. Larson, R.B. Dreele, Los Alamos National Laboratory Report.
- [7] B.A. Bruker AXS: TOPAS V3: General profile and structural analysis software for powder diffraction data. – User’s Manual, Karlsruhe, Germany, 2005.
- [8] B.I. Shklovskii, A.L. Efros, 1984.
- [9] B. Siberchicot, S. Jobic, V. Carreaux, P. Gressier, *Journal of Physical Chemistry* 100 (1996) 5863-5867.
- [10] A.R. West, *Solid State Chemistry and its Applications*. John Wiley & Sons, LTD, 1984.
- [11] F. Bodénan, V.B. Cajipe, M. Danot, G. Ouvrard, *Journal of Solid State Chemistry* 137 (1998) 249-254.



## Chapter 5: Conclusions and Suggestions for Further Work

Materials covered in this study have shown a range of unusual behaviours.  $\text{GeV}_4\text{S}_8$  has been successfully synthesized in order to investigate the structural properties as a function of temperature. Structural refinements of these data reveal that there are three distinct polymorphs over the temperature range  $7 \leq T / \text{K} \leq 32$ , of which one had not been previously determined.  $\text{GeV}_4\text{S}_8$  adopts a defect spinel structure, space group  $F\bar{4}3m$  at room temperature. Neutron diffraction experiments reveal a series of peak splittings and broadenings upon cooling to indicate a deviation from the face-centred cubic structure. The fine structure is qualitatively different at 25 K compared with 10 K. Johrendt *et al.*[1], have reported a phase transition directly from the cubic to the orthorhombic structure but this would be characterised by only a decrease in the central peak intensity with the simultaneous, gradual, appearance of the satellite peaks. However, what is observed is different. After the appearance of the satellite peaks at 30 K, the intensities remain level before the central peak increases again at 17 K. An orthorhombic phase cannot fit a reduced size central peak in this plateau region whilst still maintaining intensity in the satellites. This is because the allowed profile for the three orthorhombic reflections, originating from the cubic [440], is a 1:4:1 ratio. A reduction in symmetry to  $R3m$ , at  $T_S = 32$  K is observed. Antiferromagnetic ordering is then associated with a second successive phase transition at  $T_N = 17.8$  K. At  $T_N$  it is the pronounced lengthening in the  $a$  lattice parameter and an increase in  $\beta$  of  $M\text{-GeV}_4\text{S}_8$  that coincides with the antiferromagnetic ordering of  $\text{GeV}_4\text{S}_8$ . This monoclinic phase has previously not been reported.

The new series of mixed-metal tellurides has been prepared through substitution of chromium with indium in the series  $\text{Cr}_{1-x}\text{In}_x\text{GeTe}_3$  ( $0 \leq x \leq 1$ ) to investigate the effects of diluting the magnetic cation on the structural, physical and magnetic properties. The end-member phase,  $\text{CrGeTe}_3$ , crystallises in space group  $R\bar{3}$  with a three-layer repeating unit. It consists of hexagonally close packed layers of  $\text{Te}^{2-}$  ions, with  $\text{Cr}^{3+}$  ions and  $(\text{Ge}_2)^{6+}$

dumbbell pairs occupying octahedral holes in every other layer and providing a van der Waals' gap. These unoccupied layers persist throughout the series; however cationic ordering within the layers of  $\text{Te}^{2-}$  ions results in different stacking sequences. For  $x = 0.1$ , the incorporation of indium does result in a two phase mixture of the substituted phases. Within the range  $0.2 \leq x \leq 0.6$ , the reflection centred at  $\sim 7 \text{ \AA}$ , becomes the [002]. This structure is currently best described in space group  $P\bar{3}1c$  with the same two-dimensional ordering of  $\text{Cr}^{3+} / \text{In}^{3+}$  ions and  $(\text{Ge}_2)^{6+}$  pairs as in  $R\bar{3}$  but with a two-layer repeat along the [00 $\bar{1}$ ] plane. From the Rietveld refinements there are some discrepancies with inadequately modelled peak shape; these were originally attributed to preferred orientation however further investigation is required in order to fully elucidate the structure. Samples throughout the series exhibited semiconducting behaviour, however, there is an anomaly in  $x = 0.4$  as it showed a much lower resistivity. Analysis of these semiconducting data showed samples did not exhibit thermally activated conduction but were found to fit a variable-range-hopping model that represents electrical conductivity in three-dimensions. For  $x = 0$  and  $x = 0.1$  in  $\text{Cr}_{1-x}\text{In}_x\text{GeTe}_3$ , the Seebeck coefficient is large and positive indicating that the dominant charge carriers are holes; through progressive substitution of chromium for indium this remains the case. However at  $x = 0$ ,  $\text{InGeTe}_3$  shows markedly different behaviour, it undergoes a change in the dominant charge carriers from electrons to holes at 245 K.  $\text{Cr}_{1-x}\text{In}_x\text{GeTe}_3$ ,  $x = 0, 0.1, 0.2, 0.5, 0.6$  samples have a range of ferromagnetism that can be described using Curie-Weiss law, but they also have regions of spin glass dominated behaviour below the 'freeze' temperature,  $T_f$ .

Further work could be carried out in the following areas:

- In order to determine the origin of the poorly crystalline samples in  $\text{Cr}_{1-x}\text{In}_x\text{GeTe}_3$  high temperature neutron experiments could be conducted.
- Data sets from electronic property measurements should be further discussed for  $\text{Cr}_{1-x}\text{In}_x\text{GeTe}_3$   $0 \leq x \leq 1$  and reported appropriately.
- For  $\text{InGeTe}_3$  the structural origin of the dramatic change in Seebeck coefficient at 245 K could be carried out. It has been reported by A.

Abba-Touré *et al.*, that the compound TlGeTe<sub>3</sub>, has been synthesised, this could provide further insight into InGeTe<sub>3</sub>. [2]

## 5.1 References

- [1] D. Johrendt, *Zeitschrift Fur Anorganische Und Allgemeine Chemie* 624 (1998) 952-958.
- [2] A. Abba-Touré, G. Kra, R. Eholié, *Journal of the Less Common Metals* 170 (1991) 199-222.